# Mathematical Modeling and Dimension Reduction in Dynamical Systems

**Elmegård, Michael; Starke, Jens; Evgrafov, Anton ; Thomsen, Jon Juel**

*Publication date:*
2014

*Document Version*
Publisher's PDF, also known as Version of record

# Mathematical Modeling and Dimension Reduction in Dynamical Systems

Michael Elmegård

Kongens Lyngby 2014
PHD-2014-321

Technical University of Denmark
Informatics and Mathematical Modelling
Building 321, DK-2800 Kongens Lyngby, Denmark
Phone +45 45253351, Fax +45 45882673
reception@imm.dtu.dk
www.imm.dtu.dk

PHD: ISSN 0909-3192

# Summary

Processes that change in time are in mathematics typically described by differential equations. These may be applied to model everything from weather forecasting, brain patterns, reaction kinetics, water waves, finance, social dynamics, structural dynamics and electrodynamics to name only a few. These systems are generically nonlinear and the studies of them often become enormously complex. The framework in which such systems are best understood is via the theory of dynamical systems, where the critical behavior is systematically analyzed by performing bifurcation theory. In that context the current thesis is attacking two problems.

The first is concerned with the mathematical modelling and analysis of an experiment of a vibro-impacting beam. This type of dynamical system has received much attention in the recent years and they occur frequently in mechanical applications, where they induce noise and wear which decrease the life time of machines. From the modelling point of view these systems are often particularly rich in nonlinear dynamics. In the present study a mathematical model is derived. Amongst other outcomes the model was successfully applied to predict a nonlinear phenomenon, namely the existence of isolas of subharmonic orbits. These were then verified in the practical experiment in the lab.

The second problem that is addressed in the current thesis is a problem that has developed as a consequence of the increasing power of computers which has created the demand for analysis of ever more advanced and complex systems. These complex systems are computationally very demanding and proper analysis of the qualitative behavior of the systems becomes difficult. In general it is not possible to construct bifurcation diagrams for these so-called high-dimensional

models efficiently. In order to overcome this obstacle much research is going into the direction of development of robust methods to perform dimension and model reduction such as to pave the way for a qualitative analysis of the high-dimensional problems by analyzing the low-dimensional models.

In this thesis we demonstrate how to reduce the dimension of a certain class of dynamical systems by construction of $k$-dimensional submanifolds using the so-called graph transform. The method is suitable for a specific class of problems with spectral gaps, these are often observed. In particular the method is applied to a mechanical system. Furthermore the method has some unique and promising properties compared to other methods.

# Resumé

Processer som ændrer sig i tiden er i matematik typisk beskrevet af differentialligninger. Disse kan anvendes til at modellere vejrprognoser, hjernemønstre, reaktions-kinetik, bølger i vand, finansprognoser, social dynamik, strukturel dynamik, elektrodynamik og meget andet. Disse systemer er generisk ikke-lineære, og studiet af dem er ofte enormt komplekst. Den bedste fremgangsmåde i analysen af disse systemer er via dynamisk systemer, i hvilke man systematisk kan analysere den kritiske opførsel ved at anvende bifurkationsteori. I den sammenhæng angriber denne afhandling to problemer.

Det første omhandler den matematiske modellering og analyse af en bjælke som bliver udsat for påtrykte svingninger og kolliderer med mekaniske stop. Denne type af dynamisk system har været genstand for megen interesse i den seneste årrække, og de optræder ofte i mekaniske applikationer, hvor de inducerer støj og slitage der nedsætter maskiners levetid. Fra et matematisk modelleringssynspunkt er disse systemer i særdeleshed rige på ikke-lineær dynamik. I denne afhandling bliver en matematisk model for dette system udledt. Modellen blev blandt andet anvendt til at forudsige speciel ikke-lineær opførsel, nemlig nogle isolerede løsninger, og disse blev efterfølgende eftervist i det praktiske eksperiment i værkstedet.

Det andet problem, som er adresseret i denne afhandling, er et problem, der er opstået som en konsekvens af den forøgede beregningskraft fra computere, der har skabt et behov for analyse af mere og mere avancerede og komplekse systemer. Disse komplekse systemer er meget beregningstunge og grundig analyse af systemernes kvalitative opførsel bliver meget vanskelig, i en sådan grad at bifurkationsdiagrammer for de såkaldt højt-dimensionale modeller ikke er muligt at udføre effektivt. For at komme udenom denne forhindring går megen forskn-

ing i retning af at udvikle robuste metoder til at udføre dimensionsreduktion og modelreduktion for at muliggøre den kvalitative analyse af de højt-dimensionale problemer ved at analysere de lavt-dimensionale modeller.

I denne afhandling viser vi hvorledes man kan reducere dimensionen af en specifik klasse af dynamiske systemer ved at konstruere $k$-dimensionale delmangfoldigheder ved anvendelse af den såkaldte graf-transform. Metoden er egnet til en klasse af problemer som har en bestemt separation i sit spektrum, og disse er ofte forekommende. Vi anvender endvidere metoden på et mekanisk system. Metoden har, til sammenligning med andre lignende metoder, nogle unikke og lovende egenskaber.

# Preface

This thesis was prepared at The Technical University of Denmark (DTU) at the Department of Applied Mathematics and Computer Science (formerly the Department of Mathematics), in partial fulfilment of the requirements for acquiring the Ph.D. degree in Mathematics. The scholarship was granted by the former Department of Mathematics. The main supervisor was Associate Professor Jens Starke from the Department of Applied Mathematics and Computer Science (DTU), and the two co-supervisors were Associate Professor Anton Evgrafov from the Department of Applied Mathematics and Computer Science (DTU) and Associate Professor Jon J. Thomsen from the Department of Mechanical Engineering (DTU).

The thesis deals with modelling and dimension reduction of dynamical systems. One part is on the derivation of a low-dimensional model of a vibro-impacting mechanical system, numerical bifurcation analysis and comparison with an experiment. The other part is devoted to dimension reduction via the approximation of $k$-dimensional attracting invariant submanifolds of high-dimensional dissipative dynamical systems, with an example application from mechanics.

The thesis consists of an introduction to the applied mathematical methods and theory and three papers of which Paper A and Paper C are active parts of the thesis. Paper B is not discussed except for the part of the experimental results that were found due to the mathematical modelling found in this thesis. Paper A is introduced in Chapter 2 where it is to be read before Section 2.2; likewise Paper C is to be read before Section 3.3.

Lyngby, November 2013

Michael Elmegård

*To My Mother and Father*

# Acknowledgements

First and foremost I am very grateful to Associate Professor Jens Starke for his guidance, time and support both scientifically and personally, furthermore I am grateful for the freedom in choosing my own research direction. I am also very grateful for two co-supervisors, Associate Professor Anton Evgrafov (co-supervisor) and Associate Professor Jon J. Thomsen (co-supervisor) for their support and guidance which has been of great importance. Their doors were always open for questions and discussions.

I am also grateful for the collaborations I had with Emil Bureau, Frank Schilder, Ilmar Santos and Viktor Avrutin on the vibro-impacting beam. In particular, I am grateful for the discussions about the experiment and the experimental data with Emil Bureau and Frank Schilder. In addition, I am also grateful to Frank Schilder for his support in the continuation software CoCo and for the many discussions of the related mathematical theory.

During my years as a Ph.D. student at the Technical University of Denmark I have met many interesting and great people. I enjoyed my time at the former Department of Mathematics where I had many good colleagues. The same goes for my new colleagues in the Section of Dynamical Systems. Furthermore, I am very grateful to Christian Marschler for all the mathematical discussions and the many helpful remarks on the manuscript of my thesis. I am also grateful to Irene Heilmann and Søren Vedel for reviewing parts of my thesis.

I am also grateful for the collaboration with my hosts Professor Bernd Krauskopf and Professor Hinke Osinga during my research stay at the Department of Mathematics at the University of Auckland. It was a great learning experience both

mathematically and personally. Furthermore, I am grateful for the way I was included in the Ph.D. group in Auckland, I got some good friends there and I have already been visited in Copenhagen by one of them and look forward to host more of such visits.

# Contents

Chapter 1

# Introduction

The current chapter is written in order to provide a reasonable basis for an *intuitive* understanding of Chapters 2 and 3 and Papers A and C; for all the theory that is presented, we refer to sources that we found particularly useful to consult for detailed presentations. Furthermore, the chapter was written with the intention to give readers the possibility of getting a feel for some very useful and powerful methods in applied mathematics and a shortcut to understanding illuminating concepts that were initially troubling for this author[1] to wrap his head around. That being said, the presentation assumes a certain amount of familiarity with mathematical analysis and ordinary differential equations (ODE). A topic which is only implicitly explained is *numerical analysis*; while it is central to the practical calculations, implementations, verifications and analysis throughout the work, it is not particularly necessary in order to understand the results.

In Section 1.1 and Appendix D we derive and discuss the relevant beam theory; in Section 1.2 we describe the Galerkin principle which is very practical to get an understanding of partial differential equations (PDE) by turning them into often less complicated ordinary differential equations (ODEs); in Section 1.3 we describe some of the general ideas of continuation and bifurcation analysis; and discuss the practical aspects in 1.4, specifically we describe its application to one of the most fundamental problems of mathematical physics, the boundary

[1] author:Michael Elmegård

value problem (BVP); in Section 1.5 we introduce the notion of the *skeleton* of a dynamical system and shortly discuss the concept of invariant manifolds; this concept is very central to the theme of the thesis – *Dimension Reduction*.

## 1.1 Euler-Bernoulli beam theory

We shall give a minimal introduction to the main mechanical object that is considered in this thesis, namely the cantilever beam. As a service to the reader we present a more detailed account of the topic of beam theory in Appendix D. In the Appendix we consider a beam as a one-dimensional "body" and then give the relations to a more general beam that may change its cross-sectional geometry and material properties, i.e., we relate the one-dimensional theory of rods to the three-dimensional theory of beams. This is relegated to the Appendix because it is not strictly necessary to understand in high detail but it does facilitate a better understanding of the mechanics used throughout the thesis. It provides the means to evaluate if mechanical simplifications are expected to be valid approximations. The presentation is based on [LL86], [Ant06], [Kla06].

The equations of motion of the small transverse vibrations of a beam may be derived by, e.g., Newton's laws, Eulers laws or Euler-Lagrange equations. In the Appendix we derive it from Eulers laws so let us consider the approach of Euler-Lagranges equations. The assumption is that the potential energy from the displacements in the beam is determined by the curvature $\partial_{zz}u$, the elastic modulus $E$ of the beam and the cross-sectional moment of inertia $I$. The potential energy $V$ of the planar deformations of a straight beam of length $L$ is given by

$$V = \int_0^L \frac{1}{2} EI \left( \frac{\partial^2 u}{\partial z^2} \right)^2 \mathrm{d}z, \tag{1.1}$$

where $u(z)$ is the transverse displacement in the $x$-direction of the beam at the

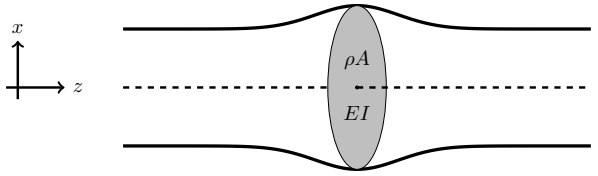


Figure 1.1: System sketch of a free beam, with coordinate system and physical properties. The dashed line denotes the center-line that is displaced by $u$ in the $x$-direction for a given position $z$.

$z$-position. We skipped the step going from three-dimensional beam to the one-dimensional beam, so $E$, $I$ are in general dependent on the $z$-coordinate unless the beam has constant cross-sections and material parameters. The same goes for the kinetic energy $K$ of the beam, here we immediately obtain,

$$T = \int_0^L \frac{1}{2}\rho A \left(\frac{\partial^2 u}{\partial t^2}\right)^2 \, \mathrm{d}z, \tag{1.2}$$

where $\rho$ is the material density and $A$ is the cross-sectional area of the beam, both quantities are in general dependent on $z$. Using Euler-Lagrange equation on the Lagrangian $L = T - V$ we obtain

$$\int_0^L \rho A \frac{\partial^2 u}{\partial t^2} + EI \frac{\partial^4 u}{\partial z^4} \;\; \mathrm{d}z = \int_0^L F(z,t) \;\; \mathrm{d}z, \tag{1.3}$$

where we added a forcing term. From this derivation we see that the terms on the left-hand side are the linear momentum of the beam and the elastic resistance force, respectively; note that a straight beam has vanishing potential energy. The local PDE form is

$$\rho A \frac{\partial^2 u}{\partial t^2} + EI \frac{\partial^4 u}{\partial z^4} = F(z,t), \tag{1.4}$$

and this is known as Euler-Bernoullis beam equation. One of the reasons for providing some detail about the mechanics at this stage is described quite well in a quote of John von Neumann [Dys04]

> With four parameters I can fit an elephant, and with five I can make him wiggle his trunk.

In other words it makes sense to base the mathematical modelling on the theory of mechanics such that the model is a product of reasoning and not simply a fitting task; in particular all terms and parameters have a physical interpretation and parameters may be estimated and this brings us to the next section on Galerkins principle.

## 1.2 Galerkin principle

In this section we describe one of the very important methods of applied mathematics, namely Galerkins method. In the derivation of the governing equations for problems in applied mathematics, e.g., from fluid dynamics to electrodynamics to quantum mechanics and back to structural mechanics, PDEs emerge naturally.

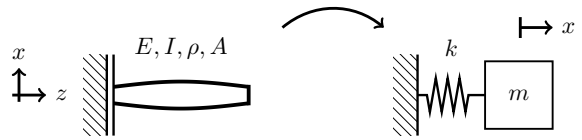


Figure 1.2: The Galerkin principle for the cantilever beam with a single mode approximation. The PDE is transformed into a single degree of freedom ODE.

In the cases where analytical solutions are attainable it makes sense to get an understanding from the analytically given families of solutions; additionally we may obtain useful information, such as, boundedness of solutions, the nature of dissipation and global attractors. In the general nonlinear case it is often difficult to understand, even qualitatively, the actual dynamics of the PDEs. The a priori knowledge is mostly limited to statements about the appropriate Sobolev spaces in which we should find our solutions; for all practical purposes this is unsatisfactory unless the ambition is to see the convergence of a numerical scheme. We note that the most useful insight may often be based on *Dimensional analysis* and *Scaling analysis* [Bar96][Hun67]. (See [dH56] for an excellent example in self-excited mechanical vibrations on oil-whirl).

In Paper A we apply the Galerkin principle as a method to obtain the proper structure of the vibro-impacting system, and also to argue about orders of parameters. In Appendix E we describe the princple by considering the simple example of applying Galerkins principle to the forced vibrations of the cantilever beam (cf. Equation (1.4)).

The Galerkin principle is illustrated in Figure 1.2 From Appendix E we observe that a single mode $\phi_1$ approximation may be used to obtain the following ODE approximation of the beam

$$0 = m\ddot{a} + ka - f(t), \tag{1.5}$$

where

$$\begin{aligned} m &= \int_0^L \rho A \phi_1 \phi_1 \mathrm{d}z, \\ k &= \int_0^L EI \frac{\partial^2 \phi_1}{\partial z^2} \frac{\partial^2 \phi_1}{\partial z^2} \mathrm{d}z, \\ f(t) &= \int_0^L F(z,t) \phi_1 \mathrm{d}z, \end{aligned} \tag{1.6}$$

this is a single degree-of-freedom model. In most textbooks, the process is to start with single degree-of-freedom models and then building up the complexity from there. The reader will quickly experience that the identification of distributed/continuous (PDE) problems as low-dimensional (ODE) problems is far

from trivial in anything but the exceptionally simple cases. When models become more complicated, e.g., model parameters $\rho, A, E, I$ are not constant but instead functions of the position in the cantilever and the cantilever is substituted by a more complicated beam shape, the reduction steps will seem increasingly coincidental. Starting instead with the weak form facilitates a systematic derivation and understanding of the geometric complexity and the parameters of the ODE through the integral relations (1.6). Lastly, the most difficult part is to have some a priori understanding of the qualitative behavior of the low-dimensional ODEs, and a necessary prerequisite for this is some knowledge of dynamical systems[2].

Often the starting point of a modeling task will be data from experimental measurements, and in this case the observed dynamics restricts the class of suitable models considerably. In Paper A the qualitative behaviour is partly known a priori from experiments, and this already sets constraints on the model choices, e.g., the most trivial example is that if an experiment shows nonlinear behavior then linear models are not suitable. More complicated examples could be experiments that show limit sets that may only be embedded[3] in dimension $> 2$, e.g., *chaos*; or chemical systems with time-scale separation where one should perhaps apply slow-manifold reduction. We further remark that Galerkin approximations have been frequently used in the context of applications of center manifold reduction in dynamical systems, see e.g., [Hol77][MH79] or Guckenheimer and Holmes [GH83, § 7.6] and references therein.

## 1.3 Continuation and bifurcation analysis

We start this section of by explaining a few general concepts that are essential to understand *continuation* and *bifurcation* theory properly. Consider the following general zero problem,

$$F(X) = 0, \tag{1.7}$$

where $X \in \mathbb{R}^N$, $F : \mathbb{R}^N \to \mathbb{R}^n$ is smooth and $N > n > 0$. Assume that the point $X = X^0$ is a solution to the zero-problem, $X^0$ can either be a *regular* or a *critical* point. *Regular* points are characterized by $F(X^0) = 0$ and that the Jacobian $\partial_X F(X^0)$ having maximal rank $n$; if the Jacobian of such a point does not have maximal rank then the point is *critical*. From here it is possible to proceed systematically only using results from analysis, however, we will try to describe the geometric nature of the subject.

[2]This is one of the main reasons why standard dynamical systems such as Duffing, van der Pol, Mathieu and combinations are studied so intensely in Dynamical Systems courses.

[3]We are considering vector fields and not maps in this discussion.

First we note that the maximal rank condition on the derivative $\partial_X F$ is the strongest that we may assume. In differential topology formulation this is equivalent to demanding that the derivative is a surjective map and in turn we call $F$ a submersion at $X^0$. Local submersions have a particularly simple interpretation, they mean that $F$ behaves as a linear mapping and in fact we may choose local coordinates, to obtain the canonical submersion, i.e.,

$$F(X) = (X_1, \ldots, X_n). \tag{1.8}$$

The implications of this is that at regular points the local zero-set of $F^{-1}(0)$ is simply $(0, \ldots, 0, X_{N-n}, \ldots, X_N)$, i.e., the solution set is the most trivial $(N-n)$-dimensional manifold that we can think of. It follows that if every point $X \in F^{-1}(0)$ is a regular point, i.e., $\text{Rank}(\partial_X F(X^0)) = n$ for all $X^0 \in F^{-1}(0)$, then $F^{-1}(0)$ is a smooth submanifold of $\mathbb{R}^N$ and $\dim(F^{-1}(0)) = \dim(\mathbb{R}^{\mathbb{N}}) - \dim(\mathbb{R}^n) = N - n$; this is known as the *pre-image theorem*, see Guillemin and Pollack [GP10][4]; note that this is equivalent to the finite-dimensional Implicit Function Theorem (IFT). A way to get some intuition for the consequences of this theorem on submersions is to consider some well-known manifolds with easy representations, e.g., a simple example is to consider,

$$f(x) = x_1^2 + x_2^2, \tag{1.9}$$

and the derivative becomes,

$$\partial_x f = (2x_1, 2x_2). \tag{1.10}$$

So, $f : \mathbb{R}^2 \to \mathbb{R}$ is a smooth function and the derivative has maximal rank everywhere except at the origin. It follows that $f^{-1}(1)$ is a 1-dimensional manifold and it happens to be the circle with unit radius. The corresponding results may be deduced with little effort for $n$-dimensional spheres.

*Continuation methods* are mainly applied in order to take advantage of this local structure to cover the zero-sets of nonlinear equations, and by application of the pre-image theorem or the IFT we simply find the zero-set in a neighborhood and advance the boundary via a new neighborhood. In Figure 1.3 we illustrate the advancement of a cover on the two-dimensional sphere.

[4]The book was originally published by Prentice-Hall in 1974. The first line of the Preface is "The intent of this book is to provide an elementary and intuitive approach to differential topology"; we highly recommend this book as well as the original inspiration for it, namely Milnor's *Topology from a differential viewpoint* of 1965 [Mil97].

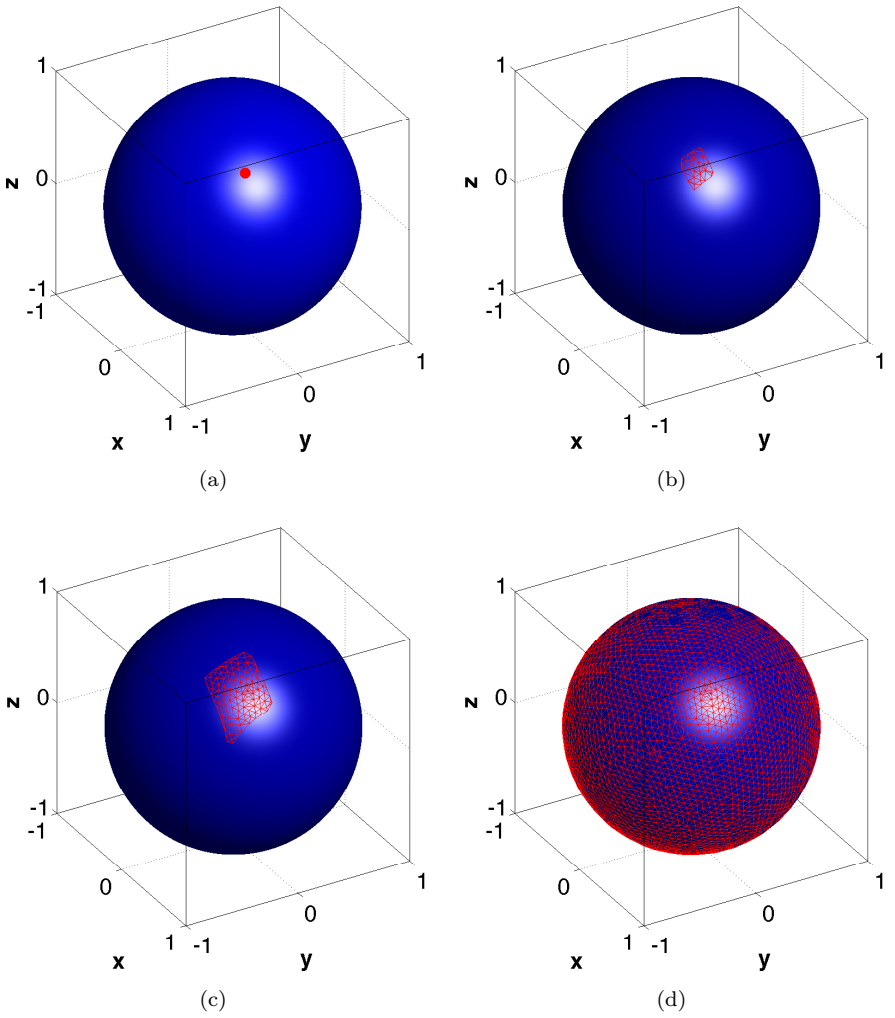


Figure 1.3: The advancement of a two-dimensional cover of the zero problem of the two-dimensional sphere, i.e., $f(x, y, z) = 1 - (x^2 + y^2 + z^2) = 0$. Panel (a) shows the initial solution point marked by the red bullet. Panel (b) shows the advancement of a cover (triangulation) of the zero set. Panel (c) further advancement and Panel (d) a complete cover. The continuation was performed using CoCo and adapting a demo on the sphere.

While the covering is a technical task to implement, the real difficulty often lies in the work that comes before, i.e., the construction of an interesting regular continuation problem $F$ and then the more detailed analysis of the zero sets; especially at critical points $X^0$, i.e., points where $F(X^0) = 0$ and $\mathrm{Rank}(\partial_X F(X^0)) < n$, the solution sets may be arbitrarily complicated. This leads us to the topic of *bifurcation theory*.

This section on bifurcation theory is by no means complete, and proper reference is given to books that address the topic in some detail, e.g., [Sey10][Wig03][Kuz04] or via the singularity theory approach presented in [GS85]. Usually, mathematical models of physical systems are dependent on a set of parameters $\lambda \in \mathbb{R}^k$, i.e., in this case there are $k$ model parameters. Often, as we discussed in a previous section on modeling, the parameters and possibly also the differential equations are only known within limited precision, and within this interval it makes sense to demand that the results of the mathematical model does not vary with small perturbations; this leads to questions of structural stability, genericity and transversality, all of which are beyond the scope of this brief introduction. We only try to paint a simple picture of the general ideas of bifurcation theory. Consider the following mathematical model,

$$\dot{x} = F(x, \lambda), \tag{1.11}$$

where $(x, \lambda) \in \mathbb{R}^{n+k}$ and $F : \mathbb{R}^{n+k} \to \mathbb{R}^n$ is a smooth function. Note that in the following we describe some local bifurcation theory in the context of rest/equilibrium/fixed points, explicitly. We consider the geometry of the zero sets of $F$ under parameter variations, i.e., we investigate the geometric properties of $\Gamma = \{(x, \lambda) : F(x, \lambda) = 0\}$ for relevant parameter regimes, i.e., it is the study of a $k$-parameter family of differential equations or vector fields. For the purpose of simplicity we consider the following setting,

$$g(y, \lambda) = 0, \tag{1.12}$$

where $(y, \lambda) \in \mathbb{R} \times \mathbb{R}$ and $g : \mathbb{R} \times \mathbb{R} \to \mathbb{R}$ is a smooth function. This may seem to be a rather crude assumption, but it is in fact very likely to be the case that high-dimensional, even infinite-dimensional, dynamical systems can be reduced in such a way near rest points via the Lyapunov-Schmidt reduction, see [GS85], where the proof is done for the minimally degenerate case, i.e., $F(x^0, \lambda^0) = 0$ and $\mathrm{Rank}(\partial_x F)_{(x^0,\lambda^0)} = n-1$.[5] In the context of continuation we referred to such points as critical, in the current context they are often called *singularities*. The term *bifurcation* was coined by Henri Poincaré, the father of

[5] Consider the set of $n \times n$ matrices, then the submanifold of matrices with rank $r$ has codimension $(n-r)^2$, hence the minimally degenerate matrices has smaller codimension[Arn81] than the latter, i.e., the minimally degenerate matrices are much more likely to be encountered when we perform parameter variations; the rationale behind this type of reasoning will be described later.

qualitative analysis of dynamical systems, in the second half of the 19th century. To 'bifurcate' means to divide in two, and in our context a *bifurcation point*, a bifurcation point is given at the parameter values for which the qualitative dynamics change, i.e., a value at which we can not identify the orbits of an original vector field uniquely into the orbits of the perturbed vector field; the precise concept is topological conjugacy. A *singularity* for our reduced function $g$ is a point $(x^0, \lambda^0)$ where $g(x^0, \lambda^0) = \partial_x g(x^0, \lambda^0) = 0$. Using the implicit function theorem we immediately see that any bifurcation point is a singularity.

By example, we will try to motivate the reasons why bifurcation analysis and structural stability are essential concepts in nonlinear systems; consider the following dynamical system,

$$\dot{x} = f(x) = x^3, \tag{1.13}$$

where there is only one rest point given at the origin $x = 0$; observe that the origin is a singularity since $f(0) = \partial_x f(0) = 0$. This is unlikely to be a realistic model for any real-world application, for if we consider any linear perturbation,

$$\dot{x} = g(x, \lambda) = x^3 - \lambda x, \tag{1.14}$$

with $\lambda > 0$, we observe that two rest points have emerged next to the rest point at the origin. The zero-set of $g$ is

$$\Gamma = \{(x, \lambda) : 0 = x \vee 0 = \lambda - x^2\}, \tag{1.15}$$

and in Figure 1.4 we observe $\Gamma$ is not a 'nice' and smooth manifold, in particular,

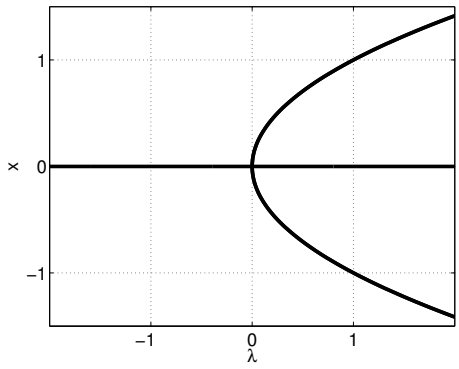


Figure 1.4: Pitchfork $\Gamma = \{(x, \lambda) : 0 = x \vee 0 = \lambda - x^2\}$, notice the singular point at the origin.

the origin $(x, \lambda) = (0, 0)$ is an unnatural point because three rest points of the system collapse to one at the same position – such a point is referred to as a

*branching point*. This type of zero set $\Gamma$ is known as a pitchfork. Consider the addition of a constant term,

$$\dot{x} = h(x, \lambda, \alpha) = x^3 - \lambda x + \alpha, \tag{1.16}$$

where $\alpha \neq 0$ but sufficiently small, in this case $\Gamma$ is a disconnected set composed of two smooth manifolds.

Equation (1.16) is the so-called cusp normal form and it happens to be a versal unfolding of $x^3$, meaning that any $C^1$ perturbation of the vector field will not change the structure in a neighborhood of $(x, \lambda, \alpha) = (0, 0, 0)$. The zero set of $h(x, \lambda, \alpha)$ is the cusp surface and it is shown in Figure 1.5; note that the cusp surface has multiple solutions in certain parameter regions of $(\lambda, \alpha)$. In

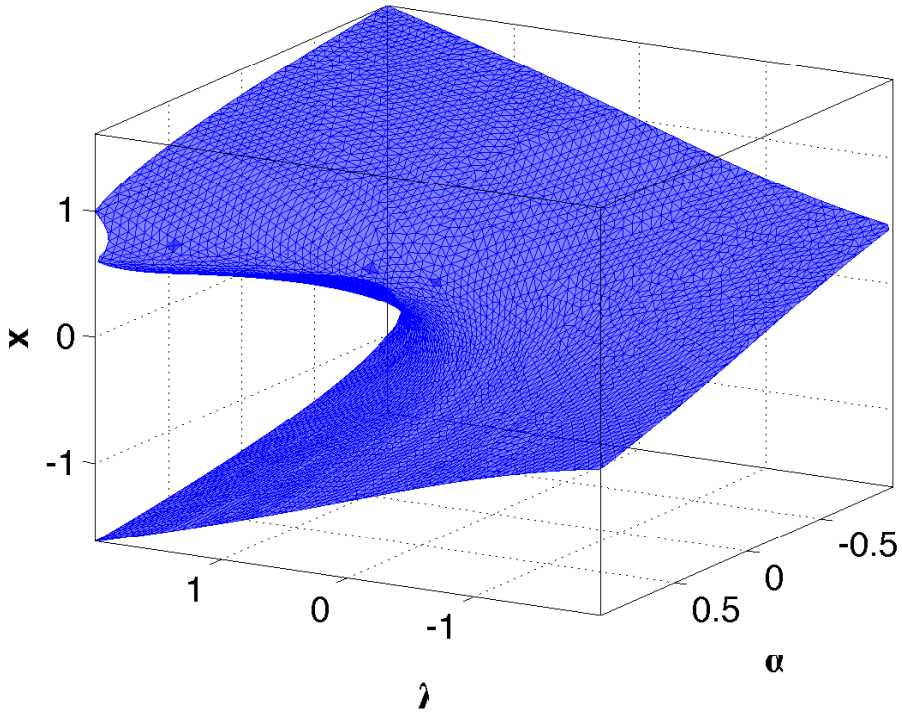


Figure 1.5: The cusp surface, i.e., the zero set of $h(x, \lambda, \alpha) = x^3 - \lambda x + \alpha$. The figure is produced using CoCo [DS13] and adapting a demo on the cusp normal form. (CoCo is applying a two-dimensional covering algorithm to chart the zero set; we observe the triangulation on the surface).

Figure 1.6 we added a curve and a point to the surface; observe that the special

points of the surface is basically given by the red curve(s); and special point of the red curve(s) is given by the black bullet. In this example the bifurcation points are exactly the points traced out by this set and bifurcation theory offers a systematic handling of these points based on a finite number of derivatives. In the present case two types of bifurcation points are observed; the vertical tangents and the point where they collide.

The bifurcation points that we consider on the cusp surface are fold points[6] and a cusp point. We can classify these bifurcation points by evaluating a few derivatives; this can be done by solving the *recognition problem* [GS85]. Fold points are recognized by the following conditions,

$$\begin{aligned} h &= 0, \\ h_x &= 0, \end{aligned} \tag{1.17}$$

to these conditions we add so-called nondegeneracy conditions,

$$\begin{aligned} h_{xx} &\neq 0, \\ h_\lambda &\neq 0. \end{aligned} \tag{1.18}$$

Using the two strict equalities the locus of possible fold points is given by

$$\Gamma_{\text{fp}} = \left\{ (x, \lambda, \alpha) : x = s, \lambda = 3s^2, \alpha = 2s^3, s \in \mathbb{R} \setminus \{0\} \right\}, \tag{1.19}$$

note that the origin does not satisfy the nondegeneracy conditions. The locus of fold points and together with the cusp point are shown in Figure 1.6. In Figure 1.7 we illustrate how the pitchfork relates to the cusp surface. The cusp point is recognized from the following conditions,

$$\begin{aligned} h &= 0, \\ h_x &= 0, \\ h_{xx} &= 0, \end{aligned} \tag{1.20}$$

to these conditions we add the nondegeneracy condition

$$\begin{aligned} h_{xxx} &\neq 0, \\ h_\lambda h_{x\alpha} - h_\alpha h_{x\lambda} &\neq 0. \end{aligned} \tag{1.21}$$

These where two simple examples of how special points may be classified using bifurcation theory. We remark that the theory of unfolding and finding the criterions for all the bifurcations is non-trivial, and as the number of unfolding parameters increase the complexity explodes; this is not a huge problem in applications because one typically observes bifurcations that are unfolded by one or two parameters.

[6] or saddle nodes or limit points.

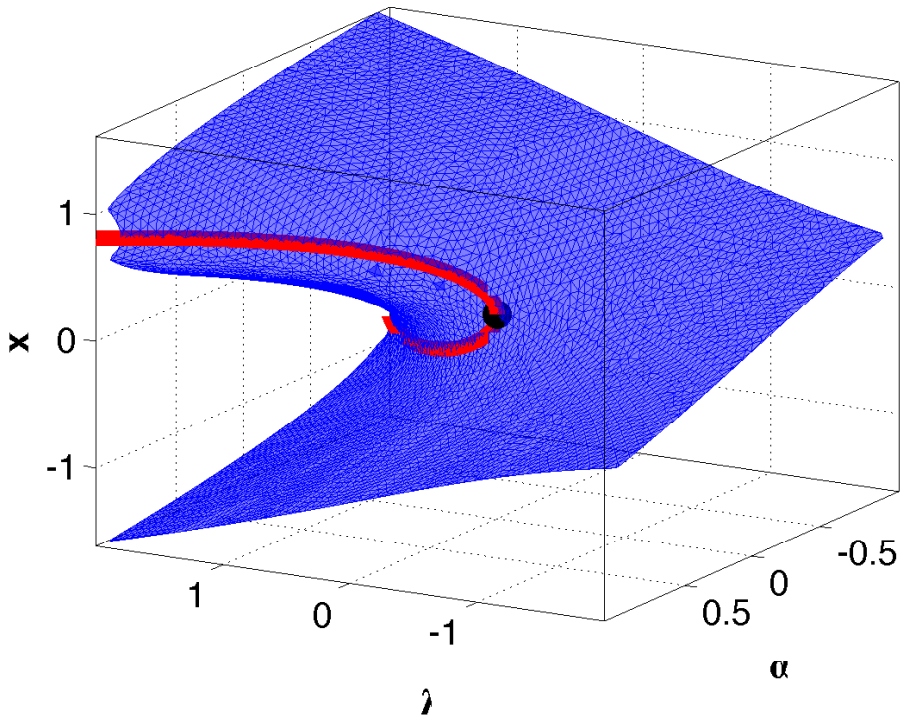


Figure 1.6: The cusp surface, i.e., the zero set of $h(x, \lambda, \alpha) = x^3 - \lambda x + \alpha$, with the fold point loci $\Gamma_{\text{fp}}$ given by the (two) red curves and the cusp point given by the black bullet.

With the starting point of a the cusp normal form $h(x, \lambda, \alpha)$, see Equation (1.16), a geometric 'viewpoint' may provide a little extra insight in some of the details without getting to concrete wrt. mathematical details.

The mapping $h$ is regular, e.g., the derivative has maximal rank 1 throughout,

$$(h_x, h_\lambda, h_\alpha) = (3x^2 - \lambda, -x, 1), \tag{1.22}$$

and by the implicit function theorem (or the pre-image theorem) the solutions set to $h(x, \lambda, \alpha) = 0$ is a two-dimensional submanifold in $\mathbb{R}^3$.

For the fold points an additional strict equality is imposed together with two nondegeneracy conditions, see Equations (1.17) and (1.18). The geometric significance of the conditions are the following. The equality constraint is a vertical

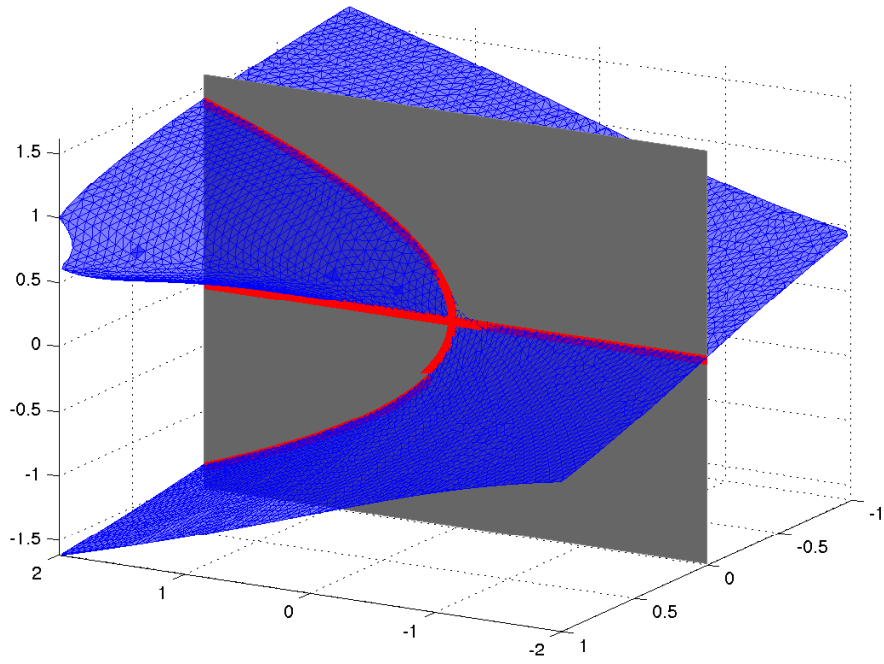


Figure 1.7: The cusp surface and the Pitchfork: Panel (a) shows that the pitchfork (the set marked by black) is the intersection between the hyperplane defined by $\alpha = 0$ and the cusp surface; imagine how the zero set breaks if $\alpha \neq 0$.

tangency and combined with the non-degeneracy conditions it implies that the solution curve folds and for parameter changes this means that we may go from zero to two solutions and vice versa. The non-degeneracy conditions simply means that we demand that the curve of fold points is regular, i.e., the map $(x, \lambda, \alpha) \mapsto (h, h_x)$ must have maximal rank and if we consider $\alpha$ constant then this amounts to

$$\det \begin{pmatrix} h_x & h_\lambda \\ h_{xx} & h_{\lambda x} \end{pmatrix} = h_x h_{\lambda x} - h_\lambda h_{xx} = -h_\lambda h_{xx} \neq 0, \tag{1.23}$$

hence $h_\lambda \neq 0$ and $h_{xx} \neq 0$.

For the cusp points the story is very much the same. Equality and non-degeneracy constraints are given by Equations (1.20) and (1.21). The equality constraints are only met at the origin for the cusp surface, this is the isolated point where the two fold curves meet. The non-degeneracy conditions are again

simply a regularity condition of the map $(x, \lambda, \alpha) \mapsto (h, h_x, h_{xx})$, i.e.,

$$\det \begin{pmatrix} h_x & h_\lambda & h_\alpha \\ h_{xx} & h_{x\lambda} & h_{x\alpha} \\ h_{xxx} & h_{xx\lambda} & h_{xx\alpha} \end{pmatrix} = \det \begin{pmatrix} 0 & h_\lambda & h_\alpha \\ 0 & h_{x\lambda} & h_{x\alpha} \\ h_{xxx} & h_{xx\lambda} & h_{xx\alpha} \end{pmatrix} \neq 0, \tag{1.24}$$

hence $h_{xxx} \neq 0$ and $h_\lambda h_{x\alpha} - h_\alpha h_{x\lambda} \neq 0$.

From the above descriptions, it should be understood that in our example the fold points are more likely to encounter compared to the isolated cusp point, and this is explained by the concept of codimension. The fold bifurcation is a codimension 1 bifurcation, and there are at least two ways to observe this; it can be seen from the number of unfolding parameters in its normal form; it can be found from the number of additional equality constraints in the recognition problem. In a geometric sense each additional equality lowers the dimension of the solution manifold by one. The codimension of a manifold $W \subset V$ is given as

$$\operatorname{codim}(W) = \dim(V) - \dim(W). \tag{1.25}$$

hence in the current example, if we call the cusp surface $V$ and the fold point curve $W$, then we immediately see that the fold point bifurcation is codimension one. This interpretation generalizes better to models with more parameters, because it is then reduced to a question of how certain submanifolds relate to the manifolds in which they reside. Likewise, the cusp bifurcation was recognized by additional constraint of $h_{xx} = 0$, hence from the previous interpretation we immediately see that it is a codimension-two bifurcation.

The geometric significance of the codimension of a bifurcation is that it provides a hierarchy of how likely certain bifurcations are to encounter. Codimension-one bifurcations, are boundaries that can separate domains, e.g., half line of a football field, we cross it regularly if we move around; by the same analogy, a codimension-two bifurcation is then the centre spot of a football field, and so we can go to it if we make the effort. The fold and Hopf bifurcation are commonly encountered examples of codimension-one bifurcations. From an applied point of view, caution is therefore to be taken wrt. mathematical models that present bifurcations of a higher codimension; in general such mathematical models are unlikely to explain real-world applications properly unless they emerge by an idealistic symmetry assumption.

## 1.4 Practical continuation and bifurcation analysis

In this section some of the practical aspects of the numerical implementation of continuation and bifurcation methods is presented. Consider a continuously differentiable function $F(X)$,

$$F : \mathbb{R}^{n+k} \to \mathbb{R}^n, \tag{1.26}$$

and assume that $F(X_0) = 0$ where $X_0, \in \mathbb{R}^{n+k}$ is a regular point, i.e., $F_X(X_0)$ has $\text{Rank}(F_X(X_0)) = n$. In this situation it was explained in Section 1.3 that the solution set is diffeomorphic to a k-dimensional hyperplane, but this is not a practical starting point for computations. Equivalently, we may instead use that the implicit function theorem provides the existence and uniqueness of a smooth $k$-dimensional manifold Z in the neighborhood of $X_0$ that solves $F(X) = 0$. Consider then all the smooth curves $\gamma : \mathrm{I}_\epsilon \to \mathbb{R}^{n+k}$ with the open interval $\mathrm{I}_\epsilon = (-\epsilon, \epsilon)$, the base point $\gamma(0) = X_0$ and $\gamma(t) \in \mathrm{Z}$; by definition $F(\gamma(t)) = 0$.

$$F(\gamma(t)) = 0, \qquad t \in \mathrm{I}_\epsilon \tag{1.27}$$

$$\Rightarrow \qquad \partial_t F(\gamma(t))\big|_{t=0} = F_X(\gamma(t)) \cdot \gamma'(t)\big|_{t=0} = 0. \tag{1.28}$$

The tangent space of Z at $X_0$, $\mathrm{TZ}_{X_0}$, is the span of the tangents of all the curves $\gamma$ at $t = 0$ (i.e. at $X_0$), and it can be shown that

$$\mathrm{TZ}_{X_0} = \text{null}(F_X(X_0)) = \text{span}(v_1, v_2, \ldots, v_k), \tag{1.29}$$

where $v_i, w_i \in \mathbb{R}^{n+k}$. We further assume that the $v_i$'s constitute an orthonormal basis of the null space and let $w_i$ with $i = 1, \ldots, n$ be a basis for the orthogonal complement. It follows from the implicit function theorem that in a sufficiently small neighborhood of $X_0$ the zero set Z may be parameterized by $p = \sum_{i=1}^{k} p_i v_i$ where $p_i \in \mathbb{R}$, i.e.,

$$\mathrm{Z} = \left\{ X \in \mathbb{R}^{n+k} : X = X_0 + \sum_{i=1}^{k} p_i v_i + \sum_{j=1}^{n} x_j v_j \text{ and } x_j = h_j(p) \right\}. \tag{1.30}$$

As an example we could consider the k-dimensional disc of radius $R$ attached at $X_0$ and spanned by the orthonormal basis of the tangent space $v_i$; for $R$ sufficiently small we can determine all $x_j = h_j(p)$ inside the disc via Newton's method. This means that we can *locally* limit our focus to the case,

$$F : \mathbb{R}^n \times \mathbb{R}^k \to \mathbb{R}^n \tag{1.31}$$

where $x \in \mathbb{R}^n$, $p \in \mathbb{R}^k$ and $F_x(x,p)$ is nonsingular. As long as the implicit function theorem does not fail, the front of the cover can be advanced without changing coordinate system and we simply patch together the discs; like the charts of an atlas. We remark that it is not a trivial task to implement k-dimensional covering algorithms, see e.g., Henderson's paper on multi-parameter continuation [Hen02]. With this discussion we only scratched some of the fundamental principles of $k$-parameter continuation.

We remark that continuation is typically applied as one-parameter continuation, i.e., set $k = 1$ in Equation (1.26).

The subject of continuation is not to be confused with bifurcation analysis; continuation is not limited to the computation of certain families of special solutions connected to bifurcations. As an example, one may ask for the family of all solutions to $F(x,\lambda) = 0$ with the additional constraint that a scalar function $\psi(x,\lambda) = 0$. We remark that $\psi(x,\lambda)$ can be arbitrarily chosen, e.g., $\lambda_3 x_1 x_{13} - c = 0$. If an initial solution is not provided then there are different strategies to finding one. One way is to continue families of solutions while monitoring if $\psi(\mathbf{x},\lambda)$ changes sign and thereby finding $\psi(x,\lambda) = 0$, if this happens we have an initial solution and the new system that is continued is,

$$\begin{aligned} F(x,\lambda) &= 0, \\ \psi(x,\lambda) &= 0. \end{aligned} \tag{1.32}$$

This process can be repeated, i.e., constraints can be further added or released as one likes. In [DS13] a rather general formalism to practical implementation of *continuation problems* is developed, explained and exemplified together with the Matlab continuation toolbox CoCo [DS].

In the context of bifurcation analysis the scalar functions $\psi(x,\lambda)$ are called test-functions, and the structure of these functions are related to the *recognition problem*. If we are interested in for example fold points then while continuing a regular family of solutions of $F(x,\lambda) = 0$ we monitor the appropriate test function say $\psi_{\text{fold}}(x,\lambda)$; if $\psi_{\text{fold}}(x^0,\lambda^0) = 0$ then $(x^0,\lambda^0)$ is marked as a fold point along the branch. If we want to continue the branch of fold points we append the test function to the continuation problem, i.e.,

$$\begin{aligned} F(x,\lambda) &= 0, \\ \psi_{\text{fold}}(x,\lambda) &= 0. \end{aligned} \tag{1.33}$$

It should be mentioned that we left out some detail in this argumentation, the most important being that one must keep in mind that the value of $k$ is appropriate; in Equations (1.33) $k \geq 2$ because the number of continuation parameters $\nu$ is equal to the difference in the number of parameters $n + k$ and

the number of equations $n+1$, hence

$$\nu = (n+k) - (n+1) = k - 1 > 0. \tag{1.34}$$

This sort of counting which is based on the implicit function theorem is essential to constructing well-posed continuation problems. This implies that in order to be able to continue certain families of solutions we may need to include more parameters or simply let more parameters vary. The number $\nu$ defines the dimension of the covering algorithm that must be used, and typically parameters are fixed such that $\nu = 1$.

This compact overview to the subjects left out a lot of details, interested readers can consult, e.g., [Gov00][Kuz04] for numerical bifurcation analysis and [DS13] for a focus on continuation methods. Most importantly, note that there exist several software packages for performing numerical continuation and bifurcation analysis, e.g., AUTO [DPC+07], MATCONT[DGK03],CoCo[DS]. Generally it is possible to define a rather wide class of problems in the available software packages.

### 1.4.1 From infinite to finite dimension

In many applications in engineering and science the governing equations are formulated as differential equations. For the current analysis there is no need to be specific about time and space variables but it is merely noted that the infinite-dimensional systems may depend on several variables. Consider a general nonlinear differential equation[7],

$$N(u(x), \lambda) = 0, \tag{1.35}$$

where $u$ belongs to an appropriate infinite-dimensional function space with basis $\{\phi_i : i \in \mathbb{N}\}$and $\lambda \in \mathbb{R}^k$. It is only the exception to the rule that we may obtain a closed form analytical solution to Equation (1.35). Consider a numerical approximation of $u(x)$,

$$u_{\text{approx}}(x) = \sum_{i=1}^{n} a_i \phi_i(x), \tag{1.36}$$

where $\phi_i$ is the $i$th basis function and $a_i \in \mathbb{R}$ the coefficient to the $i$th basis function and $n$ is the cut-off number of basis functions. Substitution of

[7] We shall not worry about the details of functional analysis, but rather assume that these allow the following analysis.

Equation (1.36) in (1.35), satisfying boundary conditions and appropriate continuity/differentiability conditions throughout the domain yields an equation,

$$F(a, \lambda) = 0, \tag{1.37}$$

where $(a, \lambda) \in \mathbb{R}^n \times \mathbb{R}^k$, and we assume that $F : \mathbb{R}^{n+k} \to \mathbb{R}^n$ is sufficiently smooth. The main argument is that numerical approximations yield finite dimensional representations, note also that discretization schemes a la finite difference yield the same result.

### 1.4.2 A two-point boundary value problem

Consider the general nonlinear first order dynamical system,

$$\frac{\mathrm{d}x}{\mathrm{d}t} = f(x, \lambda), \tag{1.38}$$

where $f : \mathbb{R}^{n+k} \to \mathbb{R}^n$ is sufficiently smooth. Let $\phi(t, \cdot)$ denote the flow of Equation (1.38), i.e., $x(t + \tau) = \phi(t, x(\tau))$; note that the flow also depends on the parameter $\lambda$ but this is suppressed in our notation. The flow $\phi(t, \cdot)$ is known in closed form in many linear cases and only in exceptional cases for nonlinear equations, however, the flow may be approximated using numerical integrators. Note that the flow is also dependent on $\lambda$ but we do not write this dependence explicitly.

Considering a solution segment of the flow initialized at $x_0$ and with flow-time $\tau$ it is immediately clear that the segment is defined by $n + 1$ conditions. If on the other hand the solution segment is defined by $n + 1$ conditions where some values are specified at the initial point and the remaining at the end point of the segment, then the problem is much more complicated as it is not handled by direct integration and because solutions may not exist. In fact it is easy to come up with bvps where solutions do not exist. With these constructions in mind, we define the system

$$F(x^0, x^1, T, \lambda) = \begin{pmatrix} \phi(T, x^0, \lambda) - x^1 \\ f_{bc}(x^0, x^1, T, \lambda) \end{pmatrix} = 0, \tag{1.39}$$

where $\phi : \mathbb{R} \times \mathbb{R}^n \times \mathbb{R}^k \to \mathbb{R}^n$ and $f_{bc} : \mathbb{R}^n \times \mathbb{R}^n \times \mathbb{R} \times \mathbb{R}^k \to \mathbb{R}^{n+1}$. Assuming that $\partial_{(x^0, x^1, T)} F$ has maximal rank at a solution point $(x^{0*}, x^{1*}, T^*, \lambda^*)$, then by the implicit function theorem the local solution set is $k$-dimensional since $(n + n + 1 + k) - (n + n + 1) = k$. The simplest example possible is the initial value problem,

$$f_{bc}(x^0, x^1, T, \lambda) = \begin{pmatrix} x^0 - x^{0*} \\ T - T^* \end{pmatrix} = 0. \tag{1.40}$$

We did not discuss how to find an initial solution to the two-point boundary value problem because there is no unique way to do this except in simple cases.

The described method is typically not the method of choice, because it is much more unstable than alternatives such as multiple shooting or collocation methods. Multiple shooting is described quite nicely in [Sey10][Kuz04] and collocation is described in detail in [DS13], the latter is a type of discretization of the orbit segments by the use of (Lagrange) polynomials where all coefficients are then variables in the continuation problem, this method has good stability properties and it is trivial to increase the order of the numerical approximation, but the dimension of the continuation problem is also much larger than that of single shooting.

The important message of the section is that all of the mentioned techniques are used to turn infinite-dimensional bvps into finite-dimensional nonlinear equations; a process which leads us back to the problem of analyzing zero sets of nonlinear equations $F : \mathbb{R}^{n+k} \to \mathbb{R}^n$.

### 1.4.3 Linear stability of orbits

Consider again a nonlinear differential equation,

$$\frac{\mathrm{d}x}{\mathrm{d}t} = f(x, \lambda), \tag{1.41}$$

where $(x, \lambda) \in \mathbb{R}^{n+k}$ and $f$ is sufficiently smooth with flow $\phi(t, \cdot)$. We want to understand what happens in the neighborhood of a trajectory in the trivial case of an hyperbolic equilibrium point the neighborhood is understood via the eigenvalues of the linearization; for trajectories that evolve in time the question is more subtle. Consider a family of solutions,

$$x(t, \epsilon) = \phi(t, \tilde{x}^0 + \epsilon v), \tag{1.42}$$

where $v \in \mathbb{R}^n$, $\tilde{x}(t) = x(t, 0)$ and $\tilde{x}^0 = \tilde{x}(0)$ and $\epsilon \in \mathbb{R}$. The orbit of which we will investigate the neighborhood of is $\tilde{x}(t)$, i.e., this means that $\epsilon$ is to be understood as a perturbation parameter and the whole family of solutions could be restricted to the evolution of a ball around $\tilde{x}^0$. Consider the expansion in $\epsilon$,

$$\phi(t, \tilde{x}^0 + \epsilon v) - \phi(t, \tilde{x}^0) = \epsilon D\phi(t, \tilde{x}^0)v + \mathcal{O}(\epsilon^2), \tag{1.43}$$

where $D$ denotes $\frac{\partial}{\partial x_i}$. A practical interpretation of Equation (1.43), as $\epsilon \to 0$, is to consider $v$ as a vector with initial base point $\tilde{x}^0$, such that[8] $v_t := D\phi(t, \tilde{x}^0)v$ is interpreted as the vector with base point $\phi(t, \tilde{x}^0)$, i.e., the matrix $D\phi(t, \tilde{x}^0)$ contains information on local expansion and contraction of the trajectories.

By substitution in Equation (1.41) we have

$$\frac{\mathrm{d}}{\mathrm{d}t}\phi(t, x) = f(\phi(t, x), \lambda), \tag{1.45}$$

differentiating with respect to $x$ in order to obtain,

$$\frac{\mathrm{d}}{\mathrm{d}t}D\phi(t, x) = Df(\phi(t, \tilde{x}_0), \lambda)D\phi(t, x), \tag{1.46}$$

and observe that $D\phi(t, \tilde{x}^0)$ is the solution matrix to the linear equation with time-dependent coefficients,

$$\frac{\mathrm{d}X}{\mathrm{d}t} = A(t, \tilde{x}^0, \lambda)X. \tag{1.47}$$

Even though Equation (1.47) is linear, it is important to note that in the case with time-dependent coefficients there is no general solution method. Assume that $X(0) = I_n$ where $I_n$ is the $n \times n$ identity matrix, then $X(t)$ is called the principal fundamental matrix of solutions [Chi06].

At this stage we can be a bit more concrete about what happens to perturbations. Choose a flow time $T$ and suppose $u$ is a real eigenvector to matrix $X(T)$ with real eigenvalue $\mu$. Then the initial tangent vector is contracted or expanded by $|\mu|$,

$$||u_T|| = ||X(T)u|| = |\mu|||u||, \tag{1.48}$$

and this provides us with the stability information of the trajectory in a natural way. Thinking about how other trajectories in phase space relates to the orbit under consideration, e.g., some sets may approach the trajectory asymptotically in forward or backward time. The eigenvalues $\mu$ are called multipliers. Consider the special perturbation in the direction of the tangent to the trajectory,

$$\frac{\mathrm{d}}{\mathrm{d}t}\phi(t + s, x) = f(\phi(t + s, x)), \tag{1.49}$$

[8] Remember that when the flow is smooth this interpretation holds without adjustments in the limit

$$\lim_{\epsilon \to 0} \frac{\phi(t, \tilde{x}^0 + \epsilon v) - \phi(t, \tilde{x}^0)}{\epsilon} = D\phi(t, \tilde{x}^0)v. \tag{1.44}$$

differentiate with respect to $s$ at $s = 0$,

$$\frac{\mathrm{d}^2}{\mathrm{d}t^2}\phi(t+s,x)\big|_{s=0} = Df \cdot \frac{\mathrm{d}}{\mathrm{d}t}\phi(t+s,x)\big|_{s=0}, \tag{1.50}$$

$$\Rightarrow \quad \frac{\mathrm{d}}{\mathrm{d}t}f(\phi(t+s,x))\big|_{s=0} = Df \cdot f(\phi(t+s,x))\big|_{s=0}, \tag{1.51}$$

$$\frac{\mathrm{d}}{\mathrm{d}t}f(\phi(t,x)) = Df \cdot f(\phi(t,x)), \tag{1.52}$$

from the previous derivation of the fundamental solution matrix this implies (cf. Equation (1.46)) that the initial value problem $f(\phi(0,x))$ is solved by,

$$f(\phi(t,\mathbf{x})) = X(t) \cdot f(\phi(0,\mathbf{x})) = X(t) \cdot f(x), \tag{1.53}$$

As a special case consider, $\tilde{x}^0 = \phi(T,\tilde{x}^0)$, i.e., $\phi(t,\tilde{x}^0)$ is a periodic orbit of period $T$, then

$$f(\tilde{\mathbf{x}}_0) = f(\phi(T,\tilde{\mathbf{x}}_0)) = X(T) \cdot f(\tilde{\mathbf{x}}_0), \tag{1.54}$$

hence the tangent direction of the periodic orbit is an eigenvector with eigenvalue one, and it is called the trivial multiplier. The stability of the periodic orbit is determined by the eigenvalues of $X(T)$; if, for example, all eigenvalues are inside the unit circle except for the trivial one, then the periodic orbit is asymptotically stable. A hyperbolic[9] periodic orbit has a stable and unstable manifold that are tangent to the corresponding eigenspaces just as it is the case for equilibrium points. A slight twist is that the dimension of the stable and unstable manifolds add up to $n+1$ where $n$ is the phase-space dimension. The eigenvalues $X(T)$ are usually referred to as Floquet multipliers in the case of periodic orbits. In the continuation and bifurcation analysis of periodic orbits, the multipliers have an importance corresponding to that of eigenvalues of equilibrium points; this correspondence can be understood via the identification of a certain discrete map known as the *Poincaré map*, see e.g., [Rob98][Chi06]. The bifurcation points are related to the parameters at which the orbit fails to be hyperbolic, i.e., some non-trivial multiplier is on the unit circle.

This section on linear stability of trajectories is only a small taste of some possibilities in the analysis of dynamical systems. The discussion was limited to the stability of trajectories; we remark that the concept of linear stability is applied in a much more general setting of sets and higher-dimensional manifolds, in fact our Paper C applies theory which relies crucially on certain uniform estimates of the linear stability of a manifold (Generalized Lyapunov-type numbers [Fen71][Wig94] ).

[9] all eigenvalues $|\mu| \neq 1$ except for the trivial multiplier

### 1.4.4 Discontinuous piecewise-linear dynamical system

In Section 2.2 we analyze periodic orbits in a discontinuous piecewise-linear dynamical system, and while there are many similarities, there are also a few crucial differences, e.g., the traditional results on uniqueness and existence, dependence on parameters and such typically rely on Lipschitz continuous vector fields, and lowering the regularity introduces many new challenges, see e.g., [BBCK07]. In particular, as it was clear from the previous sections most of the methods in continuation and bifurcation analysis are developed in systems with a sufficient smoothness assumed.

For periodic orbits in smooth systems some of the necessary detail was described in Sections 1.4.2 and 1.4.3. In systems with nonsmooth events the principle is generalized a little, such as to accommodate piecewise smooth vector fields and jump discontinuities. In mechanical engineering applications piecewise-smooth vector fields emerge naturally, e.g., rotor and stator interaction or stick-slip in friction systems. Jump discontinuities are for example used to account for inelastic impact laws. It is natural to decompose periodic orbits of such dynamical systems in multiple segments and disregarding some subtle theoretical details the philosophy in the extension is really very simple; by a predefined decomposition the continuation problem becomes a finite sequence of (coupled) two-point boundary value problems.

We formulate a multisegment continuation problem via the flow $\phi(t,\cdot)$; consider an m-segment bvp and the continuation problem becomes,

$$\begin{aligned}
&\mathbf{x}_1 - g_1(\phi_1(T_1,\mathbf{x}_0,\lambda),\lambda) = 0,\\
&\mathbf{x}_2 - g_2(\phi_2(T_2,\mathbf{x}_1,\lambda),\lambda) = 0,\\
&\vdots\\
&\mathbf{x}_m - g_m(\phi_m(T_m,\mathbf{x}_{m-1},\lambda),\lambda) = 0,
\end{aligned} \tag{1.55}$$

where $g_i$ may be a jump discontinuity. Let the dynamical system be $n$-dimensional and the model parameters $\lambda \in \mathbb{R}^k$ then the continuation problem has $mn$ equations and $(m+1)n+m+k$ unknowns, hence considering the implicit function theorem under the assumption that the mapping is regular the covering of the zero set is $(n+m+k)$-dimensional. As usual we begin by fixing $(k-1)$ of the model parameters. The underdetermination of the $(n+m)$-variables can in a less general interpretation be attributed to a deficit of $n$ boundary conditions that are needed in the determination of the traditional two-point boundary value problem for orbits, while the deficit of $m$ is attributed to the conditions that should be inferred because of the $m$-segmentation.

The addition of the $(n+m)$ conditions is to be understood in the highest gen-

erality, i.e., we should first of all understand that we can compute arbitrary families of solutions; in the light of the current application we step down for the application to the very special class of orbits that are periodic. In fact as we will now show this is a rather trivial problem to define by restricting the previous continuation problem (1.55), by adding the periodic boundary condition $(n+1)$ and $m-1$ other conditions,

$$\begin{aligned}
&\mathbf{x}_m - \mathbf{x}_0 = 0,\\
&T - (T_1 + T_2 + \ldots + T_m) = 0,\\
&h_1(\mathbf{x}_i, T_i, \lambda) = 0,\\
&h_2(\mathbf{x}_i, T_i, \lambda) = 0,\\
&\vdots\\
&h_{m-1}(\mathbf{x}_i, T_i, \lambda) = 0,
\end{aligned} \tag{1.56}$$

where each $h_i$ is a scalar function and by $(\mathbf{x}_i, T_i, \lambda)$ we mean all variables and parameters may be used as input. With the addition of the $(n+m)$ equations the continuation problem has one free parameter left, hence given an initial solution the problem is a one-parameter continuation problem. Usually, the $h_i$ scalar functions are used in a very obvious way to define the segments, e.g., for smooth periodic orbits $h_i$ could define $T_i$ directly. In piecewise smooth systems some terminology has been introduced; $h_i$'s are known as *event* functions, and the zeros of these functions determine event surfaces; $g_i$'s are known as *jump* functions, that act on the end points of segments. Segments are defined in between events, or more precisely they start where the jump map leaves it and ends when it terminates on an event surface, i.e., the first segment is from $\mathbf{x}_0$ to event $h_1$, the second segment is from $\mathbf{x}_1$ to event $h_2$, etc..

For the purposes of bifurcation analysis it is of course still crucial to have a measure of linear stability. In Section 1.4.3 we described the linear stability analysis associated with trajectories in smooth systems and for single-segment orbits; for multi-segment orbits in smooth systems the stability considerations transfer by the group properties of the flow, e.g., observe the evolution of the perturbation in a two-segment decomposition where $T = T_1 + T_2$,

$$v_T = v_2 = X(T_2)v_1 = X(T_2)X(T_1)v_0 = X(T)v_0. \tag{1.57}$$

It is more technical to get the similar result for the evolution of families of perturbations in the non-smooth setting. In Equation (1.42) we introduced the family of perturbations with solutions defined by $\mathbf{x} = \mathbf{x}(t,\epsilon) = \phi(t, \mathbf{x}(0,\epsilon))$; now consider the equation of a family of segments that impact upon the event surface at time $T_j(\epsilon)$ parameterized by the perturbation,

$$\mathbf{x}_0^j(\epsilon) = g_j(\phi_j(T_j(\epsilon), \mathbf{x}_0^{j-1}(\epsilon))), \tag{1.58}$$

where we used $\mathbf{x}_0(\epsilon) = \mathbf{x}(0, \epsilon)$ and superscript $j$ denotes the segment number. The existence of the unique parameterization $T_j(\epsilon)$ can be shown via the implicit function theorem (see [DS13]) under the condition that the orbit intersects the corresponding event surface transversally. In such a case we may obtain the following relation that describe the linear stability of the trajectory in the non-smooth setting[10],

$$v_{j+1} = \frac{\partial g_j}{\partial x} \cdot \left( Id \ - \frac{f \cdot Dh}{Dh \cdot f} \right) \cdot X_j \Big|_{\epsilon=0} \cdot v_j = M_j \cdot v_j, \tag{1.59}$$

where $X_j$ is the linearized flow on the $j$th segment for the orbit $x(t, 0)$ and $v_j = \frac{\partial x_j^0}{\partial \epsilon}\big|_{\epsilon=0}$, i.e., we have obtained the evolution of the family of perturbations over a segment, event surface and jump discontinuity and call define the map as $M_j$. For a periodic orbit the stability is determined by the multipliers of $M$ in the following composition,

$$v_m = M_m \cdot M_{m-1} \cdot \ldots \cdot M_2 \cdot M_1 v_0 = M v_0. \tag{1.60}$$

The trivial multiplier corresponding to the tangent of the periodic orbit is shifted to 0 in this setting.

This short introduction only scratches upon the developed theory for non-smooth dynamical systems. For the encoding of such problems we recommend [DS13]; the current section was mainly inspired by the presentation in that book. The theoretical basis of such dynamical systems is still under development, and readers with further interest may look in, e.g., [BBCK07] for a recent overview.

[10] It takes a bit of work to get to this result and it is not particularly enlightening since we already described the linear stability of trajectories in the smooth setting. However, it is important to realize that $Dh\mathbb{R}^{1\times n}$ is normal to the event surface since it is the gradient of $h$ and the geometric interpretation of the product $Dh \cdot f \neq 0$ is that it is a transversality condition on the trajectories.

## 1.5 The skeleton of a dynamical system

In the previous sections we focussed on the geometric structure of families of solutions as model parameters are varied; special focus was on equilibrium points and periodic orbits. The bifurcation analysis of these two latter provides us with crucial knowledge, e.g., it may be used to make decisions on design considerations in applications, in order to take advantage of nonlinear phenomena or avoid unwanted critical behavior. While this analysis is necessary to get a clear understanding of a dynamical system it also has a soft spot; it is localized to a very small part of phase space, i.e., a small sphere around the fixed point or a tubular neighborhood of the periodic orbits. In many situations we must expand these neighborhoods considerably to explain the significance of certain complicated phenomena.

Bifurcation analysis of equilibrium points and periodic orbits is only part of the understanding of dynamical systems, other orbits are of significant importance to the structure, e.g., homoclinic orbits. As an example consider the unforced vertical pendulum (without damping) and associate it to the natural description with a cylindrical phase space ($\mathbb{R} \times \mathbb{S}^1$) attributed to the angular velocity and the angle; the pendulum has two equilibrium points, the two vertical positions, where one is a saddle and the other is a center. By energy considerations it can be shown that there are two homoclinic orbits/connections for the saddle point, and these two homoclinic orbits corresponds to the exact energy level at which periodic solutions have infinite period and 'collide' with the saddle. In the interior region bounded by the homoclinics the periodic solutions librate around the center, i.e., they are small oscillations that do only librate around the center equilibrium; the region exterior to the homoclinics are periodic solutions that do complete turns of the pendulum. This is perhaps one of the simplest examples for explaining that the organizing centers of dynamical systems may be more special objects than fixed points and periodic orbits; although, admittedly, as we can also conclude in this case, there may be intimate connections between the fixed points/periodic orbits and the special objects (homoclinics).

In the pendulum example everything is quite understandable mainly since the complexity of the bounded asymptotic behavior, for smooth systems in the plane, is restricted to fixed points and periodic orbits; there can not be more complicated types of attractors. Furthermore, in a two-dimensional system orbits are codimension-one manifolds and this means that simple orbits may separate and therefore organize phase space.

While the bifurcation analysis of periodic orbits and fixed points in higher-dimensional dynamical systems is basically unchanged (cf. center manifold or Lyapunov-Schmidt reduction), the organizational importance of special or-

bits decrease significantly. This is basically attributed to the orbits being codimension-$(n-1)$ in $n$-dimensional dynamical systems; the organizing structure/centers of higher-dimensional orbits is then related to the arbitrarily complicated structure of, e.g., stable and unstable manifolds. In [Arn06] V.I. Arnold remarks,

> "Little is known about three-dimenisonal manifolds. For example, it is unknown whether a compact simply-connected three-dimensional manifold is diffeomorphic to the sphere $\mathbb{S}^3$ (the *Poincaré conjecture*[11]) or even homeomorphic to it.
> In large dimensions the differential and topological classifications of manifolds diverge..."

In that perspective caution should be taken with intuitive interpretations in higher-dimensional geometry; in the context of dimension reduction, we may understand it as a warning and an encouragement at the same time.

The organizing geometric structure of a dynamical system is sometimes referred to as the *skeleton*, according to [BKK94] this is made up by all compact invariant manifolds, e.g., fixed points, periodic orbits, tori and homoclinic connections; it may make sense to add the global stable and unstable manifolds of these to this set, e.g., the two-dimensional stable manifold in the Lorenz system [KOD+05]. It is the idea that if the complete skeleton is known then the qualitative behavior of any orbit is known merely from its initial condition (cf. the pendulum and the homoclinic orbits).

One of the main ambitions of the current work is focused towards the approximation of attracting low-dimensional submanifolds in dynamical systems with the purpose of dimension reduction. In some sense, we aim to construct a reduced representation of a relevant dynamical system while respecting the skeleton of the original dynamical system. Formally, let $\mathcal{S}(\lambda)$ denote the skeleton of the dynamical system where the dependence on $\lambda$ represents the parameters of the dynamical system; equivalently let $\mathcal{S}_{\text{red}}(\lambda)$ be the skeleton of the reduced model which is defined on some subset of $U \subset \mathbb{R}^n$. Then the ideal dimension reduction is one where formally

$$\mathcal{S}(\lambda)\Big|_U = \mathcal{S}_{\text{red}}(\lambda). \tag{1.61}$$

In general dynamical systems this equivalence is impossible to show, in fact, it is already in general cases complicated (impossible) to show the equivalence for fixed points which are the simplest constituent of the skeletons. For practical

[11] Meanwhile this has been proven by the russian mathematician Grigori Perelman.

reasons we must therefore aim lower; a reasonable comparison is to compare as much of the qualitative structure that is constructed, and this is also how we test the dimension reduction of the nonlinear mechanical vibrations example in Paper C.

In the following we shall describe some of the basic and relevant results of structural stability in dynamical systems in the very simplest cases; when we then later apply stronger theorems without having accounted for the extra theoretical details of the generalizations it is the ambition that the similarity between the results may pave the way for some deeper understanding. In the end we do this hoping that it may pave the way for a better understanding and appreciation of the crucial differences between the presented approach to dimension reduction that is taken in this work in comparison to other types of reductive methods.

### 1.5.1 Invariant manifolds of fixed points

Consider the following $n$-dimensional linear dynamical system,

$$\begin{pmatrix} \dot{x} \\ \dot{y} \\ \dot{z} \end{pmatrix} = \begin{pmatrix} S & 0 & 0 \\ 0 & U & 0 \\ 0 & 0 & C \end{pmatrix} \begin{pmatrix} x \\ y \\ z \end{pmatrix}, \tag{1.62}$$

where $(x, y, z) \in \mathbb{R}^k \times \mathbb{R}^l \times \mathbb{R}^m$ and $n = k + l + m$. $S \in \mathbb{R}^{k\times k}$, $U \in \mathbb{R}^{l\times l}$, $C \in \mathbb{R}^{m\times m}$. The eigenvalues of $S$ have negative real parts, $U$ have positive real parts and $C$ have zero real parts. In this case we have exponential estimates on the solutions $x(t), y(t)$, i.e.,

$$||x(t, x_0)|| = ||\phi_s(t, x_0)|| = ||e^{tS}x_0|| \leq Ke^{-at}, \quad t \geq 0, \tag{1.63}$$

$$||y(t, y_0)|| = ||\phi_u(t, y_0)|| = ||e^{tU}y_0|| \leq Ke^{bt}, \quad t \leq 0, \tag{1.64}$$

$$\tag{1.65}$$

where $a, b, K > 0$ exist. Before we go on to the nonlinear case, it is worth noting that we do not have this type of exponential estimates on the linear subspace corresponding to the center subspace, i.e., the subspace corresponding to nonhyperbolic eigenvalues has a less rigid structure and we understand that the center subspace(/manifold) of this linear dynamical system is the only part that we really need to analyze. For example, observe that if $S, U, C$ are dependent on model parameters then small parameter perturbations can only have a qualitative effect on the center subspaces.

For nonlinear dynamical systems everything gets technically more difficult, where linear systems have a whole hierarchy of unique invariant one- and two-dimensional

subspaces, much of this structure is lost. Consider a small smooth perturbation of Equation (1.66),

$$\begin{pmatrix} \dot{x} \\ \dot{y} \\ \dot{z} \end{pmatrix} = \begin{pmatrix} S & 0 & 0 \\ 0 & U & 0 \\ 0 & 0 & C \end{pmatrix} \begin{pmatrix} x \\ y \\ z \end{pmatrix} + \epsilon \begin{pmatrix} F(x,y,z) \\ G(x,y,z) \\ H(x,y,z) \end{pmatrix}, \tag{1.66}$$

where $F, G, H$ are smooth functions. While, as we already know, for hyperbolic fixed points the theorem of Hartman-Grobman tells us that the linearized system is locally topologically conjugate to the nonlinear system, the question of topological equivalence is very complicated for nonhyperbolic fixed points and this is the subject of bifurcation theory that we touched upon in Section 1.3 and 1.4. In the nonhyperbolic case, the *center manifold theorem* (see e.g., [Wig03]) gives the existence of a local $m$-dimensional invariant manifold, called the center manifold $W_c(\xi)$, that is tangent to the linear center subspace at the fixed point $\xi$, and solutions that are bounded in a certain neighborhood $U$ of $\xi$ in either forward or reverse time, will asymptotically approach the $W^c(\xi)$. Locally $W^c(\xi)$ is a graph over the center subspace, i.e., it may be represented by smooth functions $x = h^s(z)$ and $y = h^u(z)$. This is perhaps the simplest dimension reduction method that does not ignore the complications of model reduction in nonlinear dynamical systems; in fact the dimension reduction that is used in Paper C is very similar.

While the stable $W^s$ and unstable manifolds $W^u$ are unique the center manifold $W^c$ is non-unique, and this introduces some practical problems in the determination of $h^s$ and $h^u$. Often there will be a continuum of center manifolds, and this may be understood from the classical example due to Anosov in the paper of Kelley [Kel67],

$$\begin{aligned} \dot{x} &= x^2, \\ \dot{y} &= -y. \end{aligned} \tag{1.67}$$

In this example the local center manifold is

$$W^c_\beta(0,0) = \{(x,y) : y = h^s(x,\beta)\}, \tag{1.68}$$

where

$$h^s(x,\beta) = \begin{cases} \beta e^{1/x} & x < 0, \\ 0 & x \geq 0, \end{cases} \tag{1.69}$$

hence there is a family of center manifolds parameterized by $\beta \in \mathbb{R}$. One of the important conclusions from this example is that there is a continuum of center manifolds all of which have the correct qualitative behavior in a neighborhood of the origin. In applications, and in the approach of Paper C, this non-uniqueness is common, there are more strategies to implicitly or explicitly pick one of the center manifolds; for the current example Chicone [Chi06,

p. 340] has a good detailed description on making the center manifold unique by modifying the vector field via particular smoothing functions, often called *bump* or *cut-off* functions. Alternatively, depending on the problem at hand, it may be good enough and therefore practical to take $\beta = \beta^*$, i.e., to pick the center manifold $W^c_{\beta^*}(0,0) = \{(x,y) : y = h^s(x,\beta^*)\}$. The modification of the boundary is necessary via the approach taken in [Chi06], because of a global Lipschitz condition on the vector field; such modifications are often used when proving local results.

Two common methods of proof that rely on fixed point mappings are the Lyapunov-Perron (see e.g. [Chi06, Chap. 4]) method and the graph transformation method (see e.g. [SFLC87, Chap. 5]); while the former is of more analytical flavor via the variation-of-constants integral equations, the latter has an appealing geometric nature.

Using these constructive proofs one may approximate the center manifolds and reduce the dynamical system to the $m$-dimensional dynamical system,

$$\dot{z} = Cz + \epsilon H(h^s(z), h^u(z), z), \tag{1.70}$$

where we used $x = h^s(z)$ and $y = h^u(z)$; we remark that $h^s$ and $h^u$ satisfies the invariance conditions associated to the equations in $x$ and $y$. We did not add parameter dependencies in these equations because they may be assumed to be included in the center subspace since a parameter $\lambda$ can be added by $\dot{\lambda} = 0$.

It should be noted that it is not necessary for the eigenspectrum of $C$ to have real part zero, the criterion is more general, the real parts of the eigenspectrum corresponding to both $S$ and $U$ must be larger in absolute value than any real part in the $C$; this condition is similar to the condition of normal hyperbolicity in Paper C. In fact it is particularly important to note that this gap in the eigenspectrum between the center space and the unstable/stable spaces is crucial to the type of dimension reduction that we apply, this gap is the so-called *spectral gap*. We will apply generalizations of the center manifold theorem for more complicated sets in Paper C, but the idea is very much the same; e.g. the breakdown of a generalized spectral gap (generalized Lyapunov-type numbers) for the so-called normally hyperbolic invariant manifold, implies a bifurcation of the normally hyperbolic invariant manifold.

Chapter 2

# Modelling and analysis of a forced impacting beam — theory and comparison with an experiment.

This chapter is concerned with the mathematical modelling and analysis of a vibro-impacting beam experiment [BSS+13]. The experiment is part of a collaborative research project at the Technical University of Denmark (DTU) between the Department of Applied Mathematics and Computer Science (formerly Department of Mathematics) and the Department of Mechanical Engineering. The project is focused on control-based continuation in experiments [SK08][SGBN+08][BSS+13]. Control-based continuation is a method that allows the continuation of families of special solutions in experiments; it is the experimental equivalent to numerical continuation and bifurcation analysis in dynamical systems. The experimental continuation is applied to branches of stable and unstable periodic solutions. The experimental setup is shown in Figure 2.1.

Figure 2.1: The vibro-impacting beam experiment. The vibrating beam is the steel ruler which is clamped and mounted on the base structure in the middle. The mechanical stops are approximately at the half length. The lumped mass point is surrounded by the magnetic controllers which are used for the control-based continuation. The displacement of the base structure is measured by the top laser and the displacement of the beam by the bottom laser. The shaker is the black box on the left. See [BSS+13] for more details. Photo [Bur].

The contribution of the thesis to the project was focused on the development of a low-dimensional model (one degree of freedom). The objective behind the modelling project was to increase the understanding of the mechanical system and to create a basis for doing preliminary testing of ideas on a computer rather than in the lab.

As the model was shown to perform well a secondary study was initialized with the additional inclusion of Viktor Avrutin; the objective of this study was an exploration of phase and parameter space in a quest to find special solution branches disconnected from the 1:1 resonance component.

The current chapter is structured as follows: in Section 2.1 we introduce Paper A which amongst other topics is concerned with the derivation of the vibro-impact model of the experimental setup and some analysis of the 1:1 nonlinear resonance tongue; in Section 2.2 the analysis of the model is expanded to a larger parameter regime where we show the existence of isolas of subharmonic orbits; in Section 2.3 we give an account of how certain decisions were and can be substantiated in the mathematical modelling process. In addition, future directions on the modelling task are discussed.

We remark that the current chapter and Paper A deals with most of the theory that was described in Chapter 1.

## 2.1 Introduction to Paper A

Paper A may be decomposed into four smaller parts:

1. Derivation of a minimalistic mathematical model of the experimental setup
2. Smoothing of the non-smooth dynamical system
3. Bifurcation analysis of the smoothing and the forcing amplitude/frequency
4. Comparison with experimental data adapted from [BSS+13]

The mathematical modelling and analysis of vibro-impacting systems is far from complete, there is not 'one model to rule them all', many choices are non-unique and models with good predictive quality may be very different. Inspired by [MS83][Sha85] we derive the low-dimensional model description via Galerkin's principle, with a twist though since we only formally use the principle to get the structure of the dynamical system and some useful information to estimate

system parameters. Note that from a continuum physics point of view the governing equation of this system is a nonlinear PDE. In fact, we assume it to be described by a piecewise defined PDE.

While the derivation was most naturally done in the framework of a piecewise defined description, the impacts of the beam with the mechanical stops are not hard impacts (infinite stiffness) because the beam is rather flexible when impacting upon the mechanical stops. For this reason we construct a smooth description by smoothing the piecewise defined dynamical system using a smooth one-parameter switching function. The bifurcation structure showed an interesting dependence on the smoothing parameter and this was analyzed in depth such as to make sure that the smoothing did not have an unwanted effect. Rather than viewing the smoothing procedure as a means to approximate a non-smooth system it should be viewed as an alternative description of an impact process.

In the remaining parts of the paper we perform numerical bifurcation analysis in one and two parameters. The results are compared with an experimental data set from [BSS+13].

Now we refer the reader to Paper A in the Appendix.

## 2.2 Model-Exploration: Isolas and their experimental verification

In a subsequent study the solution structure of the derived impact model (Paper A) was further investigated in a search for special solutions primarily in parameter regimes away from the 1:1 resonance. This study was initialized in collaboration with Viktor Avrutin, where phase space was scanned for special solutions in specified parameter regions. In this systematic scan of phase and parameter space, we considered parameter variations of the forcing amplitude $I$ and the forcing frequency $\Omega$; we consider the same two parameters as in Paper A as a consequence of the experimental setup, i.e., these two parameters are the free parameters for practical investigations in the experimental setup. The theory provided in Section 1.4.4 is relevant in order to understand certain details in the current section. We shall present the study in three subsections; in Section 2.2.1 we present some of the results of the scans of parameter and phase space; in Section 2.2.2 we present some results of the numerical bifurcation analysis of the periodic orbits in the piecewise smooth setting; in Section 2.2.3 the results are compared to experimental measurements.

### 2.2.1 Scans of parameter and phase space

In the previous discussions we have seen the occurrence of multiple solutions co-existing, e.g., for the 1:1 nonlinear resonance tongue in Paper A we observed two stable periodic orbits and one unstable periodic orbit in a parameter region of forcing frequency and forcing amplitude; this type of multi-stability emerging from fold points is amongst the simplest and this type of nonlinear resonance tongue is well-known in this type of dynamical system. From a technical point of view they are often easy to find because they are on the same connected component as the small amplitude linear solutions. Since continuation methods are based on path-following we can only trace out the connected component that we initialize our continuation analysis on. The components of the bifurcation diagram that we shall construct next are disconnected from the branch of trivial small amplitude solutions, but first we describe how the orbits were found.

When we search for periodic solutions that are disconnected from the trivial small amplitude periodic solutions in phase space one strategy is forward integration of initial conditions. Disregard the parameter variation for a moment and consider the task of scanning for periodic solutions in a general dynamical system,

$$\dot{x} = f(x), \quad f : \mathbb{R}^n \to \mathbb{R}^n. \tag{2.1}$$

The complexity of a scan for periodic solutions grows in a computationally very unattractive way with the phase space dimension, e.g., if we scan an $n$-cube $\subset \mathbb{R}^n$ which is composed of $m$ points in each dimension then we must integrate $m^n$ initial conditions, therefore it is implied that such scans are only realistic in systems where it makes sense to scan very few dimensions.

In the present case the dynamical system is defined as follows,

$$\begin{aligned} \dot{x} &= f(x), \\ \dot{\theta} &= 1, \end{aligned} \tag{2.2}$$

where $(x, \theta) \in \mathbb{R}^2 \times \mathbb{S}^1$ and the introduction of the phase variable $\theta$ made the system autonomous, in fact, the periodic forcing immediately implies that the search for periodic orbits $x(t) = x(t + kT)$ where $k$ is an integer and $T = 2\pi/\Omega$ is reduced to scanning in $x \in \mathbb{R}^2$ and checking the periodicity condition. This is because the periodic forcing defines a trivial global transversal[1] to the flow which can be used as a global Poincaré section. The scans may then be repeated for various parameter sets. The parameter scans were performed using AnT [ALS+03].

[1] This is a codimension-one manifold which any trajectory intersects transversally.

At low forcing frequencies and forcing amplitudes ($I < 0.25$), i.e., in the neighborhood of the 1:1 nonlinear resonance tongue, parameter scans were performed and these indicated no special solutions except for the ones associated with the tongue (cf. Paper A, Figure 13).

While planning the scans there was an implicit constraint, namely, that we were limited to the low end of forcing amplitudes and forcing frequencies because of limitations due to the shaker in the actual experiment. In this context it should perhaps be noted that the shaker force $F_{\text{shaker}}$ is proportional to the forcing amplitude $I$ and the square of the forcing frequency $\Omega$, i.e., $F_{\text{shaker}} \propto I\Omega^2$.

The next region to scan, away from the 1:1 resonance, are for frequencies larger than three times the fundamental frequency of the beam; note that this is already a much more demanding task for the shaker. In Figures 2.2a-2.2c some scans are shown for a range of $\Omega \in [3, 5]$ and $I = 0.08$, $I = 0.09$ and $I = 0.10$; the scans show what looks like isolas of special solutions and branch points. Note how the apparent limit set structure changes quite radically over a reasonably small change in forcing amplitude, this sensitivity and the overall occurrence of several branches indicate a rich and complicated structure.

We remark that the harmonically forced impact oscillator with symmetric mechanical stops, may be expected to share much qualitative behavior with the standard Duffing equation because they share the same overall structure; the damping is identical, stiffness is similar (same symmetry) and they are harmonically excited. These relations make it reasonable to hypothesize the existence of subharmonic solutions. In particular it may be expected that it is possible to find 1:3-subharmonic orbits, see e.g., [NM95, chap.4] for some practical perturbation calculations for subharmonics in systems with cubic nonlinearities.

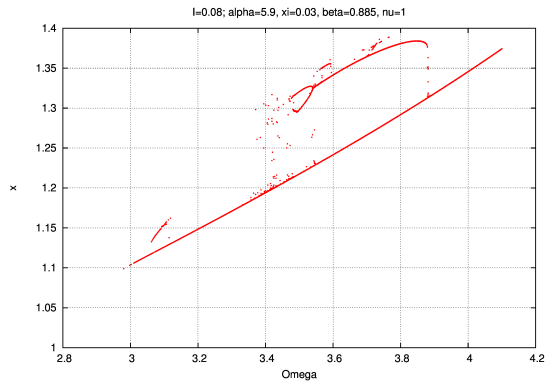


(a)

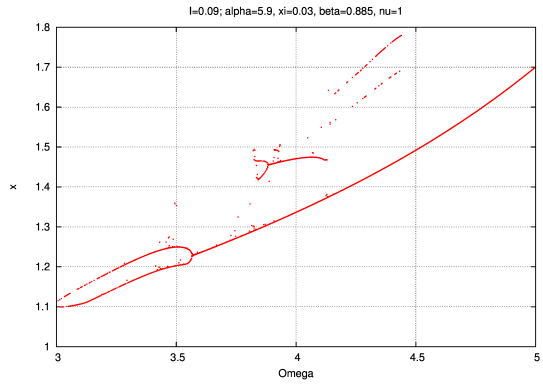


(b)

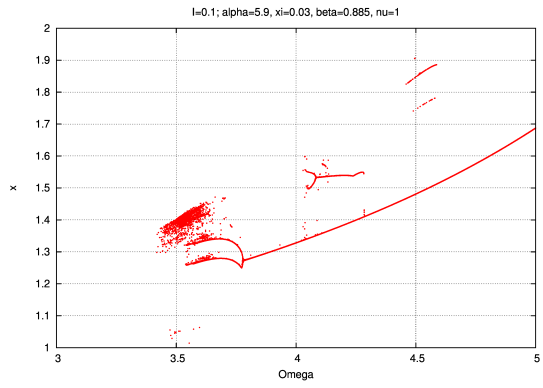


(c)

Figure 2.2: Scans for periodic orbits of the impact oscillator ($\alpha = 5.9$, $\xi = 0.03$, $\beta = 0.885$ and $\nu = 1$ cf. Paper A): Panel (a) scans with forcing amplitude $I = 0.08$, Panel (b) forcing amplitude $I = 0.09$ and Panel (c) forcing amplitude $I = 0.10$. [AE]

### 2.2.2 Preliminary numerical bifurcation analysis of two isolas of subharmonic orbits

Subsequently, bifurcation analysis was initialized, this time the bifurcation analysis was performed on the non-smooth dynamical system using the CoCo software package [DS] and the *hspo*[2] toolbox. In Section 1.4.4 we described the formulation of multisegment orbits, such as those that we encounter in non-smooth systems; a further discussion of the details and differences that emerge as the regularity of a dynamical system decreases can be very complicated because the traditional bifurcation analysis relies on smoothness of the solution sets.

In addition to Section 1.4.4 we shortly introduce the concept of orbit signatures by example of the signature of the 1:1 orbit. In Figure 2.3 we see the explicit

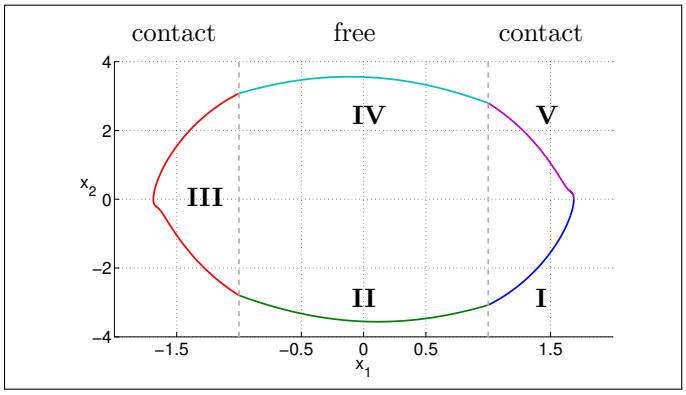


Figure 2.3: Multisegmentation of a 1:1 periodic orbit; the orbit is split into five segments, each segment is defined by *Mode, Event, Reset*. The thick dashed gray lines indicate the mechanical stops. The model parameters are $\xi = 0.03$, $\beta = 0.9$, $\alpha = 5.9$, $I = 0.1$, $\nu = 1$ and $\Omega = 5$.

orbit segmentation; the *Mode* of a segment is determined by the condition that $|x_1| > 1$ is in the 'contact' mode and $|x_1| < 1$ is in the 'free' mode; furthermore the thick dashed grey vertical lines indicate the mechanical stops. In Table 2.1 the signature of the orbit is given; each segment has a signature that defines it, the $h$ scalar functions from Equation (1.56) are defined by the 'Event' and the $g$ functions are defined by the 'Reset'. As an example segment **I** has the following interpretation; 'contact' implies that the orbit must satisfy the piecewise defined dynamical system for $|x_1| > 1$, when the segment intersects the 'right' mechanical stop the segment terminates and the 'impact' reset is particularly

[2] *hspo* is an abbreviation for Hybrid System Periodic Orbit.

| Segment | **I** | **II** | **III** | **IV** | **V** |
|---|---|---|---|---|---|
| Mode | contact | free | contact | free | contact |
| Event | right | left | left | right | vzero |
| Reset | impact | impact | impact | impact | phase |

Table 2.1: Signature for the periodic orbit shown in Figure 2.3.

simple in the current case because it is the identity. Each segment starts where the previous segment terminates after its reset, hence segment **V** starts at the right mechanical stop and terminates when the velocity is zero and then the phase variable is reset to zero. Note that the signature for orbits is non-unique. For details on the encoding of such problems consult, e.g., [DS13].

As we remarked in the previous section the scans that were performed with AnT indicated a very rich bifurcation structure; in such cases numerical continuation and bifurcation analysis is by far the best tool to investigate, understand and map the qualitative and quantitative behavior of the dynamical system. In Figure 2.4 we have computed a bifurcation diagram for $I = 0.08$ (cf. Figure 2.2(a)); the big isola ($3 < \Omega < 7$) consists of 1:3 subharmonic orbits[3] and for this forcing amplitude it does not contain any branch points; in the lower frequency range, $3 < \Omega < 4$, we see the occurrence of a smaller isola and this consists of many different subharmonic orbits. In Figure 2.4(b) we focus on this smaller isola which shows branch points and period-doubling bifurcations; the largest component of the small isola consists of 3:9 subharmonic orbits and then a period-doubling cascade seems to start at $\Omega \approx 3.5$, period-doubling points are detected at $\Omega = \{3.4920, 3.4849, 3.4835\}$, however these are not shown in the current figures. We remark that the period-doubling bifurcations are supercritical so at these points a branch of unstable periodic orbits continue such that we expect many co-existing unstable orbits for e.g. $\Omega = 3.25$.[4] Note that branch points are not a generic phenomenon in dynamical systems, in the present system they occur as a consequence of the symmetry, perturbations that do not preserve the symmetry will destroy the branch points.

[3]The identification of periodic orbits by the notation $m$:$n$ in our case is not entirely unique and deserves a short explanation. It is used to denote an orbit that is periodic with $n$-times the period of the forcing and it makes $m$ oscillations.

[4]It may be interesting to remark that the three period-doubling points $\Omega = \{3.4920, 3.4849, 3.4835\}$ give $(\Omega_{\mathrm{pd1}} - \Omega_{\mathrm{pd2}})/(\Omega_{\mathrm{pd2}} - \Omega_{\mathrm{pd3}}) = 5.0714$, and there is a universal number called Feigenbaum's constant $c_{\mathrm{Feig}} = 4.669\ldots$ that the ratio of the period-doubling bifurcations might approach, i.e., $(\Omega_{\mathrm{pd}i-1} - \Omega_{\mathrm{pd}i})/(\Omega_{\mathrm{pd}i} - \Omega_{\mathrm{pd}i+1}) \to c_{\mathrm{Feig}}$ for $i \to \infty$.

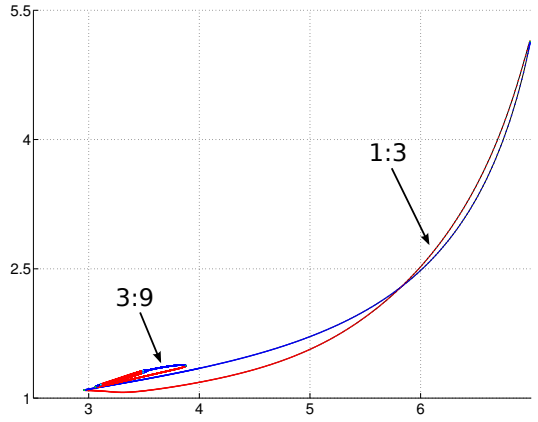


(a)

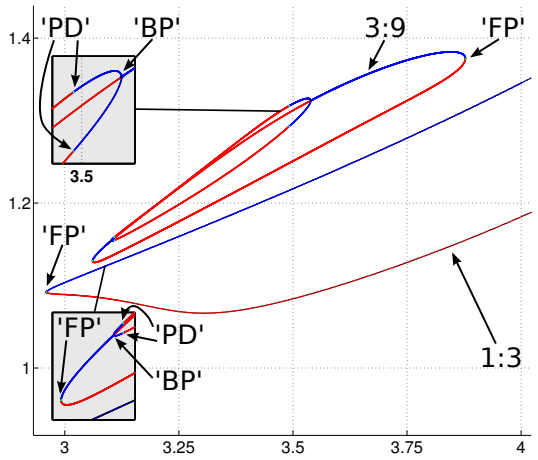


(b)

Figure 2.4: Numerical continuation results for subharmonic orbits at $\Omega \geq 3$: Panel (a) shows the numerical bifurcation results obtained using CoCo; blue denotes stable, red unstable, 'PD' period-doubling bifurcation, 'BP' branch point, 'FP' fold point. The branch type is identified by $m$:$n$. Panel (b) is a zoom. The bifurcation diagram is constructed using $\xi = 0.03$, $\beta = 0.9$, $\alpha = 5.9$, $I = 0.08$ and $\nu = 1$.

A more practical numerical remark concerned with the continuation of a period-doubling cascade such as the one in Figure 2.4 is to realize that if the error tolerance over the segments is to be kept constant then since the length of the period-doubled orbit basically doubles this implies that the number of collocation points should also be doubled, i.e., the number of nonlinear equations to be solved via Newtons method has growth proportional to $2^k$ for the $k$th period doubling in the cascade. Furthermore, since for every supercritical period-doubling bifurcation a branch of unstable periodic orbits continues to the 'other' side, cf. Figure 2.4(b) $\Omega \in [3.10, 3.53]$, these branches of periodic orbits lie very close to each other and it becomes more difficult to stay on a branch of $(2^k T)$-orbits since the signature fits all $(2^j T)$-orbits with $j \leq k$.

### 2.2.3 Experimental verification and comparison of results

Based on the numerical evidence of a wide range of subharmonic orbits at three times the fundamental frequency of the beam model, we took the numerical results to the lab to verify that the subharmonics also existed in the physical experiment. In the experimental setup it is possible to mechanically shake the system with perturbations of a certain amplitude, which was not sufficient. We remark that brute-force numerical scans seemed to indicate that the basin of attraction for the subharmonic orbits is very small, meaning that even if a perturbation is large enough it was very likely to end up on the trivial stable low-amplitude 'linear' solution branch; the basin of attraction in the physical experiment shared this property but after some nudges with the hand the experiment relaxed to a stable branch of 1:3 subharmonic orbits. Basic experimental sweeps were conducted and a disconnected component was discovered. Subsequently, attempts where made to perform continuation of the branches of subharmonic orbits and while the control-based continuation in the experiment had been performed successfully repeatedly at the nonlinear 1:1 resonance tongue the isola of subharmonic orbits presented new challenges. Based on the numerical investigations this is to be expected because of the rich bifurcation structure; not only are branches of periodic solutions apparently close to each other, but analysis indicates that there should be regions with many unstable subharmonic orbits which the control-based continuation may detect.

The first report on the occurrence of the isola is presented in Paper B. The results of the control-based continuation are shown in Figure 2.5(a) and compared to the results of the mathematical model. We remark that the comparisons between the mathematical model and the experimental results is only qualitative; the shaker does not provide a perfect harmonic because it is weakly coupled to the beam, and the amplitude of the forcing is not completely independent of the forcing frequency.

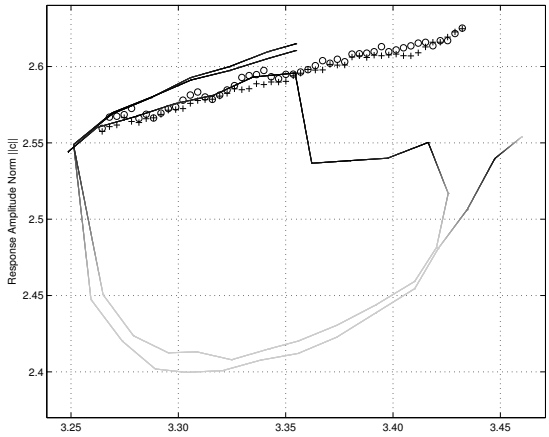


(a)

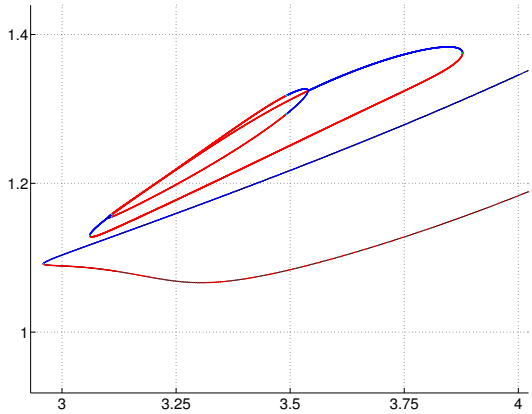


(b)

Figure 2.5: Experimental and numerical continuation results for subharmonic orbits at $\Omega \geq 3$: Panel (a) shows the branches of subharmonic orbits found by a parameter sweep and then two consecutive runs of control-based continuation using different settings for both tolerances and step size; the + symbolize sweep up and ∘ sweep down; the stability information of the continuation runs is an interpolated measure, dark means stable and light means unstable. Panel (b) is for structural comparison, it is identical to Figure 2.4(b) without zoom boxes. The bifurcation diagram is constructed using $\xi = 0.03$, $\beta = 0.9$, $\alpha = 5.9$, $I = 0.08$ and $\nu = 1$.

The subharmonic orbits are predicted at the similar frequency range and the experimental results of the control-based continuation does indicate the existence of multiple branches.

At least two things are crucial to note in Figure 2.5(a); firstly, at $26,8$Hz the control-based continuation in the experiment terminates with an end-point event 'EP', one explanation given in Paper B is that the branch terminates because a shift in phase causes it to lose contact with the mechanical stop, another explanation might be that the step size of the continuation run is to big to detect the fold of an isola as that shown around $\Omega \approx 3.9$ in Figure 2.5(b).

Another observation is what looks like a branch switch around 26 Hz in Figure 2.5(a), the step size of the control-based continuation run is seemingly large compared to the characteristic distance between branches and the radius of curvature. This structure could be associated with the multiple branches that are also observed in the numerical bifurcation analysis in Figure 2.5(b).

We remark that even if the different branches are not 1:3 subharmonic orbits in the mathematical model, an explanation could be that other subharmonics are within the tolerances that define a 1:3 subharmonic in the experiment, e.g., in an experiment it may be challenging to differentiate between 1:3 and 3:9 subharmonic orbits, unless the difference between the measured signals in an $L_2$ sense is sufficiently big relative to noise levels. (In the practical experiment such a convergence check would amount to a squared difference between a small number of Fourier coefficients). It is important to note that this is not a problem of the control-based continuation methodology; it is only a property of the experiment that the method is applied to. In the present case the control-based continuation traces out much more structure than could ever be expected from naïve brute-force scans in a lab.

We shall not go into the details of Paper B but only remark that it is concerned with the problem of determining (quantifying) stability in the experiment and the methods developed in the paper are based on the idea of finite-time Lyapunov exponents and these exponents are intimately related to the idea of the linear stability presented in Section 1.4.3. Remember that the linear stability of a periodic orbit is central to the determination of bifurcation types in a bifurcation analysis.

As a last remark it is important to acknowledge that while the model seems to perform well at small amplitudes it is far from perfect and we shall not be overly confident in the quality of the model, because it simply predicts 1:3 subharmonic orbits, many ODEs of this type would do so. However, the mathematical model has at least proven useful for the experimental work. In the following section we shall discuss how to proceed.

## 2.3 Discussions and future directions

During the project on the vibro-impacting beam, some small substructure [BSS+13, Figure 14] was observed on the nonlinear 1:1 resonance tongue in the experiment and this was not reproduced by the model. We started speculating about what these could be, and what type of meaningful model extensions would potentially explain this additional substructure. As a starting point it is natural to assume that the derived model is an essential building block for any low-dimensional model, i.e., while it does not predict the small additional substructure in the investigated parameter regimes it performs quite well overall for small amplitude orbits, e.g., in predicting the nonlinear resonance tongue and the subharmonic isolas. Without screening for good and bad ideas for possible explanations we list three examples, that are evaluated in the following.

1. Break the symmetry of the gap, i.e., the beam is off-centered between the two mechanical stops
2. add a second axial mode, i.e., add the mode shape corresponding to the second eigenfrequency
3. add a torsional mode to adjust for skew impacts, i.e., the case where the beam impact line is not constant

1) The first point on the list is seemingly the easiest to dismiss; in the parameter regimes of the 1:1 nonlinear resonance tongue the continuation and bifurcation analysis did not detect any branching points that could be induced by the symmetry of the derived impact oscillator, in particular the nonlinear resonance tongue shown in Paper A is structurally stable to perturbations; hence the bifurcation diagram would be robust with respect to an infinitesimal off-centering of the beam. We remark that in the piecewise-linear system a break of the symmetry changes the grazing bifurcations; in the symmetric case the periodic orbit grazes both mechanical stops at the grazing point bifurcation, in the symmetry-broken case the periodic orbit grazes the closest one at the first grazing point bifurcation. If there would be any difference between the smooth representation and the non-smooth representation it should be insignificant from a practical point of view.

Specifically, one may explain the expectation in a more practical manner. In the non-smooth model description the stiffness of the beam changes in a piecewise-linear manner, and the forcing changes discontinuously if $\nu \neq 0$. Under the assumption that the experiment is well described using the laws of physics of continuous matter, then it is a very troubling idea that some forces must be

modelled as non-smooth, e.g., force terms that change direction or strength instantly.

In summary; the bifurcation structure of the nonlinear resonance tongue in Paper A is stable in the smooth description with respect to perturbations, since fold points and hyperbolic periodic orbits persist under small perturbations, it follows immediately that breaking the symmetry of the gap in the considered parameter regimes may be dismissed without further testing.

2) The addition of extra degrees of freedom from other bending modes, i.e., specifically the mode shape corresponding to the second eigenfrequency in the transverse vibrations and the first torsional mode are evaluated. The strategy is to estimate the characteristic time scales and amplitudes of these extra modes in order to assess how likely they are to explain the effects. The word 'likely' is used to express that this type of analysis is heuristic, because it is based dimensional analysis and scaling.

The periodic orbits at the 1:1 resonance undergo two impacts per cycle, this implies that the characteristic time between impacts $T_{\text{impact}}$ is half the period $T$,

$$T_{\text{impact}} = \frac{1}{2}T = \frac{\pi}{\Omega}, \tag{2.3}$$

where $\Omega$ is the frequency of the forcing.

In order to come up with estimates from linear analysis or even simple scalings from dimensional analysis, it is an advantage to be able to formulate the problems mathematically. The formulation for the free vibrations of a cantilever beam with a concentrated mass at the end point and formally it writes as the follows,

$$EI\frac{\partial^4 u}{\partial z^4} + \rho A\frac{\partial^2 u}{\partial t^2} + \delta(z-L)m_d\frac{\partial^2 u}{\partial t^2} = 0, \tag{2.4}$$

$$u(0) = \frac{\partial u}{\partial z}(0) = \frac{\partial^2 u}{\partial z^2}(L) = \frac{\partial^3 u}{\partial z^3}(L) = 0, \tag{2.5}$$

where $m_d$ is the concentrated mass at the end point[5]. The word 'formally' is used to express that the equation, strictly speaking, does not make much mathematical sense with the Dirac delta distribution in a strong form. In order to solve such a system we may apply Galerkin's method, which under certain conditions converge to the weak solution of the problem, e.g., choice of function space. Currently we are interested in the eigenfrequencies of the free vibrations in the system, and these may be determined by standard calculations (see e.g.

[5]Note that we use $L$ as the distance to the mass point for simplicity.

[Mei01, Chap. 8]). The eigenfrequencies of the system can be determined from the following equation from [Mei01],

$$-\cos\gamma - \cosh\gamma - \frac{\sin\gamma + \sinh\gamma}{\cos\gamma + \cosh\gamma}(\sin\gamma - \sinh\gamma) \tag{2.6}$$
$$+ \frac{m_d}{\rho_b L}\gamma\left(\sin\gamma - \sinh\gamma - \frac{\sin\gamma + \sinh\gamma}{\cos\gamma + \cosh\gamma}(\cos\gamma - \cosh\gamma)\right) = 0,$$

where $\gamma^4 = \omega^2\rho_b L^4/EI$; $\rho_b$ is the mass density of the beam per unit length. Numerically, we find the two first eigenfrequencies $\gamma_1 = 0.77$ and $\gamma_2 = 3.94$, and from this we may calculate the eigenfrequencies

$$f_i = 2\pi\omega_i = 2\pi\sqrt{\frac{EI\gamma_i^4}{\rho_b L^4}}. \tag{2.7}$$

For the current discussion we need only evaluate the ratio between the first and second eigenfrequency,

$$\frac{f_2}{f_1} = \left(\frac{\gamma_2}{\gamma_1}\right)^2 \approx 26, \tag{2.8}$$

and thus the second eigenmode oscillates roughly 26 times for every period $T_1 = 1/f_1$, it would be an unusual explanation to go for the idea of a resonance between such two modes. Another interesting observation in this context is to consider the characteristic damping time of the second eigenmode in comparison to the time between impacts; we can do this under the assumption that the mechanical system is well characterized by a linear modal damping model. In that case all perturbations of the $n$th eigenmode are modulated by $\exp(-\xi\omega_n t)$. Now, since the beam is both in the free and the contact mode we assume that it is half of the time in each. Furthermore, we assume that the second eigenfrequency increase with the same ratio as the first eigenfrequency calculated in Paper A, i.e., $\omega_{2,c} = (1+\alpha)\omega_2$ and the damping changes as $\xi_c = (1+\beta)\xi$. In particular this implies,

$$C = \exp\left(-\xi_c\omega_{2,c}\frac{T_{\text{impact}}}{2}\right)\cdot\exp\left(-\xi\omega_2\frac{T_{\text{impact}}}{2}\right) \approx 0.65, \tag{2.9}$$

which means that the already small response amplitude $A_2$ of the second eigenmode is reduced to $A_2(t + T_{\text{impact}}) = CA_2(t)$ before it impacts again. Note that the energy from the impact is not focused to the second mode, it is a broad spectrum of higher frequencies that are excited and therefore we expect a very low excitation amplitude of the second mode at the impact time. Arguments based on the properties of damping in a model may be rightfully critized because damping is phenomenological and there are many models [Adh00] to choose from; so essentially it is a modelling decision. An interesting remark is found in Bolotin [Bol64, ch. 15, § 61] in a short paragraph on damping, in particular, about linear modal damping; we quote

> "The supposition about the diagonal form of matrix $\varepsilon$ [damping matrix] is equivalent to the assumption that there is no transfer of energy between principal forms of vibrations by the resistance forces. Experiments performed on a sufficiently wide class of systems show that this assumption is plausible ... Even if matrix $\varepsilon$ is not diagonal, then it can be easily shown that the influence of the elements outside of the principal diagonal, on the damping of free vibrations is very small."

Principal forms refer to modal forms and the $\varepsilon$ is the damping matrix. Furthermore, in impacting systems it is even less transparent how to apply damping, in some cases modellers enforce restitution laws to model the inelastic effects associated with mechanical impacts. In [BBCK07, Chap. 9] the high-frequency noise from impact oscillators is discussed together with some of the difficulties connected to this. We dismiss the idea that it could be a second eigenmode.

3) We consider now if the addition of a torsional mode, supposedly excited by small out-of-plane bending of the beam, can explain the resonance. The PDE governing small torsional vibrations with a mass at the end point is the wave equation [LL86]

$$\rho I \frac{\partial^2 \theta}{\partial t^2} - C_b \frac{\partial^2 \theta}{\partial z^2} = 0, \tag{2.10}$$

$$\rho I = m_d I_d \delta(x - L) + \rho_b I_b, \tag{2.11}$$

where $\theta$ is the relative angular change between cross sections along the centroid of the beam, $\theta$ is the torsion angle, $C_b$ torsional rigidity of the beam and $\rho_b$ beam density per unit length, $I_b$ is the polar moment of inertia[6], $m_d$ is the lumped mass and $I_d$ is the polar moment of inertia of the lumped mass.

The analysis of the torsional mode can be simplified quite a lot by a few reasonable assumptions,

$$\frac{\partial \theta}{\partial z} L \ll 1, \tag{2.12}$$

$$\theta \propto z, \tag{2.13}$$

and the beam length $L$ is further assumed constant. Essentially, this setup means that we only pay the price for the strain connected with rotating rigid

[6]The polar moment of inertia is $I_b = \int (x^2 + y^2)\, \mathrm{d}A$ where $A$ is the cross section of the beam. Note that $C_b$ is not always possible to look up, it depends very much on the geometry of the beam. Landau [LL86] has a particularly good discussion of the fundamentals of torsion in rods.

cross sections very little relative to each other. One can show that the potential energy $U$ of this deformation is given as,

$$U = \int_0^L \frac{1}{2} C_b \left( \frac{\partial \theta}{\partial z} \right)^2 \, \mathrm{d}z, \tag{2.14}$$

and the kinetic energy of the beam $T_b$,

$$T_b = \int_0^L \frac{1}{2} \rho_b I_b \left( \frac{\partial \theta}{\partial t} \right)^2 \, \mathrm{d}z, \tag{2.15}$$

and the kinetic energy of the mass considered as a disc $T_d$,

$$T_d = \frac{1}{2} m_d I_d \left( \frac{\partial \theta}{\partial t} \right)^2_{z=L}, \tag{2.16}$$

where $I_d$ is the polar moment of inertia of the lumped mass $m_d$. The fundamental frequency of the torsional mode can then be found by letting[7]

$$\theta(z,t) = A \cos(\omega t + \phi) z/L, \tag{2.17}$$

such that an energy balance[8] of kinetic and potential energy (Rayleigh-Ritz method [CH53]) may be used to obtain,

$$\omega^2_{\text{torsion}} = \frac{\int_0^L C_b \, \mathrm{d}z}{\int_0^L \rho_b I_b (z/L)^2 \, \mathrm{d}z + m_d I_d L^2} = \frac{C_b/L}{\rho_b L I_b/3 + m_d I_d} = \frac{C_b/L}{m_b I_b/3 + m_d I_d}. \tag{2.18}$$

The torsional rigidity is non-trivial to obtain for general bodies and even for beams it may be looked up in tables for different cross sections. For beams with rectangular cross section where the width $d$ is much smaller than thickness $h$, one can obtain

$$C_b = \frac{1}{3} \mu d h^3, \qquad h \ll d, \tag{2.19}$$

$$I_b = 1/12 \cdot (d^3 h + d h^3), \tag{2.20}$$

$$I_d = 1/12 \cdot (d_m^3 h_m + d_m h_m^3), \tag{2.21}$$

where $\mu$ is the Lamé second parameter, also known as the shear modulus or modulus of rigidity. Combining Equations (2.19) and (2.18) and $\mu = 77.2 \cdot 10^9$ Pa, $d = 2.5 \cdot 10^{-2}$ m, $h = 0.1 \cdot 10^{-2}$ m, $d_m = 2.9 \cdot 10^{-2}$ m, $h_m = 3.5 \cdot 10^{-2}$ m,

[7] this is not the exact solution to the problem, but it is a good guess. (An exact solution can be constructed if necessary, but there is no reason to do so).

[8] Energy balance and Rayleigh-Ritz method are great methods, but note that the approximation follows immediately from an application of Galerkin's principle, and in such a case we can easily handle lumped masses etc. without thinking too hard about the energy.

$m_d = 0.2116\text{kg}$, $\rho_b = 8 \cdot 10^3 \frac{\text{kg}}{\text{m}^3}$ and $L = 0.1275\,\text{m}$ the fundamental frequency[9] of the torsional vibrations is,

$$f_{\text{torsion}} = 2\pi\omega_{\text{torsion}}. \tag{2.22}$$

In comparison to the fundamental frequency of the vibrations of the beam we have,

$$\frac{f_{\text{torsion}}}{f_1} \approx 222, \tag{2.23}$$

hence if the torsional damping is also approximated by linear modal damping torsional effects are rendered insignificant.

Another explanation which was not given in the list is the reason we shortly mentioned in the previous section, namely, that the shaker in the experiment is coupled to the dynamics of the beam. This means that the shaker should be added as an extra degree of freedom in the model. In [BSS+13] and Paper B the observed system is not only the beam dynamics but rather the system composed of the beam structure as well as the shaker. Since the small resonance bubble is observed for impacting orbits with small amplitudes, it is probably not a bad guess that the delay in the shaker control is approximately the same as the length of the time-interval that the corresponding orbits spend from the time of initial contact to the time at which the velocity changes direction. This was not tested. As opposed to other additions the dynamics of the shaker is a bit more difficult to add because the shaker does not come from the supplier with the type of detailed information which is necessary for modelling the shaker as an active degree of freedom. One possibility is to deduce a model of the shaker and perform parameter fitting by using the experimental data. On another note, yet another addition to the model could be the inclusion of a cubic nonlinearity in the contact mode in case the response amplitudes of the beam get large enough for this to be relevant.

With these comments on the minimalistic modelling of the vibro-impacting beam with symmetric mechanical stops we will now turn to another type of reduction; while this part of the thesis was focused on reduced models of a mechanical experiment. Chapter 3 is focused on the reduction of a reference high-dimensional dynamical systems to a low-dimensional dynamical system. In the end of Paper C, we present an example (from [JPS05]) where a 25 dimensional dynamical system is reduced to a 3-dimensional dynamical system, while, so far as analysis shows, accurately preserving the skeleton and the quantitative measures of the reference dynamical system.

[9] Note that we use $L$ as the distance to the mass point for simplicity.

Chapter 3

# Dimension reduction of dissipative dynamical systems

*Reductionism* is concerned with the idea that the meaning of the 'whole' is to be understood via its smaller parts and their interrelations. While some claim that this idea is essential to our understanding of life in general, others refuse this idea; we shall not take part in such a debate but merely state the fact that the *scientific method* is very useful. One of the basic ideas of the scientific method is that in order to understand complex problems they should be broken into smaller problems of which there is a deeper understanding of *cause* and *effect*. Applied mathematicians and physicists approach problems very naively and try to formulate them in mathematical models; as to the validity of the models, in a real-world context, the ambition is often modest; the quote attributed to George E.P. Box [BD07] expresses this quite well

> Essentially, all models are wrong, but some are useful.

Mathematical modeling has already proofed extremely useful in many fields, e.g., fluid dynamics, structural dynamics, electrodynamics, quantum mechanics and many more.

While a recurring property of dynamical systems suitable for dimension reduction is the emergence of pattern and structure; the language of mathematics is

suitable to describe precise details, the validity of approximations in modelling is often restricted to convergence results in the limit where the finite-dimensional approximations go to infinity because they must approximate an element of an infinite-dimensional function space. For linear systems it is sometimes possible to obtain global results, in such a way that reduced models may be constructed with clear error bounds. In nonlinear systems, as we have seen in Chapter 1, the story is much more complicated and interesting. There is a long history of classical results in dynamical systems, often driven by applications e.g. nonlinear mechanics, that try to circumvent this property of mathematical formulations; perturbation theory has been very successful in this context. However, it is very important to understand that perturbation theory is essentially a theory of how to use linear theory to extent knowledge of some known solution, equation, geometry — this is of course a simplified view, but it is a reminder of the conservation of complexity.

It is this restriction to local analysis which prevents rigorous construction of globally valid reduced models. In our work the construct falls in the category of local analysis around an attracting subset of the high-dimensional phase space, i.e., we limit our reduced model to a subspace for which a mathematical framework exists. Another group of methods base the reduced models on statistical observations, i.e., these methods ignore the apparent limitations of the theory of dynamical systems, with the sole ambition to construct useful models. Clearly, each approach has their advantages and disadvantages.

Next, we give a short overview of the main directions in reductive methods and place them in a broader setting of reduction in mathematics; but before we do that we define exactly what we mean with the term *dimension reduction* in the current study. Consider the following,

**Definition 3.1** An *ideal* **dimension reduction** of a dynamical system satisfies the following
(a) reduction of phase space dimension,
(b) preservation of bifurcation structures,
(c) preservation of $\omega$-limit set structure,
(d) preservation of the quantitative measures connected to (b)-(c).

Another way of stating this in a short and precise manner is that an ideal dimension reduction preserves the skeleton and the quantitative measures of the reference dynamical system. The addition of '*ideal*' in the above definition is used to underscore that dimension reduction may be useful without satisfying all of (a)-(d). With the theoretical background of Chapter 1 the definition 3.1 should be self-explanatory, however, we note (c) is to account for special types of attracting sets.

## 3.1 An overview of some classes of reduction methods

In the deterministic dynamical systems where reduction methods may be applied, the a priori assumption is often that the dynamics after short transients are restricted to some low-dimensional attractors in phase space. The dynamics on these attractors can be arbitrarily complicated, e.g., fixed points, periodic/heteroclinic/homoclinic orbits, tori and chaos may be embedded.

The short transients are related to a more specific common denominator of the different methods, i.e., the observation of time-scale separations paves the way for the subsequent restriction to the slow time scale. Be aware that the choice of formulation with *slow* and *fast* time scales is sometimes misleading, since more time scales can be involved; as an example consider a solution to some linear ODE, $x(t) = x_0 \exp(\alpha t)\cos(\omega t)$, it is evident that there are two time scales determined by the dissipation parameter $\alpha > 0$ and the frequency parameter $\omega$. This difference is more subtle than one may expect (cf. Section 1.5.1 where the dissipative time scale sets the scene), in particular, the focus in the current work is on reductive methods that rely on *spectral gaps*.

### 3.1.1 Geometric Singular Perturbation theory

There is a wide range of methods that are based on geometric singular perturbation theory (GSP), see [Fen79]. The method is based on an extreme separation of time scales in a dynamical system; consider the following system,

$$\begin{aligned} \dot{x} &= f(x, y, \epsilon), \\ \epsilon\dot{y} &= g(x, y, \epsilon), \end{aligned} \tag{3.1}$$

where $\epsilon \in \mathbb{R}$ and $f : \mathbb{R}^k \times \mathbb{R}^{n-k} \times \mathbb{R} \to \mathbb{R}^k$ and $g : \mathbb{R}^k \times \mathbb{R}^{n-k} \times \mathbb{R} \to \mathbb{R}^{n-k}$ are assumed smooth. The perturbation problem is called singular because the solutions change character in a singular manner with the parameter $\epsilon$.

There are two expected time scales in the dynamical system (3.1), the evolution of $x$ is $\mathcal{O}(1)$ and $y$ is $\mathcal{O}(1/\epsilon)$. As $\epsilon$ approaches zero the *spectral gap* becomes very large and in the limit where $\epsilon = 0$, Equation (3.1) becomes,

$$\begin{aligned} \dot{x} &= f(x, y, 0), \\ 0 &= g(x, y, 0). \end{aligned} \tag{3.2}$$

The interpretation of this situation is that the 'dynamics' of $y$ is instantaneous compared to that of $x$. Now assume that we are interested in the dynamics on

a specific compact subset $K_x \times K_y$ of phase space where

$$M_0 = \{(x, y) : g(x, y, 0) = 0 \wedge (x, y) \in K_x \times K_y \subset \mathbb{R}^n\}, \tag{3.3}$$

and assume that on this set $D_y g$ is regular such that, $M_0 = \text{graph}(h_0)$ where $y = h_0(x)$ for $x \in K_x$; subscripts in $M_0$, $h_0$ are used to underscore that $\epsilon = 0$. The construction of such zero sets was discussed in Chapter 1. In this case the dimension reduction is immediate since the reduced system is restricted to the $k$-dimensional compact manifold $M_0$ with boundary, i.e.,

$$\dot{x} = f(x, h_0(x), 0), \tag{3.4}$$

where the dynamical system is then $k$-dimensional. We further assume that $M_0$ is a normally hyperbolic manifold, for $\epsilon = 0$ this amounts to demanding that the eigenvalues of $D_y g$ for all $(x, y) \in M_0$ are not on the imaginary axis.

Under these conditions and for sufficiently small $\epsilon > 0$, [Fen79] there exists a slow manifold $M_\epsilon$ diffeomorphic to $M_0$, locally invariant under Equation (3.1) and it lies within $\mathcal{O}(\epsilon)$ of $M_0$. This also implies that $M_\epsilon = \text{graph}(h_\epsilon)$ where $y = h_\epsilon(x)$ with $x \in K_x$. Note that just as with the center manifolds the slow manifold $M_\epsilon$ is not necessarily unique.

This result is very suitable for dimension reduction of dynamical systems with small parameters that introduce large spectral gaps. In chemical reaction kinetics several methods have close ties to GSP, e.g., computational singular perturbation (CSP) [LG94], intrinsic low-dimensional manifold (ILDM) [MP92] and an iterative method [RF90]. In [KK02] the asymptotic connections to GSP are investigated for ILDM and the iterative method and in [ZKK04] the connection is made for CSP.

From the point of view of practical applications GSP may be applied to a wide range of problems, and in systems that clearly have time scale separation but no explicit small parameters it is sometimes useful to temporarily to multiply some terms (expected to be small) with an $\epsilon$ to the differential equation, do the calculations and set $\epsilon = 1$. It should be remarked that the slow manifolds may still be practically useful even when $\epsilon$ is not small. However, this is application specific.

From a numerical point of view these methods typically end up as a problem of obtaining solutions to a sequence of nonlinear equations of dimension scaling with the dimension of the fast variables $y$; and the sequence is of length proportional to the order of the approximation.

### 3.1.2 Linear projection methods

This category of reduction methods can be understood by linear algebra, and by recollecting Section 1.2. Consider a dynamical system,

$$\dot{x} = f(x), \tag{3.5}$$

where $x \in \mathbb{R}^n$ and $f$ is the smooth function $f : \mathbb{R}^n \to \mathbb{R}^n$. For simplicity let $\phi_1, \ldots, \phi_n$ be an orthonormal basis for $\mathbb{R}^n$ and consider $x$ in this basis,

$$x(t) = \sum_{i=1}^{n} a_i(t)\phi_i. \tag{3.6}$$

Furthermore, define the subspace $U_r = \text{span}(\phi_1, \ldots, \phi_r)$ where $0 < r < n$; a dimension reduction based on linear projections is then the reduction to the linear subspace $U_r$, i.e., the solutions $x_r(t) \in U_r$. Explicitly we may write,

$$x_r(t) = \sum_{i=1}^{r} a_i(t)\phi_i, \qquad \text{where} \qquad a_i(t) = \phi_i^T x(t). \tag{3.7}$$

Galerkin's principle is then to force the residual of the dynamical system to be in the orthogonal complement of $U_r$; this amounts to,

$$\phi_i^T(\dot{x}_r - f(x_r)) = 0, \qquad \text{for } i = 1, \ldots, r. \tag{3.8}$$

letting $a(t) \in \mathbb{R}^r$ and defining the function $\tilde{f}_j(a) = \phi_j^T f(a_i\phi_i)$, where repeated indices are summed, the reduced dynamical system is then,

$$\dot{a} = \tilde{f}(a), \tag{3.9}$$

where $\tilde{f} : \mathbb{R}^r \to \mathbb{R}^r$. Observe that the linear projections have a very fundamental problem; as opposed to methods that reduce the dynamics to approximate invariant manifolds, linear projection methods completely disregard the possibility of nonlinear interactions with the orthogonal complement $U_r^\perp = \text{span}(\phi_{r+1}, \ldots, \phi_n)$ in $\mathbb{R}^n$. This is very unfortunate and there is no easy way to tell if the linear projections cut the skeleton of the dynamical system in a fatal way.

A crucial step that we ignored initially is to comment on how the linear projections are chosen, i.e., how are the $\phi_i$'s determined? When there is no natural choice of subspace $U_r$ based on the dynamical system a priori one way which has proven useful is the following, see e.g., [RCM04][Row05][KGVB05]. Assume that we have computed an ensemble of observations at discrete times $\{t_1, \ldots, t_m\}$. Define the data matrix,

$$X = \Big[x(t_1), x(t_2), \ldots, x(t_m)\Big] \in \mathbb{R}^{n\times m}. \tag{3.10}$$

Each column represents an observation of a trajectory at some time in phase space, note that since the system is autonomous the time-dependence is in some sense arbitrary because this analysis is only based on spatial geometry. Now, imagine that the $m$ observations make up a point cloud in $\mathbb{R}^n$, then we want to find an $r$-dimensional hyperplane that approximates the point cloud best, i.e., where the sum of the distances to the hyperplane is minimal. This is a least squares maximization problem,

$$\text{maximize } \|\Phi X\|^2, \tag{3.11}$$

where $\Phi = \left[\phi_1, \ldots, \phi_r\right]$; the $r$ basis vectors in $\Phi$ that span the hyperplane can be found, via e.g., principal component analysis (PCA), proper orthogonal decomposition (POD) or the singular value decomposition (SVD).[1]

For completeness let us note that the rectangular matrix $X$ may be represented by its SVD,

$$X = USV^T, \tag{3.12}$$

where $U \in \mathbb{R}^{n\times n}$ are the left singular vectors, $S \in \mathbb{R}^{n\times m}$ is a diagonal matrix of singular values (ordered highest to lowest), $V \in \mathbb{R}^{m\times m}$ is the matrix of the right singular vectors and the matrices $U$ and $V$ have orthonormal columns such that,

$$U^T U = I, \tag{3.13}$$
$$V^T V = I. \tag{3.14}$$

The optimal $r$-dimensional hyperplane is spanned by the $r$ first columns of $U$.

We remark that it is of course possible to consider a different weighted norm in this process, i.e., this particular choice may depend of the dynamical system at hand; nevertheless in nonlinear systems there is in general no reason to expect that the covariance is a good measure for the representation of the skeleton of the dynamical system, thus it is not a surprise that the method fails sometimes although practically all the covariance is represented.

One of the direct advantages of the linear projection methods is that they are simple and still have the potential to work efficiently in very high-dimensional systems.

[1] In statistics when $X$ is centered the matrix $\frac{1}{n}XX^T$ is known as the covariance matrix, hence the choice of $\Phi$ is chosen such that it maximizes covariance.

### 3.1.3 Nonlinear normal modes

The method of nonlinear normal modes (NNM) has proven very useful in a multitude of applications and the method seems to be the most popular choice for dimension reduction in the nonlinear mechanics communities, see e.g., the recent review [AM13]. NNMs are not clearly fixed to one definition in the mathematical sense, for example, one definition due to Rosenberg is for NNMs in conservative systems, *vibration in unison*, and this is not necessary for the NNMs found via the invariant manifold approach due to Shaw and Pierre [SP91]; we shall disregard this ambiguity and instead only consider the latter in the context of dissipative/non-conservative systems.

As noted in [SP93] the mathematical construct of nonlinear normal modes via the invariant manifold approach is inspired by the corresponding theory of invariant manifolds in dynamical systems. A particularly important theory is the center manifold theory (generalized to sets) or the theory developed by Fenichel [Fen71] for normally hyperbolic invariant manifolds, and quite possibly related perturbation results even earlier. Typically, since the method is developed for mechanical vibration problems, the considered dynamical systems are stated in second-order form,

$$M\ddot{x} + C\dot{x} + Kx = \epsilon f(x, \dot{x}, t), \tag{3.15}$$

where $x \in \mathbb{R}^n$, $M, C, K \in \mathbb{R}^{n\times n}$ and $f : \mathbb{R}^n \times \mathbb{R}^n \times \mathbb{R} \to \mathbb{R}^n$. ODEs of this format are often obtained after numerical discretizations of PDEs based on Newton's or Euler's laws (cf. Appendix E); the spatial dependencies are included in the structure of the mass, damping and stiffness matrices. Note that, in some cases Equation (3.15) is not general enough, i.e., $f$ may depend on the acceleration $\ddot{x}$ and this would make the ODE implicit. For simplicity of the argument, we assume periodic time dependence and furthermore that a coordinate change with transformation matrix $V$, $x = Vp$ and $q = \dot{p}$ and the addition of time as an explicit variable may lead to the following transformation of Equation (3.15),

$$\begin{aligned} \dot{p} &= q, \\ \dot{q} &= -\Omega^2 p - 2\xi\Omega q + \epsilon\tilde{f}(p, q, \theta), \\ \dot{\theta} &= 1, \end{aligned} \tag{3.16}$$

where $\xi > 0$, $\epsilon \in \mathbb{R}$, $p, q \in \mathbb{R}^n$, $\theta \in \mathbb{S}^1$, $\Omega \in \mathbb{R}^{n\times n}$ is a positive-definite diagonal matrix (ordered $0 < \omega_1 \leq \omega_2 \leq \ldots \leq \omega_n$ where $\omega_i := \Omega_{ii}$) and $\tilde{f} : \mathbb{R}^n \times \mathbb{R}^n \times \mathbb{S}^1 \to \mathbb{R}^n$. This form is referred to as the modal form, and the damping is linear modal damping; setting $\epsilon = 0$ and disregarding the periodic coordinate $\theta$ the eigenvalues of the origin are $\lambda_k = -\xi\omega_k \pm i\omega_k\sqrt{1-\xi^2}$; consequently the origin is a hyperbolic asymptotically stable fixed point.

Letting $\epsilon \neq 0$ the system becomes forced and the idea of the construction of

NNM is then to choose a master mode, e.g., the first degree of freedom $p_1, q_1$ and let all other degrees of freedom be slaved to the master mode and $\theta$, i.e.,

$$\begin{aligned} p_i &= P_i(p_1, q_1, \theta), \\ q_i &= Q_i(p_1, q_1, \theta), \end{aligned} \tag{3.17}$$

for $i \in \{2, 3, \ldots, n\}$. This introduces the standard invariance equations by plugging the relations (3.17) in Equation (3.16) and obtain,

$$\begin{aligned} D_{(p_1,q_1,\theta)} P_i \cdot \begin{pmatrix} \dot{p}_1 \\ \dot{q}_1 \\ \dot{\theta} \end{pmatrix} &= Q_i, \\ D_{(p_1,q_1,\theta)} Q_i \cdot \begin{pmatrix} \dot{p}_1 \\ \dot{q}_1 \\ \dot{\theta} \end{pmatrix} &= -\Omega^2 P_i - 2\xi\Omega Q_i + \epsilon \tilde{f}_i(p, q, \theta), \end{aligned} \tag{3.18}$$

for $i \in \{2, 3, \ldots, n\}$. In [JPS05] the coordinates of the master coordinates are transformed to polar coordinates, i.e., we let $(p_1, q_1) \mapsto (r, \phi)$; one of the reasons for doing this is to pave the way for a simple marching type method for constructing the invariant manifolds in intervals of $r$. We note that it is not strictly necessary to construct the invariant manifolds locally and patch them together, but this type of consideration of computational complexity is of great importance for practical purposes of dimension reduction, see e.g., the discussion in [PPS02]. Geometrically slices are matched to each other, e.g., if we want the invariant manifolds on the domain $(0, r_{\text{end}}] \times \mathbb{S}^1 \times \mathbb{S}^1$ then the invariance equation is first solved for $(0, \Delta r] \times \mathbb{S}^1 \times \mathbb{S}^1$ then $(\Delta r, 2\Delta r] \times \mathbb{S}^1 \times \mathbb{S}^1$ etc. $N$-times $r_{\text{end}} = N\Delta r$. They use a finite-dimensional function space $V$ for each slice composed of two linear basis functions in $N_r = 2$ and a Fourier/spectral basis in the two angular coordinates composed by $N_\phi$ and $N_\theta$ functions, hence the slaved modes are described by,

$$\begin{aligned} P_i(r, \phi, \theta) &= \sum_{j=1}^{N_r} \sum_{k=1}^{N_\phi} \sum_{l=1}^{N_\theta} a_{ijkl} R_j(r) \Phi_k(\phi) \Theta_l(\theta), \\ Q_i(r, \phi, \theta) &= \sum_{j=1}^{N_r} \sum_{k=1}^{N_\phi} \sum_{l=1}^{N_\theta} b_{ijkl} R_j(r) \Phi_k(\phi) \Theta_l(\theta), \end{aligned} \tag{3.19}$$

where $a, b \in \mathbb{R}^n \times \mathbb{R}^{N_r} \times \mathbb{R}^{N_\phi} \times \mathbb{R}^{N_\theta}$. This leaves $2(n-1) \cdot N_r \cdot N_\phi \cdot N_\theta$ unknowns to be determined for each slice. In [JPS05] the Galerkin method is the chosen approach to solve the invariance equation, hence the residual/defect of the approximation is forced out of the finite-dimensional approximating subspace $V$.[2]

[2] Our derivation here differs slightly, from that of the particular example in [JPS05] because the solution strategy in [JPS05] is adapted to take advantage of the nonlinearity being independent of velocities.

Explicitly, let $X$ denote the domain (the slice)

$$\int_X \left[ D_{(r,\phi,\theta)} P_i \cdot \begin{pmatrix} \dot{r} \\ \dot{\phi} \\ \dot{\theta} \end{pmatrix} - Q_i \right] \cdot R_j \Phi_k \Theta_l \, \mathrm{d}X = 0,$$

$$\int_X \left[ D_{(r,\phi,\theta)} Q_i \cdot \begin{pmatrix} \dot{r} \\ \dot{\phi} \\ \dot{\theta} \end{pmatrix} + \Omega^2 P_i + 2\xi\Omega Q_i - \epsilon \tilde{f}_i(p,q,\theta) \right] \cdot R_j \Phi_k \Theta_l \, \mathrm{d}X = 0,$$

for $i = 2, 3, \ldots, n$ and all $N_r \cdot N_\phi \cdot N_\theta$ combinations of $i, j, k$. If the integrals cannot be calculated analytically, then they are integrated via some suitable (Gaussian) quadrature scheme. Alternatively the problem may be reformulated slightly with Dirac delta weight functions such as to apply collocation. At this stage a finite-dimensional set of coupled nonlinear equations has been obtained, i.e., the invariant manifold problem is reduced to a zero-problem (cf. Chapter 1),

$$F(u) = 0, \tag{3.20}$$

where $u \in \mathbb{R}^{2(n-1)\cdot N_r \cdot N_\phi \cdot N_\theta}$ represents the unknowns $a_{ijkl}, b_{ijkl}$.

A few extra remarks are in place. It seems in [PPS02], definitely in [JPS05], that in the examples where the invariant manifolds are decomposed into smaller parts the computation of slice of the invariant manifolds are computed independently with respect to each other; while this has shown to work perfectly in a wide range of problems, there are some details that should be mentioned. When the invariant manifold is computed as one big piece, a solution it is necessarily a connected compact manifold with boundary, however, unless[3] boundary conditions are prescribed on an initial hypersurface then there is a continuum of invariant manifolds that solve the problem; consider e.g. the layer of trivial 'invariant manifolds'(/trajectories) $\dot{x} = 1$, $\dot{y} = 0$ or perhaps even more troubling the example in [Kel67] which was discussed in Chapter 1 which shows that center manifolds are non-unique even when satisfying the condition of tangency at the origin. The non-uniqueness implies that if the manifolds are computed in independent slices then collection of all slices is typically not going to be a connected compact invariant manifold with boundary, however this can be accounted for by stitching together slices through an averaging process. This is done in [JPS05]. It may be interesting to test the NNM invariant manifold construction by turning the method into a marching method, where the manifold is continuously grown, in fact this would reduce the number of unknowns by a

[3] This discussion needs much more detail than is meaningful to include in this presentation, however, readers that are more interested in nonlinear first-order PDEs (e.g. Equation (3.18)) may consult Evans [Eva10] for details on uniqueness, existence and the connection to the prescribed boundary conditions (characteristic vs. noncharacteristic).

at least factor of two and the approximated manifold would be constructed as a continuous and piecewise smooth manifold.

In this method the complexity is determined by the number of coupled nonlinear equations and as earlier mentioned this scales as $2(n-1)\cdot N_r \cdot N_\phi \cdot N_\theta$, and if we generalize it to $k$-dimensional invariant manifolds in $n$-dimensional dynamical systems then it scales as $(n-k)\cdot N^k$ where $N$ is the number of basis functions assumed to be the same in all independent variables. For manifolds with large codimension $(n-k)$ in $\mathbb{R}^n$ the method is challenged because it scales with the codimension. However, the subdivision in $r$ is already a good and quite substantial reduction since $N^k \mapsto 2\cdot N^{k-1}$.

We shall discuss the different alternatives to the approximation of invariant manifolds in more detail in Section 3.3.

## 3.2 Introduction to Paper C

While there exist many reductive methods most of them scale with the codimension of the reduced manifold and others are sensitive to the structure of the dynamics on and off the manifold. Amongst other things we address these two problems by applying the theory of normally hyperbolic invariant manifolds, in particular we apply an iterative method known as the *graph transform*. Previously, the graph transform has been applied primarily to manifolds without boundary, such as tori and periodic orbits. In [BHV07] the graph transform is applied to the construction of a two-dimensional manifold with boundary in a chemical kinetics application of codimension one, i.e., it is a three-dimensional dynamical system. In the current work we apply the graph transform to approximate $k$-dimensional attracting invariant submanifolds of dissipative dynamical systems which may also have a periodic time-dependence.

Paper C may be decomposed into five parts

1. Intro to the theory of normally hyperbolic invariant manifolds
2. Detailed description of the graph transform
3. Details of the numerical implementation
4. Dimension reduction of a problem from mechanics
5. Convergence study

While the background theory presented in Chapter 1 was sufficient for a relatively smooth entrance to Paper A, the topic of dimension reduction via the theory of *normally hyperbolic invariant manifolds* (NHIMs) is more difficult. The persistence theory of invariant manifold is generalized, but the intuition from the center manifold reduction is valueable in the practical understanding. We describe the graph transform in proper detail in the continuous case and give a detailed description of how it may be implemented numerically.

The method is tested on a mechanical system taken from [JPS05] in which dimension reduction is performed via the previously discussed NNM method of Shaw and Pierre.

Finally we perform a small convergence study, where the linear convergence rate of the graph transform is verified.

## 3.3 Discussions and future directions

In Paper C it was shown how one may apply the graph transform to approximate attracting invariant $k$-dimensional submanifolds, and the example which the method was tested on was an entirely positive test case. The violation of the overflowing boundary condition indicated no problems for suitably chosen flow time, i.e., flow times should be chosen such that the pre-image of the next iterate is not much bigger than the domain over which the manifold is approximated; or equivalently such that the pre-image is not too much outside the tubular neighborhood of the previous iterate. Although the violation of the overflowing boundary condition seems to be a mathematical problem and not a practical issue it should be handled in a future work on the mathematical aspects of the approach. Furthermore, subsequent to modifications of the boundary, the whole (unique) theory of convergence of the graph transform must be satisfied.

As opposed to most other methods the graph transform is largely independent of the dynamics on the manifold, and this makes it very robust compared to marching type methods; this is related to the property of the graph transform being a contraction mapping (under the hypotheses of Theorem 1 in Paper C). At the same time this iterative property of the graph transform also opens the possibility of a criterion for knowing wether or not a bifurcation has occurred outside the manifold, i.e., the hypothesis on the generalized Lyapunov-type numbers fails; this type of bifurcation criteria for a breakdown of the dimension reduction or a reduced model is quite unique and may prove very useful as it provides a clear measure wether or not the dimension reduction is valid in a tubular neighborhood. In general the breakdown is associated with a bifurcation

of the normally hyperbolic invariant manifold. In fact, for compact manifolds without boundary, such as a periodic orbit or torus the equivalent loss of normal hyperbolicity is a bifurcation parameter, see e.g., [BOV97],[Rei00].

As it was remarked also in Paper C the complexity of the graph transform method is superior in complexity, because the Newton steps only needs to be solved for many uncoupled $k$-dimensional problems; this also renders the method trivially suitable for parallel computing. Most other methods have complexity in their Newton steps that also scale with the codimension of the $k$-dimensional[4] manifold, i.e., the number of slaved variables $n - k$.

Furthermore, the graph transform is conceptually simple to understand and encode/implement numerically; this is even the case for general $k$-dimensional manifolds. In comparison, marching methods or other covering methods are often more complicated to implement for $k > 3$.

While there are quite a few advantages of using the graph transform method, it has a main disadvantage; the convergence of the graph transform is linear (see [Rei00],[BHV07]) and therefore it is crucially dependent on the spectral gap or in other words how strong the normal attraction/contraction is. This is an application-dependent property but it differs from, e.g., marching methods which do not suffer from a small spectral gap.

Before we go on to discuss some of the general challenges and suggestions for improvements in dimension reduction we conclude the discussion of the graph transform with a remark on comparisons between dimension reduction methods. As it was argued above the graph transform has its advantages and disadvantages. The same applies for NNM, marching methods, linear projection methods, GSP and so on; in particular each of these methods apply to certain classes of problems, the question of wether or not a dimension reduction method is good or bad is nonsense. Such a statement can only be meaningful if it is related to an application (dynamical system). An a priori determination of which dimension reduction method to apply for a given application depends on theoretical and practical considerations; while the former is concerned with direct assessments on properties of the system, the latter opens up for a different type of constraints such as efficiency and precision.

Being based on mathematical theory, dimension reduction is only limited by the abstract properties of the dynamical systems, the methods know no borders between fields and have proven very useful in a multitude of applications; but even if it has been successfully applied in many practical applications there are some important limitations and challenges that seem difficult to overcome

[4] In the forced system it was even $k - 1$ because time is trivial.

without compromises.

From a mathematical point of view the compromises introduce assumptions that are difficult to substantiate. The first and foremost problem is that dimension reduction of general dynamical systems remains to be a local approximation, there exist no practical results for global dimension reduction. There is a concept of global attractors called *inertial manifolds*. Inertial manifolds are finite-dimensional manifolds embedded in an infinite-dimensional space where all initial conditions converge to the inertial manifold exponentially fast, i.e., it is a global attractor with exponential attraction rate. As an example, assume the solutions of a PDE may be represented as $u(t,x) = \sum_{i=0}^{\infty} c_i(t)w_i(x)$ where $w_i$'s are an orthogonal basis for the Hilbert space $\mathcal{H}$; we can imagine that if the PDE has an inertial manifold then the idea is that there exist an $n$ large enough such that

$$c_i = \Phi(c_1, c_2, \ldots, c_n) + error, \quad i > n \tag{3.21}$$

where $\Phi$ is the function that determines the state of the ith mode $i > n$ and $||error|| < C\exp(-\lambda t)$ and $C, \lambda > 0$. This principle is very reminiscent of the reduction techniques that we already rely on in center manifold reduction, $\lambda$ is also related to a spectral gap condition. For certain PDEs the existence of inertial manifolds may be proven, see e.g., [Rob01]. While the existence of an inertial manifold is reassuring it is not practical; from [Tem97] we take the following quote,

> In many cases the dimension of the attractor $\mathcal{A}$ and thus the number of required parameters is too large for existing computational resources.
> For instance, in fluid mechanics the number of degrees of freedom (dim $\mathcal{A}$) is of the order of $10^9$ in aeronautical and wind-tunnel experiments, and up to order $10^{20}$ in geophysical flows (meteorology).

Here $\mathcal{A}$ is the global attractor. It is clear that these attractors are not what we approximate; not even the reference/full models of aeronautical computational fluid dynamics (CFD) problems would have this many degrees of freedom. For practical purposes the ideas are then relaxed a lot and one may find papers that consider the construction of so-called Approximate Inertial Manifolds (AIMs). The AIM is constructed by a slaving principle that is very reminiscent of the ones used in center manifold reduction and sometimes it is referred to as nonlinear Galerkin; the method is practical but unless it is proven globally valid the name AIM is a bit misleading.

From a computational point of view two properties are particularly important to consider for the reduction methods that are based on approximations of attracting invariant submanifolds of high-dimensional phase space. Let $n$ be the dimension of the phase space and $k$ the dimension of the supposed attracting invariant submanifold; it is tempting to simply state that the minimal number of nonlinear equations that needs to be solved for in the determination of the submanifold scales with its codimension $(n-k)$ by considering it as the problem of determining the zero set of

$$F(x, y) = 0, \tag{3.22}$$

where $F : \mathbb{R}^k \times \mathbb{R}^{n-k} \to \mathbb{R}^{n-k}$ is smooth. This type of scaling would be disquieting because the long term ambition is to be able to perform dimension reduction of systems with truly large $(n-k)$. A marching method of Guckenheimer and Vladimirsky [GV04] is of this type and for low codimension it is fast, an example is given for the approximation of the stable manifold of the hyperbolic equilibrium at the origin in the Lorenz system (i.e. a codimension one manifold). We shall not discuss the method in detail but we note that marching methods are in general sensitive to the dynamics (contraction/expansion) both on and off the submanifold. As a trivial example consider the two-dimensional linear system with a stable fixed point at the origin,

$$\begin{aligned} \dot{x} &= -x, \\ \epsilon\dot{y} &= -y, \end{aligned} \tag{3.23}$$

where $0 < \epsilon \ll 1$. In this simple case the $x$-axis is an invariant manifold $M$ and any initial condition will approach it very fast $\propto \exp(-\frac{1}{\epsilon}t)$. Marching methods for calculating the invariant manifold $M$ is then done by solving the invariance equation setting $y = h(x)$ with $\partial_x h(0) = 0$,

$$\epsilon\dot{y} = -y, \quad \Rightarrow \partial_x h = \frac{1}{\epsilon} \cdot \frac{y}{x}. \tag{3.24}$$

In this case it is clear that $y = h(x) = 0$ solves the problem, however consider a discretized marching method where we initialize from the origin. If at some step we are a little bit off the $x$-axis then the derivative explodes because $\epsilon$ is very large. If on the other hand the $x$-axis was an unstable manifold, i.e., $\dot{x} = x$ then the scheme would be very stable.[5] The Galerkin-based NNM reduction is similarly done by expanding the slow manifold from the origin. At the same time this has the opposite effect on the graph transform which actually only converges faster as $\epsilon \to 0$.

Another practical challenge is related to the representation of the invariant manifolds. If we consider a meshgrid being a cube with $m$ basis functions in each of

[5] In that case the $x$-axis would also be an overflowing normally hyperbolic invariant manifold.

the $k$ dimensions of the manifold then $m^k$ is the number of k-dimensional boundary value problems to be solved[6]; for the Galerkin-based NNM then as previously mentioned each slice needs to solve a system of roughly $(n-k)\cdot 2m^{(k-1)}$ equations. This is somehow the curse of dimensionality, the power $k$ term is truly a challenge, and it makes it very important to have a very sparse representation of the manifold, i.e., $m$ should be minimized; essentially for large codimension and manifold dimension the number of coefficients to the basis functions explode and the numerical computations become very memory intensive. It is a highly non-trivial task to solve though; the construction of a sparse representation of functions without sacrificing too much accuracy is a difficult problem. In Paper C we used a spline basis with uniform grids. There it may be beneficial instead to consider splines that allow local refinement, e.g., hierarchical splines.

In conclusion the graph transform is crucially dependent on the spectral gap and is for this reason not suitable for dynamical systems with small spectral gaps if it is implemented along the lines of the numerical methods in Paper C. On the other hand the method has great potential to perform dimension reduction on high-dimensional problems because it does not scale with the codimension in the Newton steps as many other methods. Additionally a theory of convergence is available.

[6]If time is one of the $k$ variables then the number of bvps to be solved is $m^{k-1}$

Appendix A

# Bifurcation Analysis of a Smoothed Model of a Forced Impacting Beam and Comparison with an Experiment

# Bifurcation analysis of a smoothed model of a forced impacting beam and comparison with an experiment

M. Elmegård* B. Krauskopf† H.M. Osinga‡ J. Starke§
J.J. Thomsen¶

August 16, 2013

**Abstract**

A piecewise-linear model with a single degree of freedom is derived from first principles for a driven vertical cantilever beam with a localized mass and symmetric stops. The resulting piecewise-linear dynamical system is smoothed by a switching function (nonlinear homotopy). For the chosen smoothing function it is shown that the smoothing can induce bifurcations in certain parameter regimes. These induced bifurcations disappear when the transition of the switching is sufficiently and increasingly localized as the impact becomes harder. The bifurcation structure of the impact oscillator response is investigated via the one- and two-parameter continuation of periodic orbits in the driving frequency and/or forcing amplitude. The results are in good agreement with experimental measurements.

*Department of Applied Mathematics and Computer Science, Technical University of Denmark, Matematiktorvet, Building 303B, 2800 Kgs. Lyngby, Denmark, melm@dtu.dk.

†Department of Mathematics, University of Auckland, Private Bag 92019, Auckland 1142, New Zealand, b.krauskopf@auckland.ac.nz.

‡Department of Mathematics, University of Auckland, Private Bag 92019, Auckland 1142, New Zealand, h.m.osinga@auckland.ac.nz.

§Department of Applied Mathematics and Computer Science, Technical University of Denmark, Matematiktorvet, Building 303B, 2800 Kgs. Lyngby, Denmark, jsta@dtu.dk

¶Department of Mechanical Engineering, Technical University of Denmark, Nils Koppels Alle 404, DK-2800 Kongens Lyngby, Denmark, jjt@mek.dtu.dk

# 1 Introduction

In mechanical engineering applications piecewise-smooth dynamical systems are often encountered through structural interactions. This is especially the case in the field of machinery dynamics, e.g., with vibro-impact, and with friction systems and processes: *Vibro-impact systems* and processes involve repeatedly colliding elements and vibrations with abrupt changes in velocity and forces. Applications include devices to crush, grind, forge, rivet, drill, punch, tamp, print, tighten, pile, cut, and surface treat a variety of materials and objects, at frequencies ranging from sub-Hertz to ultrasonic [1], [2], [3]. In other contexts vibro-impact occurs as an unwanted side effect, often producing noise and wear, such as with devices operating with stops and clearances, e.g., gear wheels, rotors, rattling heat exchanger tubes, and guides for roller chain drives. Here, discontinuities are typically due to abrupt changes in the restoring forces or boundary conditions, i.e. on a time scale much smaller than those associated with the free oscillation frequencies of a system. *Friction systems* and processes are an inherent or purposefully implemented part of many technical devices, including automotive brakes and clutches and bowed musical instruments, some are unwanted in other apparatus, such as in chatter in metal cutting, creaking doors, and squealing tramways and disc brakes [4], [5]. Here, discontinuities appear in the dissipative terms of the equations of motion, typically as abrupt changes in dissipative forces with the sign changes of the relative interface sliding velocities.

The strong nonlinearity associated with such discontinuous systems and processes preclude exact analytical solution in all but a few simple cases and, in general, bifurcation analysis is far from straightforward [6]. Analytical approaches are typically approximate; they include stitching [3], i.e. integrating motions between impacts or other discontinuities, and using kinematic impact conditions to switch solution intervals; averaging; harmonic linearization [1]; and various kinds of discontinuous transformations of variables, e.g., see [7]. Details about some of the mathematical methods for piecewise-smooth systems can be found, e.g., in [8]. However, in most cases one needs to resort to or complement the analysis with numerical solutions of the equations of motion [9].

One of the main modeling challenges emerges from the fact that the continuum physical laws of impacts, friction etc. are not well understood. Hence, while the equations of motion for many smooth mechanical systems can be derived directly from the theory of elasticity, the modeling of mechanical systems with impacts and/or friction involves identifying suitable reaction laws. This results in a range of modeling decisions that are often problematic to substantiate theoretically. This is both in terms of the mathematical structure of the reaction laws, as well as the extra parameters that need to be estimated. Under these conditions it is very advantageous to be able to make comparisons with experimental measurements to test the given model.

In this paper we construct a mathematical model for a vibro-impacting cantilever of which experiments were performed and reported in [10]; see Figure 1 for a sketch of the experimental setup. In [10], the authors perform control-based

bifurcation analysis of the experiment, i.e., real-time bifurcation analysis of a mechanical vibro-impacting system. The method of control-based continuation is a method that makes it possible to perform bifurcation analysis of systems for which no mathematical model is given; the method was recently developed in [11] and demonstrated in a rotating pendulum experiment in [12]. Since then, control-based continuation has been used to investigate the bifurcation structures of mechanical experiments, such as the current case of a cantilever beam with symmetric mechanical stops [10] and a nonlinear energy harvester [13], [14]. The model derived here deals with the smooth modeling of small-amplitude vibrations of a driven cantilever beam under the influence of symmetric stops, and it concludes with a comparison with experimental measurements. In Section 2 we derive the single-degree-of-freedom model of a cantilever beam that vibro-impacts on symmetric stops. The structural mechanics of the model is based on the Euler-Lagrange beam equation and the reduction is inspired by the Galerkin step in [15] and [16]. In Section 3 a smooth version of the dynamical system is constructed by a nonlinear homotopy. In Section 4 numerical bifurcation analysis of the smoothing procedure is performed in order to test that the bifurcation results are robust with respect to the smoothing homotopy parameter. In Section 5 the model results are compared with experimental measurements.

# 2 Mathematical model

A mathematical model for the mechanical vibrations of a cantilever beam with symmetric mechanical stops, as sketched in Figure 1, is derived. In Section 2.1 the governing PDE and the main assumptions for its validity are given. In Section 2.2 the structure of the single-degree-of-freedom model is derived by Galerkin's method, but without an explicit choice for the approximating subspace, i.e., a mode shape is not chosen explicitly. In Section 2.3 the model parameters are estimated and compared with values fitted to experimental data.

## 2.1 Transverse vibration of a cantilever with a lumped mass

Formally the PDE is derived by Euler-Bernoulli beam theory, for small-amplitude transverse vibrations of a slender cantilever. Furthermore, the cantilever is harmonically driven and has a lumped mass $m$ attached. Following, e.g., [17], [18], the complete system can be derived as

$$\Big(m\delta(z-L_m)+\rho A_0\Big)\ddot{u}+EIu''''+\mu\dot{u}''''=0, \tag{1a}$$

$$u'(0,t)=u''(L,t)=u'''(L,t)=0 \quad \text{and} \quad u(0,t)=v_0(t). \tag{1b}$$

Here, $u=u(z,t)$ is the transverse displacement in inertial coordinates, $z$ is the axial coordinate; the overdot denotes derivation w.r.t. time $t$, and the prime denotes derivation w.r.t. space $z$. Furthermore, $\delta(\cdot)$ is the Dirac delta distribution; $v_0(t)=A\cos\omega t$ describes the harmonic excitation of the clamped base; $L$

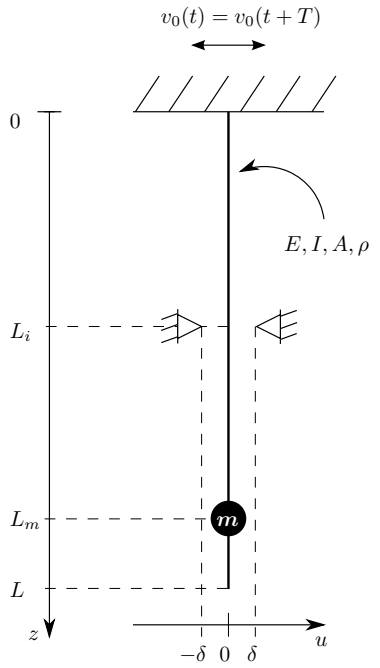


Figure 1: Experimental setup of the vertical cantilever beam of length $L$, with a lumped mass point $m$, symmetric mechanical stops at a transverse distance $\delta$ and a periodic excitation $v_0(t)$ of the clamped boundary. In the experiment; $E = 2 \cdot 10^{11}\,\mathrm{Pa}$, $I = 2.08 \cdot 10^{-12}\,\mathrm{m}^4$, $A = 2.5 \cdot 10^{-5}\,\mathrm{m}^2$, $\rho = 8 \cdot 10^3\,\frac{\mathrm{kg}}{\mathrm{m}^3}$, $m = 0.2116\,\mathrm{kg}$, $\delta \approx 10^{-3}\,\mathrm{m}$, $L_m = 0.1275\,\mathrm{m}$, $L_i = 0.071\,\mathrm{m}$ and $L_m = 0.1275\,\mathrm{m}$ and $L = 0.161\,\mathrm{m}$.

is the beam length; $\rho$ is the beam density; $A_0$ is the cross-sectional area of the beam; $\mu$ is the coefficient of stiffness proportional damping; $E$ is the modulus of elasticity; $I$ is the cross section area moment of inertia; and $L_m$ is the axial position of the attached mass. In a co-moving frame, using $u = \eta + v_0$, the governing equations transform to

$$\Big(m\delta(z - L_m) + \rho A_0\Big)(\ddot{\eta} + \ddot{v}_0) + EI\eta'''' + \mu\dot{\eta}'''' = 0, \tag{2a}$$

$$\eta(0,t) = \eta'(0,t) = \eta''(L,t) = \eta'''(L,t) = 0. \tag{2b}$$

The equations of motion in the co-moving frame (2) are equivalent to a cantilever beam with a lumped mass under the influence of an axially uniformly distributed harmonic forcing, and a time-harmonic point force proportional to the lumped mass at the position $z = L_m$.

## 2.2 Reduced ODE model

The configuration space of the cantilever in the PDE description is infinite dimensional. In order to construct a finite-dimensional description an approximating subspace is chosen for the spatial coordinate. Let $\eta(z,t) = \sum_{i=1}^{N} a_i(t)\phi_i(z)$, where all $\phi_i(z)$ satisfy the essential boundary conditions. Galerkin's method is then used to obtain a finite-dimensional ODE

$$\int_0^L \left[\Big(m\delta(z-L_m) + \rho A_0\Big)(\ddot{\eta} + \ddot{v}_0) + EI\eta'''' + \mu\dot{\eta}''''\right]\phi_j(z)\mathrm{d}z = 0. \tag{3}$$

After applying essential and natural boundary conditions via integration by parts, Equation (3) can be written as

$$\mathbf{M}\ddot{\mathbf{a}} + \mathbf{C}\dot{\mathbf{a}} + \mathbf{K}\mathbf{a} + \ddot{v}_0\mathbf{d} = 0, \tag{4}$$

where

$$M_{ij} = m\phi_i(L_m)\phi_j(L_m) + \rho A_0\langle\phi_i, \phi_j\rangle, \tag{5a}$$
$$C_{ij} = \mu\langle\phi_i'', \phi_j''\rangle, \tag{5b}$$
$$K_{ij} = EI\langle\phi_i'', \phi_j''\rangle, \tag{5c}$$
$$d_i = m\phi_i(L_m) + \rho A_0\langle 1, \phi_i\rangle. \tag{5d}$$
$$a_i = a_i(t). \tag{5e}$$

Here the angle brackets denote the inner-product $\langle f, g\rangle = \int_0^L fg\,\mathrm{d}z$. Equation (4) is a second order linear ODE with modal amplitudes $\mathbf{a}$, mass $\mathbf{M}$, damping $\mathbf{C}$ and stiffness $\mathbf{K}$ matrices and a time-dependent force vector $\ddot{v}_0\mathbf{d}$. When such a dynamical system is driven near or at its lowest resonance (the frequency corresponding to the smallest eigenvalue of the matrix $\mathbf{M}^{-1}\mathbf{K}$), quantitatively good results can be obtained even with a single-degree-of-freedom model, because all higher-order modes are expected to have negligible amplitudes in comparison. In addition, all higher-order modes are increasingly damped under the assumption that the damping is stiffness proportional, cf. Equations (5) where $\mathbf{C} \propto \mathbf{K}$. In the contact phase the mechanical stop moves the imaginary part of the eigenspectrum to higher values, i.e. the stiffness increases. Combining (5c) with the natural assumption that the beam shape in the contact phase has larger curvature in the neighborhood of the mechanical stop, it can be expected that the lowest eigenfrequency of the beam increases when in contact.
To obtain a single-degree-of-freedom model, we let $\eta(z,t)$ be the continuous, piecewise-defined, function

$$\eta(z,t) = \begin{cases} a(t)\phi_f(z), & |a| < \Delta, \\ \Delta\,\mathrm{sgn}(a)\phi_f(z) + (a(t) - \Delta\,\mathrm{sgn}(a))\phi_c(z), & |a| \geq \Delta, \end{cases} \tag{6}$$

where $\mathrm{sgn}(\cdot)$ denotes the sign-function, subscripts $f$ and $c$ denote "free" and "contact", respectively, and $\Delta$ is the displacement amplitude of the mass point

at which the beam grazes the mechanical stop. In what follows it is assumed that the cantilever displacement change is small compared to the change in curvature along the beam between solutions in free flight and contact phase. As a consequence we have

$$0 < \frac{|\eta_c - \eta_f|}{L^2(\eta_c'' - \eta_f'')} \ll 1, \tag{7}$$

where $\eta_f$ is a free configuration and $\eta_c$ is a contact configuration. Here, we assume that the beam mass is negligible relative to the lumped mass, i.e., $\frac{\rho A_0 L}{m} \ll 1$. Moreover, the following relations between the parameters in free flight and the contact phase are assumed:

$$c_c = c_f(1+\beta), \tag{8a}$$
$$k_c = k_f(1+\alpha), \tag{8b}$$
$$m_c = m_f = m(1+\gamma), \tag{8c}$$
$$d_c = d_f(1+\nu), \tag{8d}$$

where the relative changes in damping $\beta$ and stiffness $\alpha$ are large compared to $\gamma$ and $\nu$, respectively. Here we neglect the mass increment with $\gamma$ while retaining the forcing increment with $\nu$ for bookkeeping and later use. Dropping the subscripts, the system is then given by

$$m\ddot{a} + c\dot{a} + ka + d\ddot{v}_0 = 0, \qquad \text{for } |a| < \Delta, \tag{9a}$$
$$m\ddot{a} + c(1+\beta)\dot{a} + k(1+\alpha)a + \Gamma\,\mathrm{sgn}(a) + d(1+\nu)\ddot{v}_0 = 0, \qquad \text{for } |a| \geq \Delta. \tag{9b}$$

Here, the constant $\Gamma = -\alpha\Delta$ balances the static reaction forces of the beam at the mechanical stop, i.e., the beam is bent and the elastic forces push it back towards the unbent state; this implies that the restoring force is continuous and piecewise linear. At $a = \pm\Delta$ the mechanical stops are reached. Let the clamped basepoint be harmonically moved, i.e., $v_0 = A\cos(\omega t)$. Rescaling and nondimensionalising the system by $t \mapsto \omega_1^{-1} t$ and $a \mapsto \Delta a$, where $\omega_1 = \sqrt{\frac{k}{m}}$, and defining $\Omega = \frac{\omega}{\omega_1}$, $2\xi = \frac{c}{m\omega_1}$, and $I = \frac{d}{m}\frac{A}{\Delta}$, Equations (9) transforms into

$$\ddot{a} + 2\xi\dot{a} + a - I\Omega^2\cos(\Omega t) = 0, \qquad \text{for } |a| < 1, \tag{10a}$$
$$\ddot{a} + 2\xi(1+\beta)\dot{a} + (1+\alpha)a - \alpha\,\mathrm{sgn}(a) - I(1+\nu)\Omega^2\cos(\Omega t) = 0, \qquad \text{for } |a| \geq 1, \tag{10b}$$

which is the dynamical system analysed in Section 4.

An alternative approach yields an almost equivalent dynamical system: the model is derived by recognizing, a priori, that the mechanical system is analogous to that given in Figure 2. Using Newton's second law for the mass, one

arrives at the dynamical system

$$m\ddot{a} + k_1 a + \ddot{v}_0 = 0, \qquad \text{for } |a| < \Delta, \tag{11a}$$

$$m\ddot{a} + k_2 a + (k_1 - k_2)\Delta \operatorname{sgn}(a) + m\ddot{v}_0 = 0, \qquad \text{for } |a| \geq \Delta. \tag{11b}$$

By adding damping, this mechanical analogue can be a good approximation to (9), but in certain cases the changing geometry might be important; e.g. the modal mass, and forcing amplitude can vary. Furthermore, when using this direct ODE modeling approach it is difficult to assign a proper physical meaning to the mass $m$, and model and material parameters as well as geometrical parameters are not directly available. From a mathematical perspective, the derivation presented here and those given in, e.g., [15] and [16], clarify underlying arguments that justify the reduction from PDE to low-dimensional ODEs.

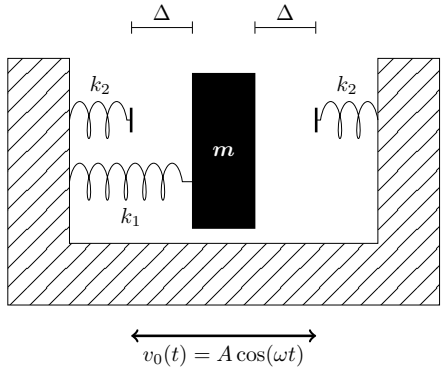


Figure 2: The mass/spring-system that is mechanically equivalent to the cantilever beam system in Figure 1.

The model (10) was derived without any explicit use of specific shape functions nor numerical methods. To keep the derivation simple, we estimate the lowest-resonance frequencies in free flight and in contact in the next section. When comparing the theoretical findings to experimental data, a beam configuration as shown in Figure 3 is used.

## 2.3 Parameter estimation

In free flight, the beam stiffness can be approximated by standard methods: The beam is driven at a frequency close to the first eigenfrequency; in this case the stiffness can be found via the lowest eigenfrequency of system (2) without damping and forcing. We observe that for a single-mode expansion the undamped

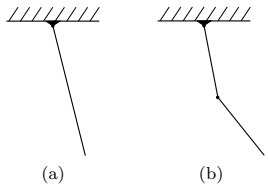


Figure 3: The assumed configuration of the cantilever: Panel (a) shows the one-element configuration in free flight; while Panel (b) shows the two-element configuration in the contact phase.

squared eigenfrequency is approximated via

$$k/m = \frac{EI \int_0^L (\phi'')^2 \mathrm{d}z}{M\phi^2(L_M) + \rho A \int_0^L \phi^2 \mathrm{d}z}\,, \tag{12}$$

where $k/m$ is calculated as $K_{11}/M_{11}$ from (5). Let the beam shape $\phi(z)$ be approximated by the cubic polynomial that solves the static problem, as is illustrated in Figure 4 without the reaction force $R$. The resulting the eigenfrequency is given by

$$f = \frac{1}{2\pi}\sqrt{\frac{k}{m}} \approx 8.4 \text{ Hz}. \tag{13}$$

This frequency deviates by about 10% from the experimentally measured frequency of 7.75 Hz. The estimation method is equivalent to the Rayleigh-Ritz method see, e.g., [19] or, for a more exact approach, [20]; the gain in precision is $< 1\%$.

For vibrations involving contact, the estimation is more difficult due to the amplitude-dependent constraint which results in a nonlinear PDE. However, by assuming that this change in stiffness can be estimated by the static problem through the change in tip stiffness, the problem is linear. The equation that has to be solved is the differential equation for a slender bending beam under the assumption of small displacements (Euler-Bernoulli) and point loads, that is,

$$EIu'''' = 0, \qquad \text{Euler-Bernoulli beam,} \tag{14a}$$
$$u(0) = u'(0) = 0, \qquad \text{clamped end,} \tag{14b}$$
$$u''(L) = 0, \qquad \text{moment free end,} \tag{14c}$$
$$EIu'''(L_i) = R, \quad EIu'''(L) = P, \qquad \text{transverse point forces.} \tag{14d}$$

This linear structural problem is statically indeterminate. The solution can be

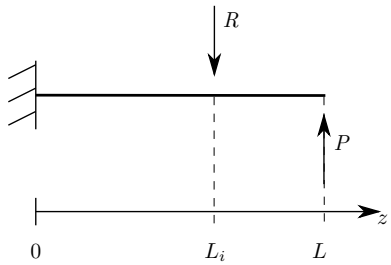


Figure 4: Cantilever beam exposed to transverse point forces $R$ and $P$. The reaction force $R$ acts as the mechanical stop, and $P$ is the point force acting on the mass point.

written as see, e.g., [21]

$$u(\zeta) = u_1(\zeta) + u_2(\zeta), \text{ where } \zeta = \frac{z}{L}, \gamma = \frac{L_i}{L} \text{ and} \tag{15a}$$

$$u_1(\zeta) = \begin{cases} -\frac{RL^3}{6EI}\zeta^2(3\gamma - \zeta), & \zeta \leq \gamma, \\ -\frac{RL^3}{6EI}\gamma^2(3\zeta - \gamma), & 1 \geq \zeta > \gamma, \end{cases} \tag{15b}$$

$$u_2(\zeta) = \frac{PL^3}{6EI}\zeta^2(3 - \zeta), \qquad \zeta \leq 1. \tag{15c}$$

The relative change in tip stiffness is given by $\alpha$, where tip stiffness is defined as

$$k = \left.\frac{\partial P}{\partial u}\right|_{\zeta=1}.$$

When the beam does not touch the mechanical stop the reaction force is zero, i.e., $R = 0$ and, therefore, the tip stiffness is given by

$$k_1 = \left.\frac{\partial P}{\partial u}\right|_{\zeta=1} = \frac{3EI}{L^3} \tag{16}$$

for free flight. When the beam touches the mechanical stop one has to know $R = R(P)$. At the impact, $u(\gamma) = \delta$ and this implies a linear relationship between $P$ and $R$ given by

$$u(\gamma) = \delta = -\frac{RL^3}{3EI}\gamma^3 + \frac{PL^3}{6EI}\gamma^2(3 - \gamma).$$

From this expression it follows that the tip stiffness in the contact phase is

$$k_2 = \left.\frac{\partial P}{\partial u}\right|_{\zeta=1} = \frac{3EI}{L^3}\left(1 - \frac{1}{4}\left(3-\gamma\right)^2\gamma\right)^{-1}. \tag{17}$$

Combining (8b), (16) and (17) leads to

$$\alpha = \left(1 - \frac{1}{4}\left(3-\gamma\right)^2\gamma\right)^{-1} - 1 = \left(1 - \frac{1}{4}\left(3 - \frac{L_i}{L}\right)^2\frac{L_i}{L}\right)^{-1} - 1. \tag{18}$$

It appears that $\alpha \to 0$ for $L_i \to 0$, and $\alpha \to \infty$ for $L_i \to L$. In other words, the change in stiffness vanishes as the mechanical stop is moved towards the clamped end, and it is unbounded as the mechanical stop approaches the free tip. This agrees with the physics of the problem. When the mechanical stop is at the clamped end, it is not going to impact with the beam so the change in tip stiffness vanishes. When the mechanical stop approaches the tip of the beam, it will become harder to move the tip of the beam transversely, to the point where it is not possible to do so as the mechanical stop is blocking any motion of the tip.

Since the damping is chosen proportional to the stiffness (2), the change in damping has the same order of magnitude as $\alpha$. In Table I we see that $\alpha$ deviates by about 20% from the experimentally fitted value.

| | Theory | Experiment |
|---|---|---|
| $f$ | $\sim$ 8.4 Hz | 7.75 Hz |
| $\alpha$ | 4.9 | 5.9 |
| $\xi$ | — | 3 % |
| $\beta$ | $\mathcal{O}(1)$ | 0.885 |

Table I: Stiffness parameters $f$ and $\alpha$, and damping parameters $\xi$ and $\beta$. The parameter $f$ is the natural frequency of the cantilever. Experimental values are model-fitted values.

In summary, the mathematical model (10) has been derived for a clamped beam model with symmetric mechanical stops. The parameters of the model can be split into two main groups as follows:

- Fixed parameters: damping $\xi$ and ratio $\beta$ of damping constants are obtained from experimental data.
- Free parameters: forcing amplitude $I$, frequency $\Omega$, stiffness ratio $\alpha$, and relative forcing amplitude $\nu$.

The damping $\xi$ and the natural frequency $f$ (Table I) in free flight are fitted to the experimental data. The relative stiffness $\alpha$ is considered free, but in the actual experiment it was not changed.

# 3 Smoothing of the piecewise-smooth impact model

In the present case of a cantilever beam with mechanical stops a smooth representation is constructed and analyzed. The smoothing is realized through a nonlinear homotopy or, equivalently, a smooth switching function. To this end, we consider a differentiable nonlinear scalar switching function $\mathrm{H} = \mathrm{H}(\mathbf{x}, p)$ where H converges pointwise to a Heaviside-type step function as $p \to \infty$. Using $\mathbf{x} = (x_1, x_2)^T$, where $x_1 = a$ and $x_2 = \dot{a}$, Equation (10) is reformulated as the first-order system

$$\dot{\mathbf{x}} = \mathrm{f}(\mathbf{x}, t, \boldsymbol{\lambda}) = \begin{cases} \mathrm{f}_1(\mathbf{x}, t, \boldsymbol{\lambda})), & |x_1| \leq 1, \\ \mathrm{f}_2(\mathbf{x}, t, \boldsymbol{\lambda})), & |x_1| > 1, \end{cases} \tag{19}$$

where $\mathrm{f} : \mathbb{R}^2 \times \mathbb{R} \times \mathbb{R}^{k+1} \mapsto \mathbb{R}^2$ is piecewise smooth. The smooth dynamical equivalent is obtained by the following homotopy

$$\dot{\mathbf{x}} = \mathrm{g}(\mathbf{x}, t, \boldsymbol{\lambda}, p) := \mathrm{H}\mathrm{f}_1 + (1 - \mathrm{H})\mathrm{f}_2, \tag{20}$$

so that $\mathrm{g} : \mathbb{R}^2 \times \mathbb{R} \times \mathbb{R}^{k+1} \times \mathbb{R} \mapsto \mathbb{R}^2$ is now a smooth function. This approach has been taken in [22]; see also [23].The choice of $\mathrm{H}(\mathbf{x}, p)$ is a modeling decision and, in general, one can smooth a given sequence of impacts in a piecewise-defined system by smooth functions that approximate the nonsmooth right-hand sides. Well-known examples are the Bump function (compact support) and the hyperbolic tangent function. In general, a piecewise-smoothly defined system has smooth representations given by sums, $\mathrm{g}(\mathbf{x}, \boldsymbol{\lambda}, \mathbf{p}) = \sum_i \mathrm{H}_i(\mathbf{x}, \boldsymbol{\lambda}, p_i)\mathrm{f}_i(\mathbf{x}, \boldsymbol{\lambda})$. Note that the smooth switching functions can also depend on the system parameters and in some cases this might be of interest if, e.g., the natural switching occurs over a predefined range depending on a model-specific geometric parameter. If the smoothing procedure is performed in order to construct a smooth equivalent to the nonsmooth system then a necessary condition is that there exists smoothing homotopy parameter values $p_i^*$ such that the bifurcation diagrams are robust for all $p_i > p_i^*$.

Smoothing processes introduce additional parameters $p_i$ that may effect the solution and bifurcation structure. Hence, it is important to analyse, e.g., how special points depend on the smoothing homotopy parameters and whether they are robust with respect to changes in the parameters $p_i$. In the present case, with one smoothing homotopy parameter $p$, we are interested in quantitative measures, such as the displacement of the cantilever, which should not change for sufficiently large $p$. From the point of view of numerical computations it is not tractable to make $p$ extremely large, because this introduces very large derivatives near the nonsmooth events. Therefore, the strategy is to find a suitable value of $p$ that does not induce artificial and unwanted dynamics or skew the quantitative results in the parameter domains of interest.

We consider the dynamical behavior of the smoothed equivalent of system (10) with parameters $\boldsymbol{\lambda} = (\xi, \beta, \alpha, \Omega, I, \nu)$. Specifically, we consider the cantilever beam with stops

$$\dot{x} = \mathrm{H}\mathrm{f}_1 + (1 - \mathrm{H})\mathrm{f}_2, \tag{21}$$

with

$$\mathrm{f}_1(\mathbf{x}, t, \boldsymbol{\lambda}) = \begin{pmatrix} 0 & 1 \\ -1 & -2\xi \end{pmatrix} \mathbf{x} + I\Omega^2 \cos(\Omega t) \begin{pmatrix} 0 \\ 1 \end{pmatrix},$$

$$\mathrm{f}_2(\mathbf{x}, t, \boldsymbol{\lambda}) = \begin{pmatrix} 0 & 1 \\ -(1+\alpha) & -2\xi(1+\beta) \end{pmatrix} \mathbf{x} + \alpha \begin{pmatrix} 0 \\ \tanh(Kx_1) \end{pmatrix} + I\Omega^2 \cos(\Omega t) \begin{pmatrix} 0 \\ 1+\nu \end{pmatrix},$$

and

$$\mathrm{H}(\mathbf{x}, p) = \left(1 + (x_1^2)^p\right)^{-1}.$$

Our choice of the smooth switching function H is visualized in Figure 5 for several values of $p$. In the present case, the smoothing depends only on the displacement of the beam and the smoothing homotopy parameter $p$. Notice that

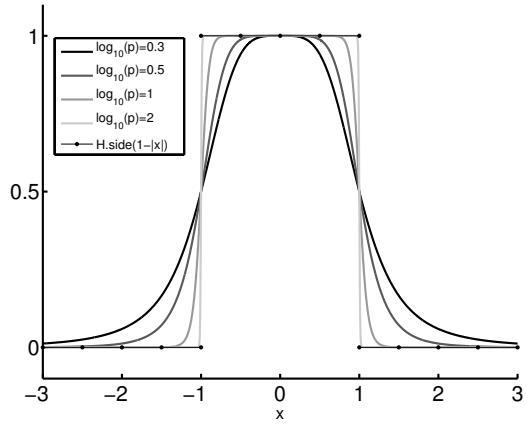


Figure 5: Smooth switching functions $\mathrm{H}(x, p)$ for $\log_{10}(p) \in \{0.3, 0.5, 1, 2\}$ compared to the Heaviside step function Heaviside$(1 - |x|)$.

the definition of $\mathrm{f}_2(\mathbf{x}, t, \boldsymbol{\lambda})$ is modified slightly by approximating the discontinuous sign-function in Equation (10b) with the smooth hyperbolic tangent function. This is a necessary step in order to make the dynamical system smooth. In the nonimpacting region any term in $\mathrm{f}_2(\mathbf{x}, t, \boldsymbol{\lambda})$ is multiplied by the smooth switching term $1 - \mathrm{H}(\mathbf{x}, p)$ which converges to zero pointwise as $p \to \infty$. Therefore, it only matters how well the hyperbolic tangent function approximates the sign-function for $|x| \geq 1$. In Figure 6, the piecewise-constant switching term and $(1 - \mathrm{H}(x, p))\,\mathrm{sgn}(Kx)$ is plotted together with the smooth approximations $(1 - \mathrm{H}(x, p))\tanh(Kx)$ with $\log_{10}(p) = 2$ and $K = 0.5$, $K = 1$, $K = 5$ and

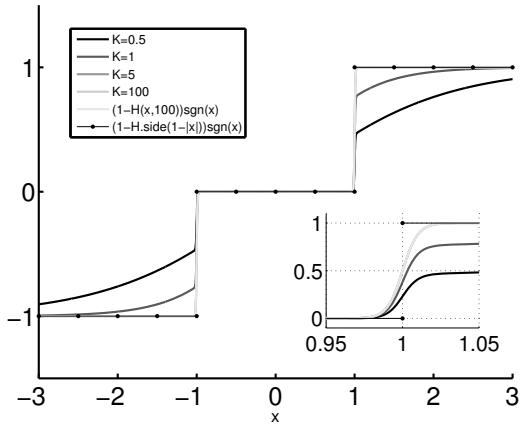


Figure 6: Smooth switching term $(1 - \mathrm{H}(x, p))\tanh(Kx)$ for $p = 100$ and $K \in \{0.5, 1, 5, 100\}$ compared with piecewise-smooth switching functions $(1 - \mathrm{H}(x, 100))\,\mathrm{sgn}(x)$ and $(1 - \mathrm{Heaviside}(1 - |x|))\,\mathrm{sgn}(x)$.

$K = 100$. The smooth approximations are visually indistinguishable for $K = 5$ and $K = 100$; we choose to fix $K = 100$. In the impacting regions the error between the sign-function and the hyperbolic tangent function with $K = 100$ is

$$1 - \tanh(100|x_1|) < 10^{-15} \text{ for } |x_1| > 1.$$

Since the local variations are below the numerical tolerances, we can conclude that further investigations of the dependence of the smoothing on the smoothing parameter $K$ is not necessary.

# 4 Numerical bifurcation analysis

In this section we investigate the dynamical behavior of the smooth system using the numerical continuation and bifurcation analysis package AUTO [24]. We continue periodic orbits in one and two parameters of the smooth system (21) at the 1:1 resonance. As mentioned earlier, the mechanical system is, a harmonically-driven single-degree-of-freedom nonlinear oscillator for which the nonlinearity is hardening, because the effective beam stiffness is larger in the contact phase. When such a system is driven with a large enough forcing amplitude near its natural frequency (eigenfrequency) the usual response is a nonlinear resonance peak. Figure 7 shows one of the nonlinear resonance peaks, where $\Omega$ denotes the scaled forcing frequency and $||x_1||_\infty$ denotes the maximal displacement amplitude of the periodic orbits. Stable and unstable branches are

indicated by solid and dashed lines, respectively. For a range of frequencies, we have a bistable system with three coexisting periodic orbits, two stable orbits separated by an unstable orbit. There are two bifurcation points marked by the two grey bullets, which are fold points (limit point/saddle point/turning point). Together, the fold points organize a hysteresis loop that determines the possible behavior of the system when keeping all parameters fixed except for the forcing frequency. Starting with a relatively large forcing frequency, the system stabilizes to a solution on the lower branch. Continuously decreasing the forcing frequency causes a discontinuous (increase) jump in the response amplitudes when reaching the left-most fold point. Similarly, starting from a relatively small forcing frequency, and continuously increasing the driving frequency results in a discontinuous (decrease) jump in response amplitude when passing the right fold point on the upper stable branch.

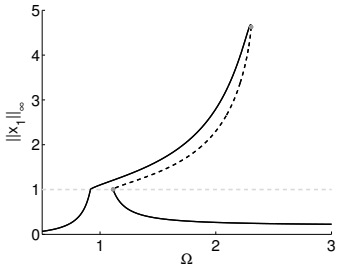


Figure 7: Nonlinear frequency response diagram of system (21) with $\nu = 0$, $\alpha = 5.9$ and $\log_{10}(p) = 2$. Stable branches are solid, unstable branches are dashed and the two fold points are marked with grey bullets. The other parameters are $(\xi, \beta, I) = (0.03, 0.885, 0.2)$.

In Section 4.1 we investigate the behavior of the system without considering a change in the forcing amplitude at the mechanical stop, i.e., for $\nu = 0$. In Section 4.2 the case of doubling the forcing amplitude in the contact phase is considered, i.e., we set $\nu = 1$. In this case, the system has two additional fold points and the bifurcation diagram exhibits an isola of periodic solutions that is not connected to the main solution branch. In what follows we neglect the discontinuous damping terms when the regularity is stated, this is motivated by the fact that the damping is orders of magnitude smaller than all other terms.

## 4.1 Continuous forcing amplitude

First we consider the case of a continuous forcing amplitude, i.e., $\nu = 0$, so that system (10) is Lipschitz continuous. Moreover, we choose a moderately stiff impact using an intermediate value of $\alpha = 5.9$. Based on Equation (18), $\alpha = 5.9$

geometrically corresponds to a placement of the mechanical stops at 3/5-length of the beam (from the clamped end $z = 0$). Figure 8(a) shows the corresponding one-parameter bifurcation diagram; as in Figure 7, $||x_1||_\infty$ denotes the maximal amplitude of the periodic orbits and the bifurcation parameter is the scaled frequency $\Omega$. At first sight, the bifurcation diagram shows a typical nonlinear resonance like the one shown in Figure 7. However, two additional very localized folds are robustly present on the upper branch; see the enlargement in Figure 8(a). Since we are smoothing a piecewise-smooth system, we also investigate how the bifurcation diagram depends on the smoothing homotopy parameter $p$. To this end, we follow the loci of all four fold points in two parameters. Figure 8(b) shows the bifurcation diagram projected onto the $(\log_{10}(p), \Omega)$-parameter plane. The two upper fold points are robust, in the sense that they are practically independent of $p$ as $p \to \infty$, while the two lower fold points disappear in a cusp for $\log_{10}(p) \approx 1.5$. Hence, for $p$ large enough, the smoothed system exhibits the same expected bifurcation structure as system (10). We conclude that, with a Lipschitz-continuous vector field for $\nu = 0$, the smoothed system shares the same bifurcation structure as the Duffing oscillator near resonance, because the two localized fold points on the left of the resonance are induced by the smoothing. In another setting, it may be advantageous to create this smoothing effect deliberately by design; however, for the mechanical system under consideration here, this is unwanted behavior.

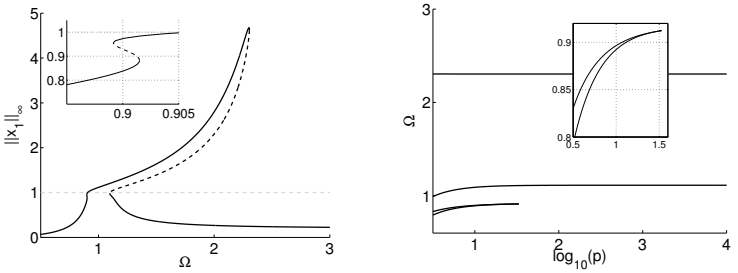


Figure 8: System (21) with $\nu = 0$ and $\alpha = 5.9$; Panel (a) shows the frequency response diagram for $\log_{10}(p) \approx 1.1$; Panel (b) shows the loci of fold points in the $(\log_{10}(p), \Omega)$-plane. The remaining parameter set is $(\xi, \beta, I) = (0.03, 0.885, 0.2)$.

For $\alpha = 10$, still with $\nu = 0$, the change in stiffness is almost twice as large as for $\alpha = 5.9$. Based on Equation (18), $\alpha = 10$ geometrically corresponds to a placement of the mechanical stops at 2/3-length of the beam (from the clamped end $z = 0$). There is no qualitative difference between Figures 8 and 9. Note from the enlargements that the two localized fold points are both below

threshold of the mechanical stop; this indicates that they are induced by the smoothing, since the piecewise-smooth system is linear if the mechanical stops are not impacted upon, i.e., for solutions with $||x||_\infty < 1$.

The additional fold points emerge, because the smooth switching is not sufficiently localized. Consequently, the restoration force features a softening effect that is unphysical. For each given $\alpha$ there is a suitable choice of $p$, but as $\alpha$ is increased, the smoothing must be more localized, i.e., $p$ must be increased. If $p$ is not sufficiently large the softening effect becomes more pronounced, and in the present case this is the sole mechanism for the observed smoothing-induced bifurcations; softening and hardening effects are explained, e.g., in [25] and [26]. Figure 10 illustrates how, for small $p$, the smooth approximations of the piecewise-linear elastic restoring force and/or its derivative dips (i.e., spring softens) in a neighborhood of $x = 1$. In Figure 9b the fold points are continued in $(\log_{10}(p), \Omega)$. It is observed that they disappear in a cusp for $\log_{10}(p) \approx 2$, hence, the smoothing should be chosen such that $\log_{10}(p) > 2$.

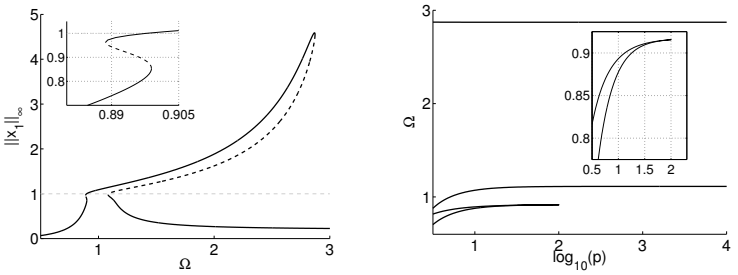


Figure 9: System (21) with $\nu = 0$ and $\alpha = 10$; Panel (a) shows the frequency response diagram for $\log_{10}(p) \approx 1.1$; Panel (b) shows the loci of fold points in the $(\log_{10}(p), \Omega)$-plane. The remaining parameter set is $(\xi, \beta, I) = (0.03, 1.5, 0.2)$.

## 4.2 Discontinuous forcing amplitude

We next consider the case where the the forcing amplitude is such that system (10) is discontinuous, by setting $\nu = 1$. We first set $\alpha = 5.9$, so that the cantilever is undergoing moderately stiff impacts. These parameter values will also be used when the system is compared with experimental data in Section 5. Figure 11(a) shows that, for $\nu = 1$, two fold points are again introduced in the same region as in Figure 8(a) and the qualitative structure is the same. However, these fold points are not induced by the smoothing process. This is illustrated by the two-parameter bifurcation diagram in Figure 11(b), which

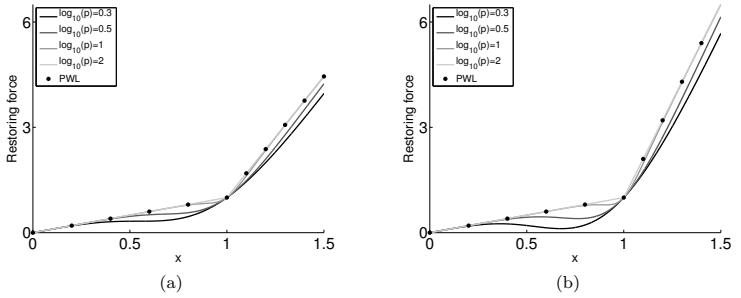


Figure 10: Elastic restoring force as a function of transverse displacement. Panel (a) shows the moderate impact, $\alpha = 5.9$. Panel (b) shows the hard impact $\alpha = 10$. The legends refer to different smoothing levels of the piecewise-linear force, i.e., different $p$. PWL denotes the piecewise-linear force.

shows that the two additional fold points do not disappear in a cusp as $p$ is increased. For this particular parameter set there are four limit points for any $p$.

As was mentioned earlier, it may be of interest to include dependencies of model parameters in the smoothing functions. For example, the smooth switching functions generally depend on model parameters, i.e., $p = \Theta(\lambda)$ where $\Theta$ is designed by a-priori model properties or from numerical continuation results. Our analysis shows that the smooth switching must be scaled according to the stiffness ratio $\alpha$, i.e., $p = \Theta(\alpha)$; however, since the experimental data is for fixed $\alpha$, we need not construct $\Theta(\alpha)$ explicitly for more values of $\alpha$ than are already investigated. We mention here the modeling and analysis of the dynamics of the main landing gear on a plane [27], where such a smoothing dependence is analyzed further, because, in that case, the smooth switching function naturally depends on an active bifurcation parameter.

In addition to the difference in the number of fold points between the case of continuous vs. discontinuous forcing amplitude the latter exhibits an isola of periodic solutions for all sections in a small range of the rescaled forcing amplitude $I_l = \frac{d}{m}\frac{A}{\Delta_l}$; where $\Delta_l$ denotes the displacement of the end-point of the beam when the beam touches the mechanical stops. This isola is not connected to the main solution branch. The structure of the branching process of the isola is shown in Figure 12; where Figure 12(a) is a projection of the fold point curve that connects the two right-most fold points in the sections showing the nonlinear resonance tongue, e.g., Figure 11(a). Note that the fold point curve that connects the two left-most fold points is not present because the forcing amplitude is to small. The horizontal lines are the sections which are shown

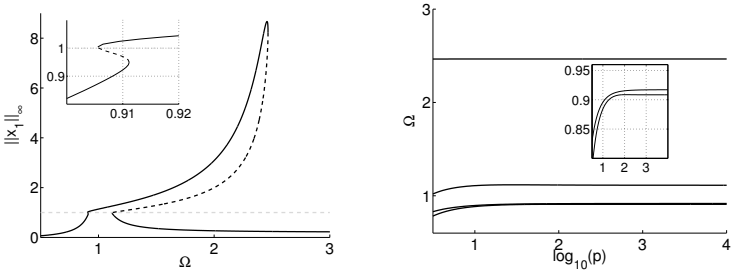


Figure 11: System (21) with $\nu = 1$ and $\alpha = 5.9$. Panel (a) shows the frequency response diagram for $\log_{10}(p) = 1.5$. Panel (b) shows the loci of fold points in the $(\log_{10}(p), \Omega)$-parameter plane; all four branches are disconnected. The remaining parameter set is $(\xi, \beta, I) = (0.03, 0.885, 0.2)$.

in Figures 12(b)–12(d) and combined they illustrate structure of the isola. In Figure 12(b) the section with $I_l = 0.0463$ is shown and it is readily observed that the frequency response exhibits only the main solution branch for the system (21) with no impacting solutions, i.e., a linear resonance peak as a result of weak forcing; in Figure 12(c) the section with $I_l = 0.0475$ is shown and an isola of periodic solutions appears; increasing the forcing amplitude to $I_l = 0.0487$ and the isola has reconnected to the main solution branch. In the present case the isola is caused by the discontinuous change in forcing amplitude. In Figure 13(a) a global two-parameter bifurcation diagram is shown, this will be explained in detail in Section 5.

# 5 Comparison with experiments

The experimental data is adapted from [10], where experimental continuation is performed for an impacting beam experiment. A cantilever beam of length 0.161 m with end mass 0.2116 kg is periodically excited by a shaker and allowed to hit stops at 0.71 m with a gap between cantilever and stops of $10^{-3}$ m (cf. Figure 1). The data set was obtained via frequency sweeps with constant gains of the shaker. As a result the amplitudes of the excitation are not constant along the constant-gain sweeps conducted in the experiment. We transformed this data set for comparison with the numerical findings of the model (21). The non-constant forcing amplitudes during sweeps prohibit conclusive evidence of the presence of isolas in the experiment, as observed in the model; the necessary information is simply not contained in this data set. The coupling of the shaker to the mechanical structure resulted in some cases in forced excitations that

are not perfect harmonics. This could be the reason why, in the experimental data the cusp point also comes earlier than in the model. We now consider system (21) with $\xi, \beta, \alpha, \nu$ and $p$ are fixed, while $I_l$ and $\Omega$ are free parameters. The values used are $\xi = 0.03, \beta = 0.885, \alpha = 5.9, \nu = 1$ and $p = 10^2$. The experimentally fitted value of the change in forcing amplitude was found to be $\nu = 1$, even though the theoretical predictions indicate that $\nu$ should be of higher order and, therefore, negligible.

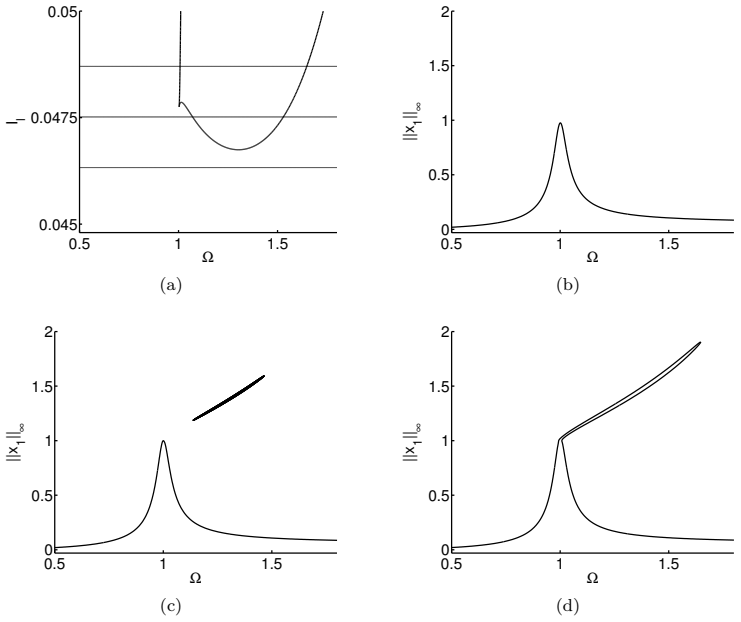


Figure 12: The solid curve in Panel (a) is a projection of the loci of fold points, while the three horizontal lines correspond to the sections for $I_l \in \{0.0463, 0.0475, 0.0487\}$, which are shown in Panels (b)–(d), respectively. Panel (b) shows the frequency response of $I_l = 0.0463$; panel (c) shows the isola for the frequency response of $I_l = 0.0475$; panel (d) shows the frequency response of $I_l = 0.0487$. The remaining parameter set is $(\xi, \beta) = (0.03, 0.885)$.

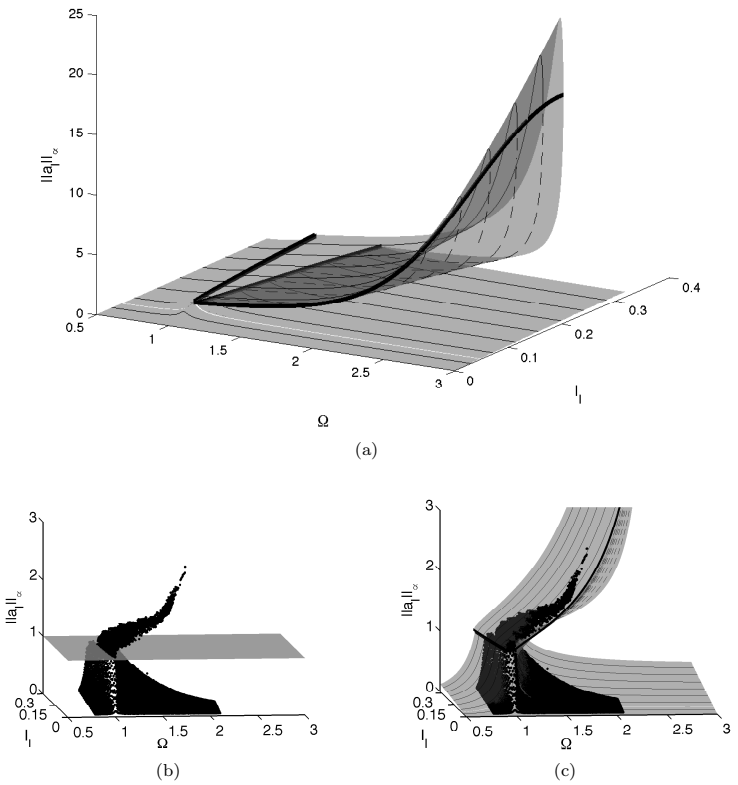


Figure 13: Panel (a) shows the global bifurcation structure of the 1:1 resonance tongue in two parameters, namely, driving force amplitude $I_l$ and driving frequency $\Omega$. The thin curves will be used for experimental comparison. The solid black curves represent the loci of fold points. Panel (b) shows the experimental data plotted against the surface indicating the mechanical stops. Panel (c) shows the smooth model (21) with the experimental data adapted from [10].

We are interested in how the loci of fold points depend on driving frequency $\Omega$ and the rescaled forcing amplitude $I_l$. From now on we also consider a rescaling of the displacement of the end point of the beam by $\Delta_l$; this is denoted by $a_l$ and $||a_l|_\infty$ is the maximal displacement amplitude of the periodic solutions. The scaling is introduced because the laser in the experiment measures the displacement at a certain distance below the lumped mass and for experimental comparison $a_l$ is adjusted accordingly using the beam configuration in Figure 3 and assuming small displacements; this transformation has no effect on qualitative measures. The global two-parameter bifurcation diagram is shown in Figure 13(a); here we see how the resonance tongue is bending over due to the mechanical stops and the nonlinearity they induce. In the diagram there are two solid black curves, separated via the plane section given by $\{(\Omega, I_l, ||a_l||_\infty) : \Omega = 1\}$, and these are the loci of fold points and both of the curves loop back over themselves in a cusp in the projection onto the $(\Omega; I_l)$-parameter plane. The range over which the isola exists is visualized by cutting the manifold in two pieces leaving out the sections with the isola. This isola is very thin and can not be observed in the experimental data. The thin solid/dashed curves are used for experimental comparison later.

The experimental data set is shown in Figure 13(b) with the mechanical stop indicated by the transparent surface, and we can clearly see the match of the resonance tongue bending over due to the mechanical stops. Figure 13(c) shows an enlargement of the continuation results from the smooth system (21) in $(\Omega, I_l, ||a_l||_\infty)$ together with the experimental data. It is difficult to asses the quantitative agreement between the model and experiments because the data is scattered and the density of measurements varies nonuniformly. Therefore, all experimental comparison is done via sections of constant forcing shown in Figure 14.

Figure 14(a) shows the section for $I_l \approx 0.03$. The model predicts low-amplitude nonimpacting solutions for this value of (scaled) forcing amplitude, but the experimental data is showing impacting solutions. This indicates that the cusp point or grazing point is not predicted perfectly. From the figure it looks as if the experimental data indicates an isola as well. As mentioned earlier, it is not possible to conclude if this is indeed the case because the experimental sweeps were conducted with constant gain of the shaker. Furthermore, for small-amplitude forcing the noise levels might not be negligible.

Figure 14(b) shows the section for $I_l \approx 0.07$. For this value of the forcing amplitude the quantitative agreement of both upper and lower branches is very good. It is worth noting that, for orbits close to the mechanical stops, there is, in some of the figures, a small indication of clustering points. They could be ascribed to the fact that experimental measurements naturally show some fluctuations in regions where noise levels are comparable to the distance from the mechanical stops, and grazing orbits are particularly vulnerable to this effect.

Figures 14(c) and 14(d) show the sections for $I_l \approx 0.11$ and $I_l \approx 0.16$, respectively. Again, the quantitative agreement of both upper and lower branches is very good. From the enlargement it is seen that the width of the 'linear' resonance in the model is not in exact agreement, with the experimental data,

and the upper branch is slightly overestimated. The reasons for these small discrepancies could be the choice of damping model or damping parameters, which are phenomenological.

In Figures 14(e) and 14(f) sections are shown with $I_l \approx 0.20$ and $I_l \approx 0.24$, respectively. For these values of the forcing amplitude, the quantitative agreement is less good; in particular, the effect of overestimating the upper branches is slightly more pronounced, but it should be noted that the absolute errors are $< 1\,\mathrm{mm}$. Furthermore, from the enlargements it can also be observed that the fold points of the lower branches are not sharply defined for these large forcing amplitudes.

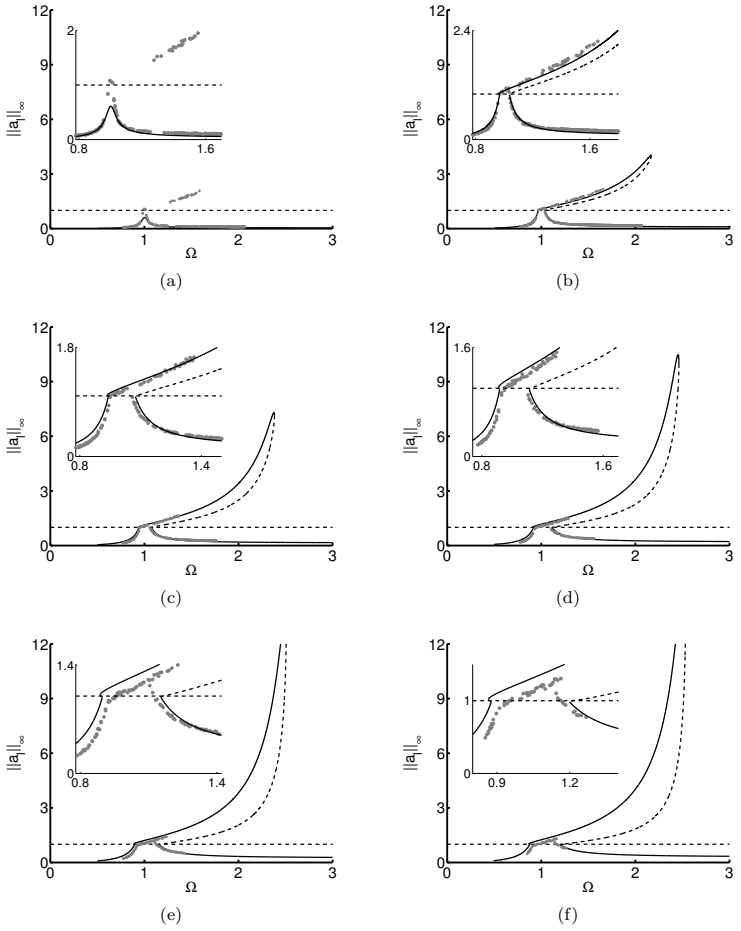


Figure 14: Panels (a)-(f) shows the comparison of the smooth model (21) with the experimental data set. Each plot represents one of the thin solid/dashed curve sections in Figure 13. The smoothing homotopy parameter is $p = 100$ and $I_l$ takes the values 0.03, 0.07, 0.11, 0.16, 0.20 and 0.24, respectively. The solid/dashed curve represents the continuation results of (21) and the grey bullets are the scattered point set from the experimental data. The enlargements are for proper visual comparison in the regions with experimental data.

The correspondence between the experimental data and the mathematical model also depends on the ambiguous choice of the ratio $\frac{m}{d}$ for the rescaling $I_l = \frac{d}{m}\frac{A}{\Delta_l}$. In these calculations $m/d = 2/3$ was used and the measured distance $\delta$ in Figure 1 is corrected to fit by setting $\delta = 0.85 \cdot 10^{-3}\,\mathrm{m}$. Furthermore, it is to be expected that the model validity is restricted to small-amplitude displacement, because for larger displacement amplitudes the beam should be treated as a nonlinear elastica.

It would have been desirable to investigate whether or not the two limit points before the first linear resonance exist in the experiment or not. Unfortunately, this is not feasible, because these two points lie at a distance below the noise level of the experiment.

# 6 Discussions and conclusions

In this paper a single-degree-of-freedom model of a cantilever beam with symmetric mechanical stops and a mass attached was derived. Model parameters were estimated from first principles and compared to experimentally fitted values. These comparisons are given in Table I and it should be remarked that the nonlinear stiffness ratio $\alpha$ is quite well approximated. The model is particularly suited for small-amplitude solutions, for which it predicts the experimental data very well.

In contrast to the more traditional setting where mechanical systems with impacts are realized by nonsmooth models, the present paper dealt with the setting in which the impact model is described with a smooth model. To obtain this model a smooth switching (nonlinear homotopy) was applied. The smoothing procedure was investigated by means of numerical bifurcation analysis. It was investigated when and how the bifurcation structure was affected by the smoothing. The investigation showed that, as the smoothing function approaches the Heaviside function, the bifurcation diagram becomes practically independent of the smoothing homotopy parameter. This investigation was performed for moderate impacts, hard impacts and discontinuous forcing amplitudes. The mechanism for the smoothing-induced bifurcations was also identified, and it was shown that the suitable smoothing homotopy parameter depends on the stiffness ratio, i.e., $p = \Theta(\alpha)$; specifically, increasing $\alpha$ implies increasing $p$. With this in mind, it may be noted that the smoothing process can cause numerical difficulties as $\alpha$ becomes very large, because then $p$ must be very large. In such cases it may be beneficial to perform multisegment numerical continuation of the nonsmooth system.

The behavior of the smooth model was compared with the experimental data [10]. The qualitative structure was verified within the range of the data set. The quantitative comparison was good overall, with a tendency to overestimate the upper branch as the forcing amplitudes becomes large. The results in the paper demonstrate that a smooth single-degree-of-freedom model describes the experimental behavior very well and that high-dimensional FE models are not always necessary to obtain predictions of good quantitative quality.

For future work it is interesting to test the model in a larger parameter regime to explore its limits. Specifically it would be interesting to investigate other parameter regimes of excitation frequency and amplitude. Since a posteriori fitting was kept to a minimum, it could also be interesting to find an optimal fit in a reasonable parameter-neighborhood, now that model parameters have been determined with mechanical interpretations and proper magnitudes.

## Acknowledgements

ME thanks the Department of Mathematics at *The University of Auckland* for its kind hospitality and the Idella Fondation for financial support. JS and JJT acknowledge funding from the Danish Research Council FTP under the project number 09-065890/FTP. The authors thank Emil Bureau, Frank Schilder and Ilmar Santos for fruitful discussions and for providing the data from [10].

## References

[1] V. I. Babitsky. *Theory of Vibro-Impact Systems and Applications*. Springer-Verlag, Berlin, 1998.

[2] R. Burton. *Vibration and Impact*. Dover, Publications, New York, 1968.

[3] A. E. Kobrinskii. *Dynamics of Mechanisms with Elastic Connections and Impact Systems*. Iliffe Books, London, 1969.

[4] R.A. Ibrahim. Friction-induced vibration, chatter, squeal, and chaos: part i mechanics of friction. *In: Friction-induced vibration, chatter, squeal, and chaos, ASME DE-Vol 49, 107121*, 1992.

[5] R.A. Ibrahim. Friction-induced vibration, chatter, squeal, and chaos: part ii - dynamics and modeling. *In: Friction-induced vibration, chatter, squeal, and chaos, ASME DE-Vol 49, 123-138*, 1992.

[6] R. I. Leine and H. Nijmeijer. *Dynamics and Bifurcations of Non-Smooth Mechanical Systems*. Springer-Verlag, Berlin Heidelberg, 2004.

[7] J. J. Thomsen and A. Fidlin. Near-elastic vibro-impact analysis by discontinuous transformations and averaging. *Journal of Sound and Vibration 311(1-2), 386-407*, 2008.

[8] M. Bernardo, C. Budd, A.R. Champneys, and P. Kowalczyk. *Piecewise-smooth dynamical systems: theory and applications*, volume 163. Springer, 2007.

[9] V. Acary and B. Brogliato. *Numerical Methods for Nonsmooth Dynamical Systems - Applications in Mechanics and Electronics*. Springer-Verlag, Heidelberg, 2008.

[10] E. Bureau, F. Schilder, I.F. Santos, J.J. Thomsen, and J. Starke. Experimental bifurcation analysis of an impact oscillator – tuning a non-invasive control scheme. *Journal of Sound and Vibration*, 2013.

[11] J. Sieber and B. Krauskopf. Control based bifurcation analysis for experiments. *Nonlinear Dynamics*, 51(3):365–377, 2008.

[12] J. Sieber, A. Gonzalez-Buelga, S.A. Neild, D.J. Wagg, and B. Krauskopf. Experimental continuation of periodic orbits through a fold. *Phys. Rev. Lett. (USA)*, 100(24):244101–1–4, 2008.

[13] D. Barton and S.G. Burrow. Numerical continuation in a physical experiment: Investigation of a nonlinear energy harvester. *J. Comput. Nonlinear Dyn. (USA)*, 6(1):–, 2011.

[14] D. Barton, B.P. Mann, and S.G. Burrow. Control-based continuation for investigating nonlinear experiments. *Journal of Vibration and Control*, 18(4):509–520, 2012.

[15] F. C. Moon and S. W. Shaw. Chaotic vibrations of a beam with non-linear boundary-conditions. *International Journal of Non-linear Mechanics*, 18(6):465–477, 1983.

[16] S. W. Shaw. Forced vibrations of a beam with one-sided amplitude constraint - theory and experiment. *Journal of Sound and Vibration*, 99(2):199–212, 1985.

[17] L.D. Landau and E.M. Lifshitz. *Course of Theoretical Physics vol. 7: Theory of elasticity*. Butterworth-Heinemann, Oxford England Burlington, MA, 1986.

[18] J.J. Thomsen. *Vibrations and Stability: Advanced Theory, Analysis, and Tools*. Springer, Berlin, 2003.

[19] R. Courant and D. Hilbert. *Methods of Mathematical Physics*, volume 1. Interscience Publishers, Inc., New York, NY, 1953.

[20] L. Meirovitch. *Fundamentals of Vibrations*. McGraw-Hill, Boston, 2001.

[21] J.M. Ger and S.P. Timoshenko. *Mechanics of Materials*. PWS Publishing Company, Boston, 1997.

[22] R. Szalai and H. M. Osinga. Arnol'd tongues arising from a grazing-sliding bifurcation. *Siam Journal on Applied Dynamical Systems*, 8(4):1434–1461, 2009.

[23] Yu.A. Kuznetsov, S. Rinaldi, and A. Gragnani. One-parameter bifurcations in planar filippov systems. *Int. J. Bifurcation Chaos Appl. Sci. Eng. (Singapore)*, 13(8):2157–2188, 2003.

[24] E. J. Doedel with major contributions from A.R. Champneys, T. Fairgrieve, Yu.A. Kuznetsov, B. Oldeman, R. Paffenroth, B. Sandstede, X. Wang, and C. Zhang. *AUTO-07P : Continuation and bifurcation software for ordinary differential equations*. Concordia University Montreal, Canada.

[25] J.K. Hale. *Ordinary Differential Equations*. Wiley, New York, 1969.

[26] A.H. Nayfeh and B. Balachandran. *Applied Nonlinear Dynamics. Analytical, Computational, and Experimental Methods*. Wiley, New York, 1995.

[27] C. Howcroft, B. Krauskopf, M.H. Lowenberg, and S.A. Neild. Influence of variable side-stay geometry on the shimmy dynamics of an aircraft dual-wheel main landing gear. *SIAM J. Appl. Dyn. Syst.*, 12-3:1181–1209, 2013.

Appendix B

# Experimental Bifurcation Analysis of an Impact Oscillator - Determining Stability

# Experimental Bifurcation Analysis of an Impact Oscillator - Determining Stability

Emil Bureau[a,*], Frank Schilder[b], Michael Elmegård[b], Ilmar F. Santos[a], Jon J. Thomsen[a], Jens Starke[b]

[a]*Department of Mechanical Engineering, Technical University of Denmark*
[b]*Department of Applied Mathematics and Computer Science, Technical University of Denmark*

**Abstract**

We propose and investigate three different methods for assessing stability of dynamical equilibrium states during experimental bifurcation analysis, using a control-based continuation method. The idea is to modify or turn off the control at an equilibrium state and study the resulting behavior. As a proof of concept the three methods are successfully implemented and tested for a harmonically forced impact oscillator with a hardening spring nonlinearity, and controlled by electromagnetic actuators. We show that under certain conditions it is possible to quantify the instability in terms of finite-time Lyapunov exponents. As a special case we study an isolated branch in the bifurcation diagram brought into existence by a 1:3 subharmonic resonance. On this isola it is only possible to determine stability using one of the three methods, which is due to the fact that only this method guarantees that the equilibrium state can be restored after measuring stability.

*Keywords:* Control-based Continuation, Experimental Bifurcation Analysis, Impact Oscillator, Electromagnetic Actuators, Determining Stability, Finite-Time Lyapunov Exponent (FTLE)

## 1. Introduction

We propose and test different strategies for experimentally determining the stability of dynamical equilibrium states (here periodic orbits with stationary amplitude) that can be applied when conducting experimental bifurcation analysis using a control-based continuation method. Control-based continuation [1, 2, 3, 4, 5, 6] is a technique that allows path following of stable as well as unstable dynamical equilibrium states under variation of system parameters, i.e. it enables investigations of the type shown in Figure 1. The method utilizes a non-invasive stabilizing control, which locally turns both stable and unstable equilibrium states into asymptotically stable ones. A consequence of adding control is that investigating the Jacobian or fitting a simple model to judge the stability of the system will yield information about the artificially stabilized system rather than the underlying uncontrolled system.

Following Lyapunov's idea of defining stability, we show how it is possible to assess the stability by modifying or turning off the control signal for a certain amount of time, and study the resulting behavior of the system. As a result it is possible to experimentally obtain bifurcation diagrams with indication of the stability of individual branches as well as locating the bifurcation points where the stability changes, cf. Figur 1. Under certain conditions it is possible to quantify the rate of divergence from an unstable state in terms of the finite-time Lyapunov exponent (FTLE). Depending on the type of system, it may be unacceptable to allow unbounded divergence from an unstable equilibrium: The divergence must not alter the system and the control must be able to restore the equilibrium state after the stability check. We show how it is possible to assess the stability of an equilibrium state while only allowing a limited divergence. Details on the experimental test rig (cf. Figure 2) and the implementation of the control-based continuation method are given in [6], while here we propose and test new methods for determining stability.

*Corresponding author. TEL: +45 2843 5906.
*Email address:* embu@mek.dtu.dk (Emil Bureau)

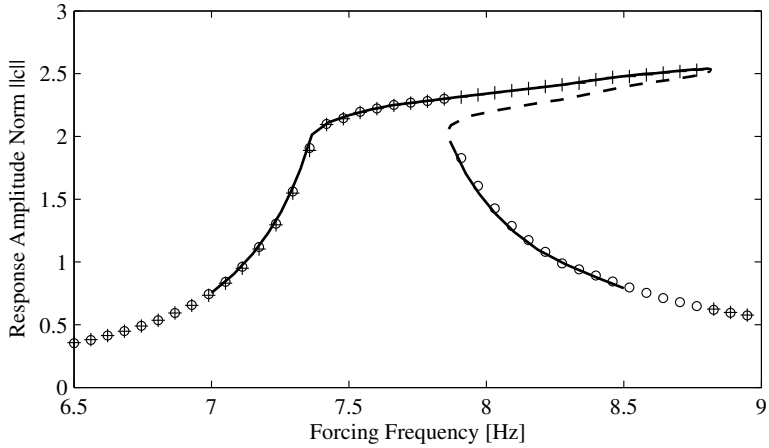


Figure 1: Experimental frequency response of a harmonically forced nonlinear impact oscillator obtained by parameter sweep and control-based continuation. Response from traditional frequency sweeps is denoted by (+) for increasing and (∘) for decreasing frequency. Response obtained by control-based continuation is denoted by (—) for stable part and (– – –) for unstable part.

## 2. Experimental Setup

The experimental test rig is shown in Figure 2; it comprises a harmonically forced impact oscillator with electromagnetic actuators. The impactor is a flexible beam with a tip mounted mass. The beam will impact the mechanical stops when the vibration amplitude exceeds the gap size. This impact causes an increased stiffness which results in highly nonlinear responses for certain ranges of forcing parameters, see Figure 1. Electromagnetic actuators mounted on each side of the impactor mass are used to generate a non-invasive control force $u$ necessary for the control-based continuation. The direction of the generated force is dependent on the sign of the control signal. Two laser sensors are used to measure the relative displacement of the impactor mass, which is used for characterizing the current state of the experiment $x$. Note that several internal scalings are used in the continuation code, which means that the presented measured quantities are non-dimensionalized. The response amplitude of the impactor is measured using the norm:

$$\|c\| := \sqrt{\sum_{i=0}^{2*Q} c_i^2}, \tag{1}$$

where the $c_i$ are the Fourier components and $Q$ denotes the number of Fourier modes used, in our experiment usually $Q = 5$. All results and plots presented throughout the paper are experimental measurements made using the test rig.

## 3. Suggestion of three methods for assessing stability in experiments

Control-based continuation employs a path following algorithm that tracks branches of stable and unstable equilibrium under the variation of system parameters. It works by iterating a series of prediction and correction steps: First a prediction step is made in the tangent direction of the equilibrium branch, and then this prediction is corrected orthogonally back onto the branch using a root finding algorithm [7]. Since we are continuing dynamical equilibrium states, the predicted and current state are expressed in terms of a predicted reference trajectory $y(t)$ defined by the discrete points $y_j = y(t_j), t_j = t_0 + j\Delta t, j = 0, 1, \ldots, n$ and a measured state $x(t)$ defined by the sampled points $x_j = x(t_j)$,

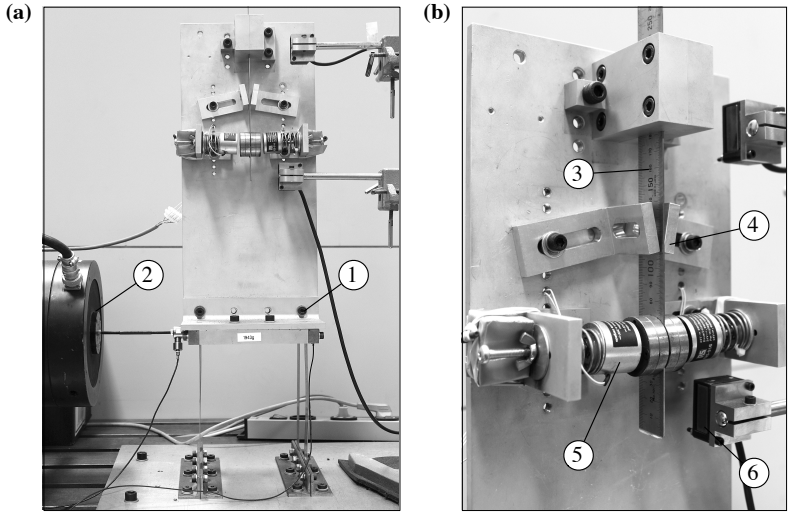


Figure 2: The experimental test rig: A harmonically forced impact oscillator with electromagnetic actuators. (a) Front view of the full test rig. (b) Impactor side view. The test rig consists of (1) a platform with flexible legs, which allows movement only in the forced direction; (2) an electromagnetic shaker to apply a harmonic force to the platform; (3) flexible beam with tip mass; (4) adjustable mechanical stops, which will cause impacts and increased stiffness when the vibration amplitude of the beam exceeds the gap size; (5) electromagnetic actuators which can exert a control force directly on the tip mass; (6) laser displacement sensors. Further details can be found in [6].

where $\Delta t = 1/f_s$ is the sampling interval and $f_s$ the sampling frequency. The predicted state $y(t)$ is artificially created and stabilized by a non-invasive proportional derivative (PD) control:

$$u(t) = PD(x(t) - y(t)) := K_p(x(t) - y(t)) + K_d(\dot{x}(t) - \dot{y}(t)), \tag{2}$$

where $K_p$ and $K_d$ denote proportional and derivative gain, respectively.

The corrector keeps changing the reference state $y$ until the predicted and measured state are close to identical $x - y \approx 0$, at which point the periodic contribution from control effectively vanishes ($u \approx 0$). The measured state $x$ is accepted as a stable or unstable equilibrium state of the underlying uncontrolled system, and the control is only activated if the measured state $x$ diverges from the reference state $y$. A bifurcation diagram (cf. Figure 3) consists of a number of such successful continuation steps. At each accepted state we wish to determine and possibly quantify the stability.

To determine stability information, we implement and test three simple ideas based on modifying or turning off the control, while observing the resulting behavior of the system. In theory nothing happens when turning off the control at a stable state, as long as turning off the control does not cause a perturbation of the system. Due to the fact that an experiment will have noise in both measurements and control, the continuation algorithm accepts a measured state $x$ as an equilibrium state of the underlying uncontrolled system within some tolerance. Therefore, one must expect a small residual drift when turning off the control at a stable state. The stability tests presented here all require the tolerance with which the corrector accepts a state $x$ as an equilibrium state to be sufficiently strict.

When turning off the control at an unstable equilibrium state, the current state $x$ starts to diverge from the reference state $y$, cf. Figure 4. Branches of unstable equilibrium states act as seperatrices in the bifurcation diagram, so depending on the initial conditions given when turning off the control, the state will diverge and settle onto another stable state; in our system either a higher or a lower amplitude stable equilibrium state, cf. Figure 3. If the noise in the experiment is very low, it might be necessary to introduce a small in-phase perturbation in order to facilitate the divergence, but in our case the imperfections in the experiment make this unnecessary. In [6] it is explained how to implement such an in-phase perturbation and an in depth investigation of the effects of turning off the control at stable and unstable states is presented in [8].

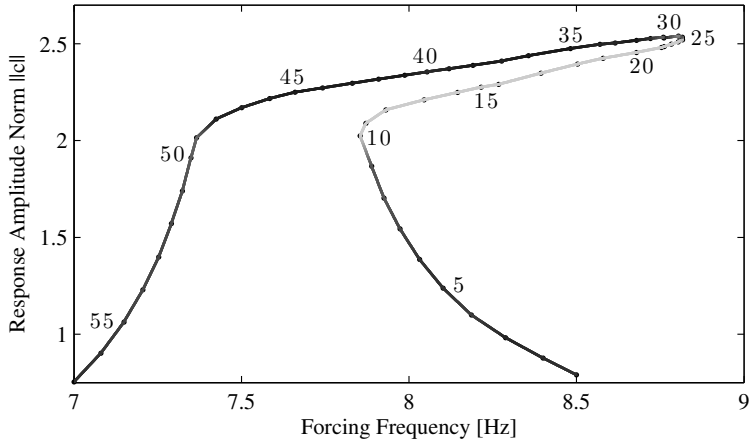


Figure 3: Bifurcation diagram with a continuous measure of stability plotted in grayscale (interpolated in between measurement points): Dark tones denote a small stability estimator and hence a stable state. Lighter tones denote a large stability estimator and hence an unstable state. All measurement points are marked with $(\cdot)$ and consecutively number labeled (shown for every fifth point). These labels will be used to identify different equilibrium states and will be referred to with # and label number throughout the paper.

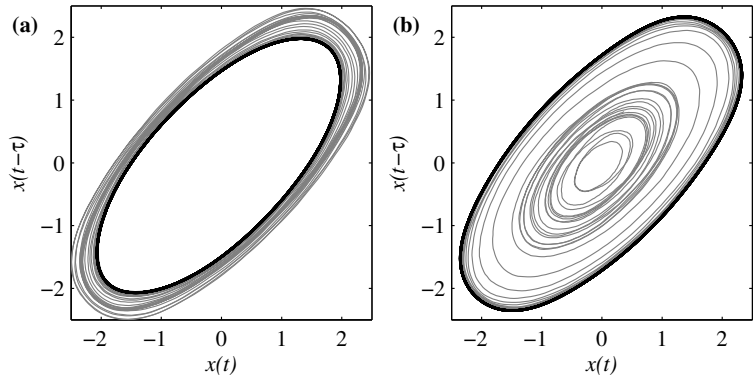


Figure 4: Reconstructed phase plane orbits using the current state $x(t)$ and a delayed coordinate $x(t-\tau)$, showing two examples of divergence from unstable equilibrium states. (a) System is initialized on the stabilized equilibrium state marked by #10 in Figure 3 corresponding to the initial orbit (▬). Once the control is disabled, the measured state $x$ starts to diverge from this equilibrium state and settles onto the upper branch, at slightly larger amplitude. (b) Control is disabled from state #16 which results in $x$ diverging and settling onto the lower branch, at a much smaller amplitude.

### *3.1. Method 1: Free flight stability check*

The first method is based on a simple heuristic idea: Turn off the control actuators and observe if the current state $x$ diverges from the reference state $y$, implying that the equilibrium state is unstable. Figure 5 presents time series from such an experiment starting from different equilibrium states. A conclusion to draw from these time series is that it can be helpful to study the divergence of the difference $x - y$ rather than $x$. A state can diverge from an equilibrium both in amplitude and phase and the latter is more pronounced in the difference $x - y$ (compare Figure 5b and 5c). We define a normalized root mean square error

$$\varepsilon = \frac{\mathrm{RMS}(x-y)}{1+\mathrm{RMS}(y)} \tag{3}$$

where RMS denotes the root mean square value of a sampled signal defined as

$$\mathrm{RMS}(x) = \sqrt{\frac{1}{n}\left(x_1^2 + x_2^2 + \cdots + x_n^2\right)}. \tag{4}$$

The error $\varepsilon$ provides a combined measure of how fast and far a state $x$ diverges from a reference state $y$ upon disabling control, and it seems to be a robust measure of instability. A large error $\varepsilon$ means that the state $x$ has diverged from the reference state $y$, and we consider it to be unstable. Since $\varepsilon$ is a continuous measure it is required to select a threshold for instability. If the error exceeds this threshold, the equilibrium state is considered unstable and vice versa. Figure 6 shows the error $\varepsilon$ for each point of the bifurcation diagram in Figure 3 along with the chosen threshold for stability. The grayscale used in Figure 3 reflects the value of $\varepsilon$ and is interpolated between each measured point along the curve. It appears that the estimator predicts regions of instability that is in good agreement with theory.

There are some precautions to take when using the free flight stability test: Some systems can be allowed to have unbounded divergence, while others cannot. In order to resume the continuation after a stability check, the control must be able to restore the system to the reference state. This requires the divergence not to damage or alter the system, and requires more available control energy than is necessary for the continuation itself. Furthermore, stable and unstable states may lie close in phase space, and depending on precision of the test equipment it may be hard to

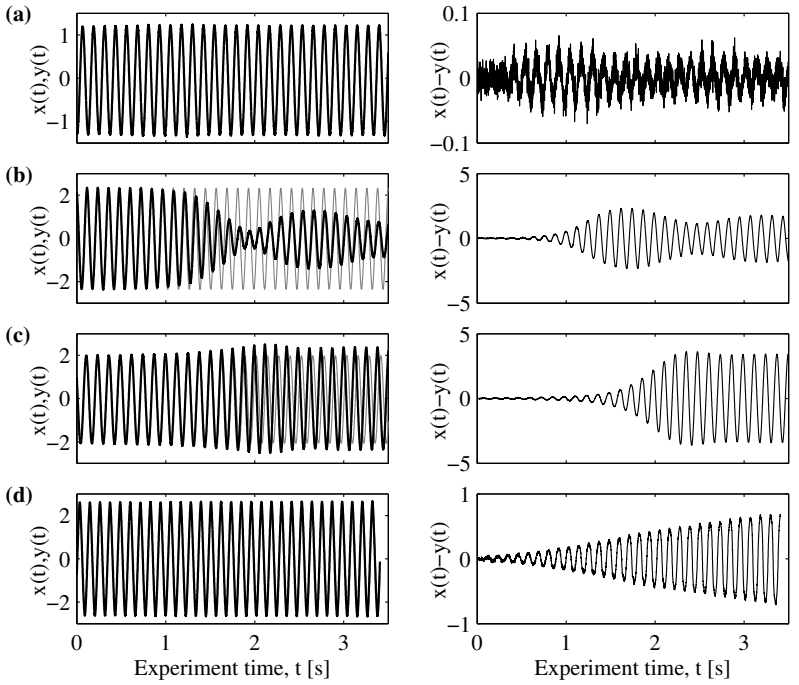


Figure 5: Time series for free flight stability tests. Left column: Time series of $x$ (—) and $y$ (—). Right column: Difference between current state and reference state ($x - y$). (a) Starting at a stable state (#5). (b) Divergence from unstable (#16) and settling onto lower amplitude stable state, the divergence predominantly changes the amplitude. (c) Divergence from unstable (#10) onto higher amplitude stable state, the divergence changes both phase and amplitude. (d) Stability test at a state very close to the upper fold point (#24), divergence is weakly exponential since the state is close to marginally stable. Note the different scales in the right column.

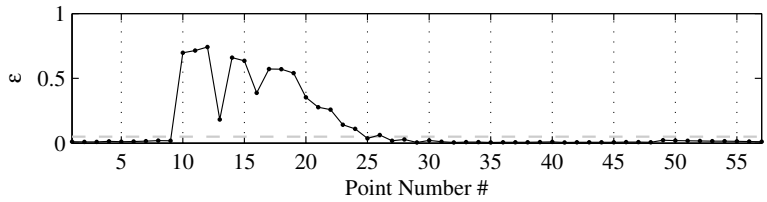


Figure 6: Stability indicator $\varepsilon$ for the bifurcation diagram in Figure 3. Numbers on the x-axis correspond to label numbers along the bifurcation branch. The chosen threshold, which indicates the limit of instability $\varepsilon_t = 0.05$, is marked by (- - -).

distill a binary measure of stability, as the indicator for stability in some cases approaches the threshold for instability smoothly (cf. Figure 6).

Interpreting the time series for $x$ or the difference $x - y$ (cf. Figure 5) is straightforward for some states but less obvious for others. Signals may look qualitatively different, depending on their location in the bifurcation diagram. Nevertheless the divergence seems to be close to exponential for most unstable states, which means that a one degree of freedom linear harmonic oscillator solution of the form: $x-y = Ae^{\lambda t}\cos(\omega t+\phi)+d$ (with variable phase $\phi$, variable amplitude $A$ and DC-offset $d$) can be fitted. The finite-time Lyapunov exponent $\lambda$ will give information about how fast the system diverges. A more simple strategy is to do a linear fit to the logarithm of the peaks (cf. Figure 7), which compares to looking at a Poincaré section. The slope of the linear fit will also yield the finite-time Lyapunov exponent $\lambda$.

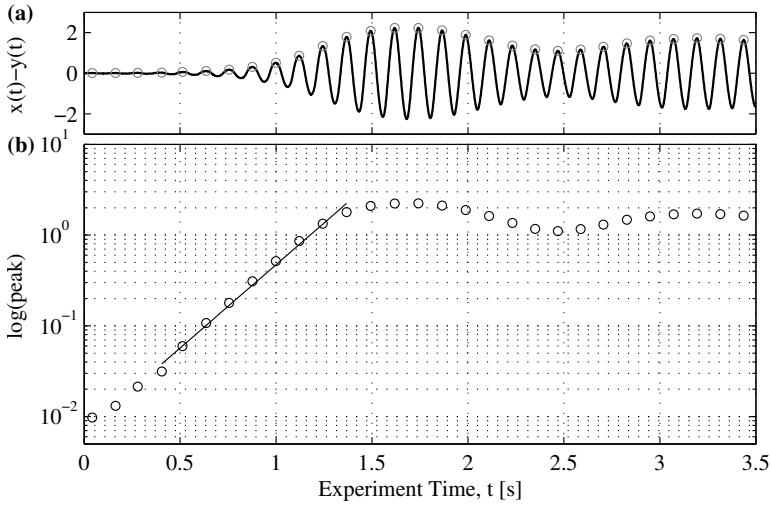


Figure 7: Retrieving stability information for an unstable state (#16) by using a linear fit to the logarithm of the peaks. (a) Smoothened difference $x-y$ with detected peaks (using the Matlab functions: Smooth (moving average filter from the Curve Fitting Toolbox) with a 20 points window and Findpeaks (Signal Processing Toolbox)). (b) Logarithmic plot of the detected peaks (∘) along with linear fit (—) in the time-interval $t \in [0.4; 1.2]$.

### *3.2. Method 2: Stability check using deadband control*

We introduce a deadband $\Pi$ in the non-invasive control signal (2)

$$u(t) = \begin{cases} 0 & \text{for } \|PD(x(t) - y(t))\| \leq \Pi \\ PD(x(t) - y(t)) & \text{for } \|PD(x(t) - y(t))\| > \Pi. \end{cases} \tag{5}$$

Now nonzero control will only be enabled when the requested control signal exceeds the deadband. Proper choice of this deadband will cause the control to enable only if the state $x$ diverges from the reference state $y$. Stability is determined by noting if the control was enabled. The number of control bursts might also be used as a continuous measure of stability for more noisy systems. Figure 8 shows time series for a deadband stability check for a stable and an unstable state. Note that the control is only enabled for the unstable state, and that the state $x$ is not allowed to have unbounded divergence. The width of the deadband can be selected to be of the same order of magnitude as the noise in the control signal, but in Figure 8 it has been kept relatively wide for visualization purposes. For the deadband stability check to work, the deadband must be correctly adjusted (considering noise, closeness of nearby states and

the controls' ability to restore the system) and the time window for the stability check must be long enough for the system to diverge noticeably at all unstable states.

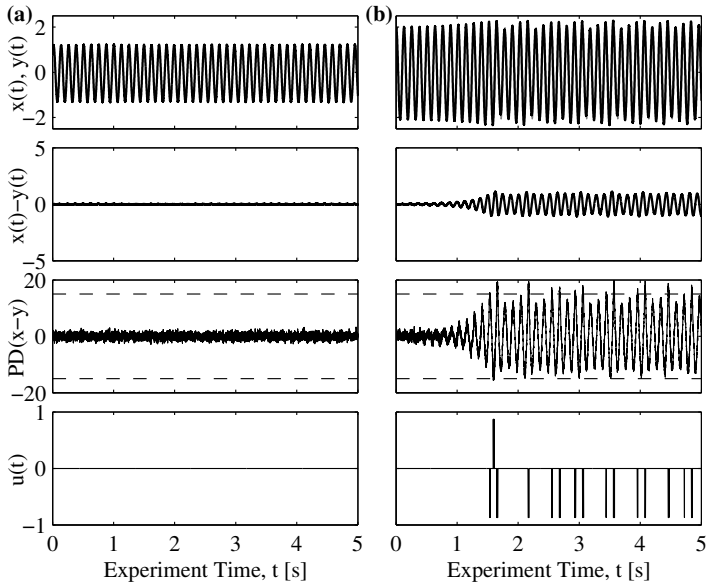


Figure 8: Time series for deadband control stability tests at (a) a stable state (#5) and (b) an unstable state (#10). Deadband limits (**- - -**) are shown together with controller output in the third panel and the deadbanded control signal which is sent to the actuators is shown in the fourth panel. Note that the control is only active for the unstable state (b) and that it manages to reduce the divergence amplitude of the system comparing with Figure 5c.

### *3.3. Method 3: Deadband-limited free flight*

This method combines the advantages of Method 1 and 2 in order to measure finite-time Lyapunov exponents $\lambda$ without allowing unbounded divergence. The trade-off is that the method requires conditions which cannot always be expected from an experiment: The measurements have to be relatively clean, and the divergence has to be approximately exponential. Furthermore, the measured states must be allowed to diverge inside the deadband, which requires the divergence to be completely reversible by the control. In other words, the divergence must not alter the system and the control must be able to restore the equilibrium state after measuring stability.

We modify the deadband control such that whenever the deadband is exceeded ($\|PD(x(t) - y(t))\| > \Pi$) the control signal $u(t)$ is held active for a certain time interval $T \in [t_{enable}; t_{enable+hold}]$. Consequently, the system is restored to the reference state meaning that $x - y \approx 0$. The result is a sequence with several periods of free flight limited to diverge only inside the deadband as it is shown in Figure 9. For a sufficiently narrow deadband the divergence will only include the local (exponential) behavior and not allow the system to settle onto a different stable equilibrium state. Our observations suggest that the estimated Lyapunov exponent is not dependent on which side of the branch of unstable equilibria the state diverges to, as long as we only study the local behavior. For each stability check (at every point of the bifurcation curve) the following postprocessing is performed:

1. Center the data set $x - y$ by subtracting its mean value.
2. Smoothen the time series using a moving average / lowpass filter. In Matlab this can be done by using the function 'smooth' (Curve Fitting Toolbox).

3. Detect peaks of the absolute value of the smoothened signal to get both positive and negative peaks. It can be helpful to use a peak detection algorithm that can discard values smaller than a certain tolerance and require the peaks to be separated by a certain time span. In Matlab this can be done using the function 'findpeaks' (Signal Processing Toolbox).
4. Divide the data set into separate segments of free flight. This can be done by checking the control signal, as this is zero when the system is in free flight, cf. Figure 9.
5. Evaluate the Cooks' distance [9] for each segment and use this information to remove statistical outliers from the data sets.
6. Perform linear interpolation on each set of peak data and average the slopes to get the finite-time Lyapunov exponent $\lambda$.

Near the fold points of the frequency response we experience a slow divergence (Figure 5d) but the exponential fit still seems to be robust, cf. Figure 10. Note also that the method only estimates the divergence rates for unstable states. For stable states the stability is not quantified and the value is set to zero for plotting purposes. For noisy experiments or experiments with low sampling rate, it can be helpful to consider intersections with a hyper plane in the phase space (e.g. zero velocity crossings) rather than detecting peaks of a time series, as the intersection can be located by linear interpolation [10].

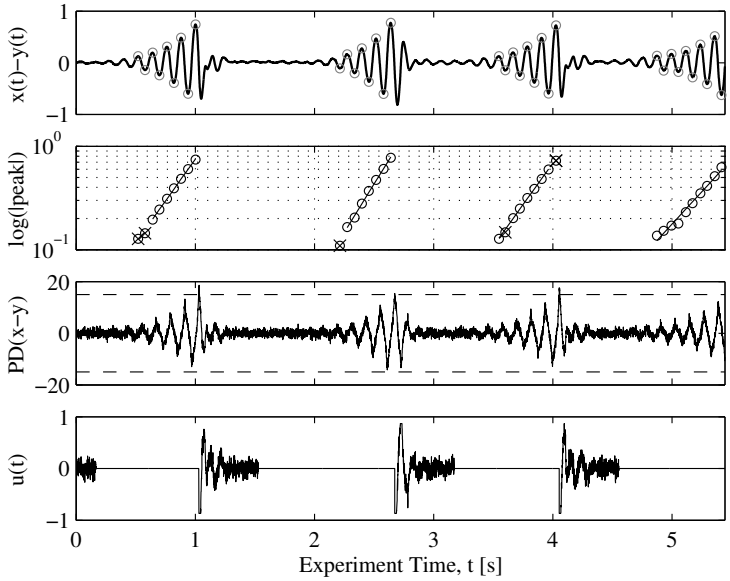


Figure 9: Deadband-limited free flight stability check at an unstable state (#16). Removed outliers are marked by (×) in fit. Average Lyapunov exponent: $\lambda = 3.65 \pm 0.58$.

## 4. Results

The following will present the results of applying the three suggested methods for determining stability during continuation using the test rig presented in Figure 2.

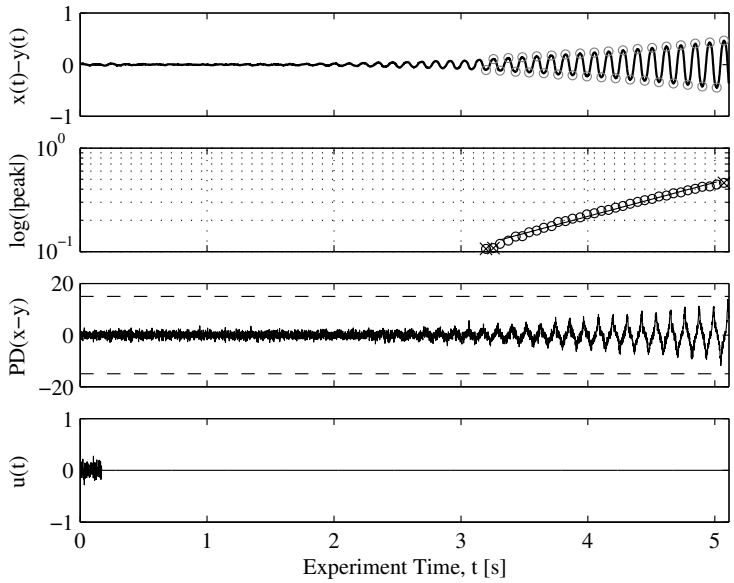


Figure 10: Deadband-limited free flight stability check near the upper fold point (#24). Average Lyapunov exponent: $\lambda = 0.76$. Note the slow divergence compared to the one in Figure 9.

### *4.1. Continuation results*

Figure 11 presents five consecutive continuation runs overlaid along with stability information obtained by the three different stability test methods. Note that Method 1 and 2 give very similar results, while Method 3 estimates the fold point amplitudes a bit higher and with less deviation than the other methods.

### *4.2. Stability near the fold points*

Figure 12 shows the stability estimators for the five bifurcation diagrams depicted in Figure 11, calculated using methods 1 and 3. They are normalized with respect to the total arclength of the corresponding branch, e.g. applying this normalization to Figure 6 the first and last point would get values zero and one respectively. This is necessary since we use an adaptive continuation step length, causing the number of points along each branch to vary. The two methods are seen to give qualitatively similar results, but the free flight test (cf. Figure 12(a)) shows a large jump in estimator at the lower fold point and a smooth transition across the stability limit at the upper fold point. We ascribe this to the fact that the normalized root mean square error $\varepsilon$ is a combined measure of how fast and far a state diverges, rather than an explicit divergence rate such as the finite-time Lyapunov exponent. At the lower fold point, the system diverges and settles onto a stable state quite far from the unstable state, whereas close to the upper fold the bifurcation branches lie very close (cf. Figure 13) causing a short divergence before settling onto a nearby stable state. In comparison, the divergence rate $\lambda$ in Figure 12(b) changes smoothly with respect to the arclength at both fold points. Note that Method 3 detects the onset of instability by the control signal exceeding the deadband which means that an equilibrium state is considered unstable when $\lambda > 0$. Figure 13 shows a zoom of the upper fold point with stability information obtained using Method 3. It is interesting to note how the rate of divergence decreases smoothly when tracking around the fold point, meaning that the stability changes smoothly along the equilibrium branch.

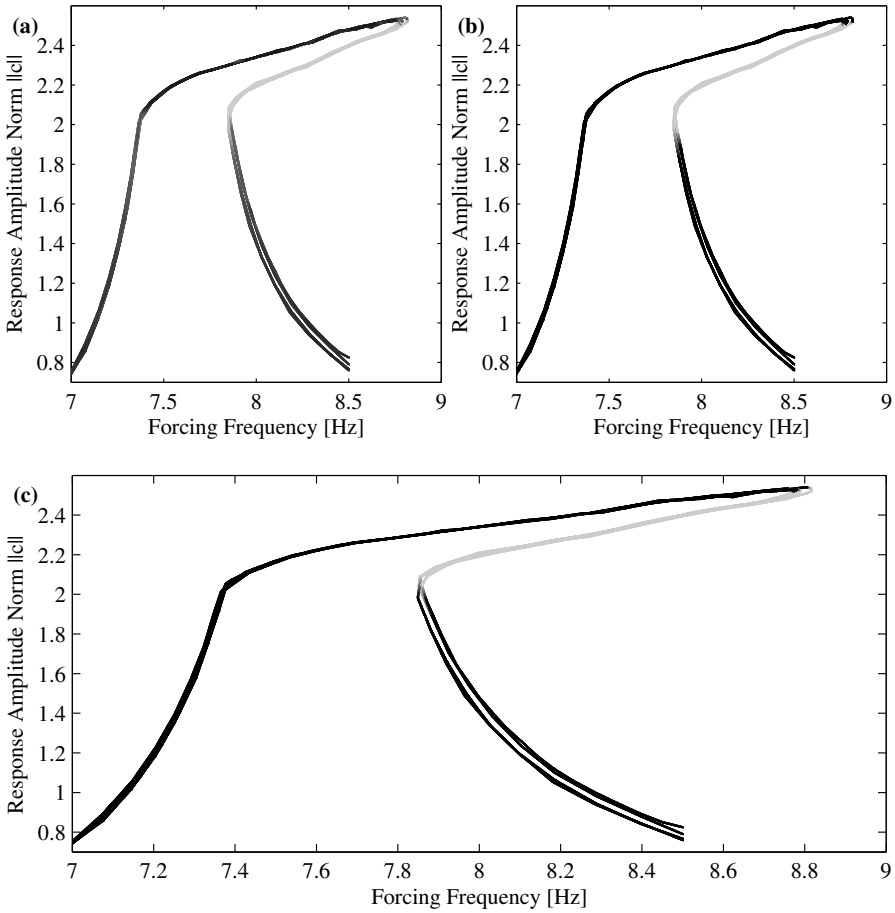


Figure 11: Five overlaid bifurcation diagrams for forcing strength $A = 0.5$ with stability estimator plotted in grayscale (dark for small values, light for larger values). Stability information retrieved using (a) the free flight method (Method 1), (b) the deadband control method (Method 2) and (c) the deadband-limited free flight method with Lyapunov exponent estimation (Method 3). Note that the grayscale has been scaled nonlinearly to visualize the change of stability at the fold points rather than the variation of the estimator along the unstable part of the branch.

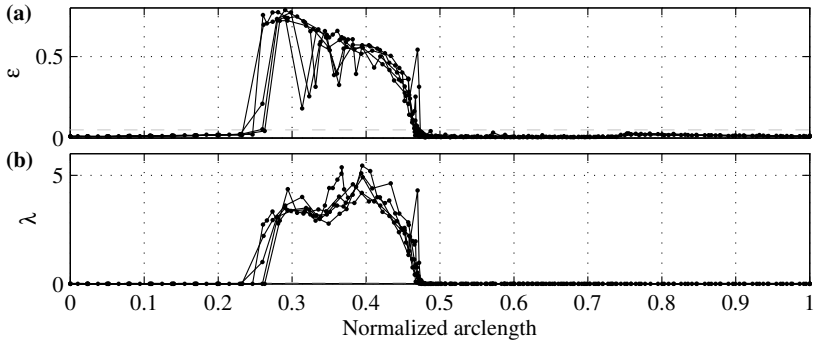


Figure 12: Stability estimator (normalized with respect to arclength of the branch in the bifurcation diagram) of multiple continuation runs. Chosen stability threshold $\varepsilon_t = 0.05$ is marked by (- - -). Top panel shows the normalized root mean square error $\varepsilon$ for a free flight test (Method 1). Bottom panel shows the averaged Lyapunov exponent estimated by the deadband-limited free flight method (Method 3).

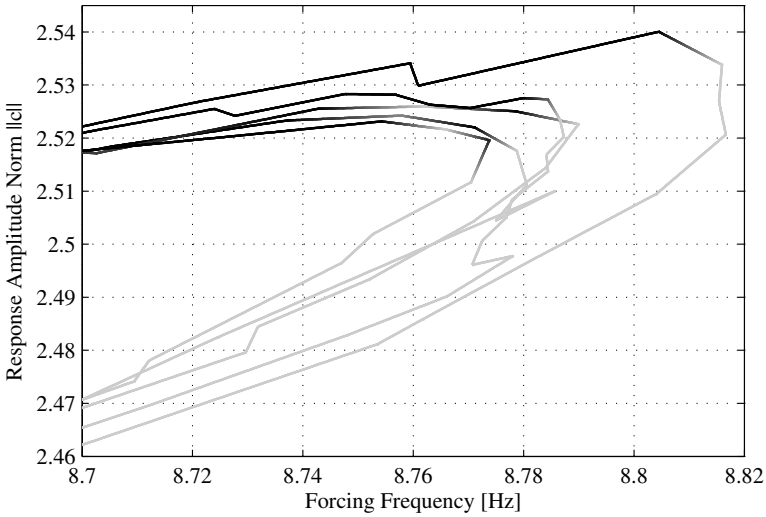


Figure 13: Zoom of the upper fold point in Figure 11(c).

*4.3. Stability at a family of isolated equilibrium branches (isola)*

Figure 14 presents the experimental finding of an isola, by which we mean a family of stable and unstable equilibrium branches that are detached from the primary resonance peak in the bifurcation diagram. This isola is created by a 1:3 subharmonic resonance, at which the impactor is forced at approximately three times its fundamental resonance frequency, but the response is approximately at its fundamental resonance frequency. The isola was found by parameter sweep and two consecutive continuation-runs. Its existence was suggested by simulation of a single-degree-of-freedom model of our test rig [11] and was initially found by systematic parameter sweeps. Several branches of stable as well as unstable equilibria seem to coexist in that parameter region and continuing of the unstable branches is a mean for mapping out a more complete picture of the possible dynamical responses. Near 26.6-26.8 Hz the branches cease to exist due to a shift in the phase between impactor and platform, i.e. the impactor and platform starts to vibrate in-phase, which causes the relative amplitude between impactor and mechanical stops to be insufficient for impact, which in turn effectively changes the response of the system. At this point, the sweep settles onto a stable equilibrium at a much lower amplitude, while the continuation reports an endpoint and terminates. A more refined and systematic investigation of this isola requires the precision of measurements and actuation to be increased, as well as implementing a means to do systematic branch switching at bifurcation points.

For the case of the isola, it was only possible to successfully apply the deadband control stability test (Method 2), as it would otherwise not be possible for the control to restore the equilibrium states after stability check. The deadband had to be adjusted to only allow divergence just above the noise level (5 times tighter than the deadband in Figure 8). Due to noise, the control signal would exceed the deadband a few times at the stable states, causing a few control bursts, while unstable states were characterised by an effectively active control (an approximate factor of 100 more control bursts).

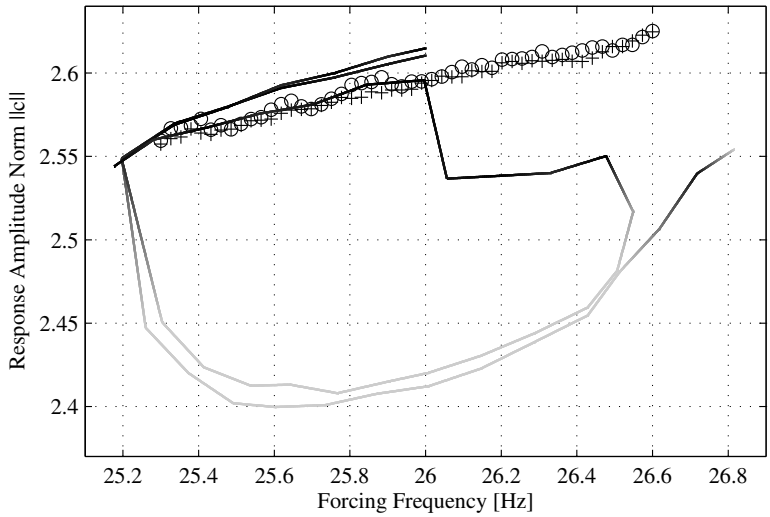


Figure 14: Isola composed of the stable and unstable equilibrium branches of a 1:3 subharmonic resonance found by a parameter sweep and two consecutive continuation-runs, using different settings for tolerances and step size. The sweep is denoted by (+) for increasing and (∘) for decreasing frequency. Stability information is assessed using Method 2.

## 5. Conclusions

The experiments presented show that it is possible to assess stability during control-based continuation of bifurcation branches by momentarily modifying or turning off the control. Three different methods have been proposed: 1) Free flight stability check, 2) stability check using deadband control, and 3) deadband-limited free flight. All three methods have been successfully applied to determine stability during experimental continuation, and each of the methods is shown to be suitable in different situations:

The free flight stability test (Method 1) is robust and easy to implement but requires the divergence to be completely reversible by the control. The estimated normalized RMS error between reference and measured state is shown to give a good indication of the stability but does not provide direct information about the rate of divergence. Similarly, the deadband stability check (Method 2) does not provide information about the rate of divergence, but on the other hand has the advantage to be employable while only allowing minimal divergence. The isola presented in Section 4.3 is a good example of the usefulness of Method 2, since its ability to limit the divergence to a pre-defined maximum makes it the only of the three methods which allows stability assessment in this situation.

Finally the deadband-limited free flight method (Method 3) is able to provide an estimate of the rate of divergence while allowing only a limited divergence. In turn the method puts more requirements on the experiment, is more difficult to implement and has more parameters that need to be adjusted. The stability estimator is observed to approach the stability threshold smoothly at bifurcation points regardless of the stability test method. In other words, continuing a branch of equilibria, the stability is noted to change smoothly, e.g. from unstable to stable, especially at the upper fold point. A quantitative measure of stability is determined only at unstable states; to extend the capability to stable states, one could introduce an in-phase perturbation and measure the (exponential) decay of transients. Unfortunately, for the system that we investigate this is difficult because the transients are damped out within few oscillations at stable equilibrium states away from the fold points. To get just a few points for estimation the perturbation has to be so strong it effectively changes the response of the system. This could possibly be improved using a fitting method which fits the whole data set rather than just the peaks.

The isola presented in Figure 14 serves as a good example of the usefulness of control-based continuation method with additional stability investigations. It shows how the method can be used to obtain a more complete picture of the bifurcation diagram in regions where multiple stable and unstable equilibrium states coexist. Furthermore, it is seen that continuing branches of unstable equilibria can be the key in discovering seemingly unconnected stable equilibrium branches. It also points out room for improvement, by underlining the need for a method to switch between multiple branches at bifurcation points. Other possibilities for future research include fitting the time series obtained during free flight to a single-degree-of-freedom harmonic oscillator to get statistically more accurate estimates of the finite-time Lyapunov exponents. It might also be possible to determine the stability directly from the control signal. In our experiments the control signal appears to be uncorrelated noise once the correction step has converged, regardless of the stability of the equilibrium state. Perhaps superimposing the control with a noise signal or even introducing a locally destabilizing control can help to develop maybe a faster method to determine stability and to obtain further insights.

## 6. Acknowledgements

This work was supported by the Danish Research Council FTP under the project number 09-065890/FTP. The authors wish to thank Jan Sieber, David Barton, Harry Dankowicz and Bernd Krauskopf for helpful comments when setting up the experiments and Viktor Avrutin for his help with the model investigations of the isola.

## References

[1] J. Sieber, B. Krauskopf, Control based bifurcation analysis for experiments, Nonlinear Dynamics 51 (3) (2008) 365–377. doi:10.1007/s11071-007-9217-2.

[2] J. Sieber, A. Gonzalez-Buelga, S. Neild, D. Wagg, B. Krauskopf, Experimental Continuation of Periodic Orbits through a Fold, Physical Review Letters 100 (2008) 244101. doi:10.1103/PhysRevLett.100.244101.

[3] J. Sieber, B. Krauskopf, D. Wagg, S. Neild, A. Gonzalez-Buelga, Control-Based Continuation of Unstable Periodic Orbits, Journal Of Computational And Nonlinear Dynamics 6 (1). doi:10.1115/1.4002101.

[4] D. A. W. Barton, S. G. Burrow, Numerical Continuation in a Physical Experiment: Investigation of a Nonlinear Energy Harvester, Journal Of Computational And Nonlinear Dynamics 6 (1). doi:10.1115/1.4002380.
[5] D. A. Barton, B. P. Mann, S. G. Burrow, Control-based continuation for investigating nonlinear experiments, Journal of Vibration and Control 18 (4) (2012) 509–520. doi:10.1177/1077546310384004.
[6] E. Bureau, I. Ferreira Santos, J. J. Thomsen, F. Schilder, J. Starke, Experimental bifurcation analysis of an impact oscillator - tuning a non-invasive control scheme, Journal of Sound and Vibration 332 (22) (2013) 5883–5897. doi:10.1016/j.jsv.2013.05.033.
[7] H. Dankowicz, F. Schilder, Recipes for continuation, Vol. 11 of Computational Science & Engineering, Society for Industrial and Applied Mathematics (SIAM), Philadelphia, PA, 2013. doi:10.1137/1.9781611972573.
[8] E. Bureau, I. Santos, J. J. Thomsen, F. Schilder, J. Starke, Experimental Bifurcation Analysis By Control-based Continuation - Determining Stability, in: Proceedings of the ASME 2012 International Design Engineering Technical Conferences & Computers and Information in Engineering Conference, 2012.
[9] R. Cook, Detection of influential observation in linear-regression, Technometrics 19 (1) (1977) 15–18.
[10] O. Corradi, P. Hjorth, J. Starke, Equation-free detection and continuation of a hopf bifurcation point in a particle model of pedestrian flow, SIAM Journal on Applied Dynamical Systems 11 (3) (2012) 1007–1032. doi:10.1137/110854072.
[11] M. Elmegård, B. Krauskopf, H. M. Osinga, J. Starke, J. J. Thomsen, Bifurcation analysis of a smoothed model of a forced impacting beam and comparison with an experiment, ArXiv e-printsarXiv:1308.3647.

Appendix C

# Dimension reduction in dissipative dynamical systems

**Noname manuscript No.**
(will be inserted by the editor)

# Dimension reduction in dissipative dynamical systems

## Manifold approximation in k dimensions via the graph transform

**M. Elmegård · J. Starke**

Received: date / Accepted: date

**Abstract** Using the theory of normally hyperbolic invariant manifolds we approximate attracting submanifolds in high-dimensional dynamical systems with a spectral gap in order to obtain a low-dimensional description. We apply the graph transform method and use it in a natural continuation scheme. The complexity of the construction scales with the dimension of the attracting submanifold. Typically marching methods scale with the much larger codimension. As an example we demonstrate how this method can be applied to obtain very accurate reduced models for the transverse vibrations of a beam with a torsional nonlinearity at one end and a linear spring and harmonic forcing at the other end.

**Keywords** normally hyperbolic invariant manifold · dimension reduction · graph transform · mechanical system · model reduction · reduced order modelling

### 1 Introduction

Mathematical modelling as a discipline has changed its style considerably over the last couple of decades with the increasing computational power. Where approximate solutions to nonlinear differential equations were constructed using for example transforms, perturbation methods and averaging methods such as to be able to construct approximate bifurcation diagrams; today, we construct families of solutions and bifurcation diagrams in the order of seconds for single degree of freedom dynamical systems using numerical continuation and bifurcation software such as, e.g., CoCo [1] and AUTO [2]. At the same

M. Elmegård
Department of Applied Mathematics and Computer Science, Technical University of Denmark, Matematiktorvet, Building 303B, 2800 Kgs. Lyngby, Denmark.
E-mail: melm@dtu.dk

J. Starke
Department of Applied Mathematics and Computer Science, Technical University of Denmark, Matematiktorvet, Building 303B, 2800 Kgs. Lyngby, Denmark.
E-mail: jsta@dtu.dk

time the dimension/degrees of freedom (dof) of the problems that can be solved numerically has increased by many orders of magnitude, e.g., from a small Duffing oscillator $\mathcal{O}(1)$ to a finite element model of the large amplitude vibrations of a beam $\mathcal{O}(10)$ to vibrations of a wing of a windmill $\mathcal{O}(10^6)$. While low-dimensional problems are handled very well by numerical continuation software, it is still not possible to construct bifurcation diagrams for high-dimensional models efficiently. This is due to insufficient computational power, e.g., for performing the many Newton iterations in the continuation runs or handling large Jacobians and in turn evaluate test-functions for bifurcations. With a demand for proper nonlinear analysis of the high-dimensional models, much focus has been put on developing methods that make this possible. There are different approaches to this problem; one of the methods solves the original problem by taking advantage of the spectral gap directly in the Newton steps, see e.g., [3]. Where a continuation and bifurcation analysis of periodic orbits in a large-scale, $10^4$-dimensional, dissipative fluid problem is performed using a Newton-Krylov method. The review article [4] on bifurcation analysis in high-dimensional fluid applications and the specific computational problems that emerge; other approaches are reductive methods under names such as model reduction, dimension reduction, reduced-order-modelling, coarse graining methods, equation-free methods and multi-scale methods. The underlying rationale of reductive methods is that the observed dynamics is often low-dimensional compared to the very high-dimensional ambient space where the models are naturally described. Low-dimensional dynamics may be classified in a number of ways, for example, via data analysis (manifold learning, signal analysis), or by classifying according to the geometry and complexity of the asymptotic dynamics or bifurcation structures, e.g., periodic solutions and tori. The fundamental idea of (most) reductive methods is that they are based on the assumption that orbits quickly relax to some low-dimensional attracting submanifold in a high-dimensional ambient space. The time-scale separation, in the contractive and expansive sense, often appears under names such as spectral gaps [5], generalized Lyapunov-type numbers [6], [7], exponential dichotomies [8]; with varying definitions these properties describe the effect of how volumes contract in phase space in the neighborhood of, e.g., attracting manifolds, and in that sense they are all simple geometric quantities. In model reduction one then attempts to chart the attracting manifold to a low-dimensional subspace in a way such that the attractor in the reduced system is diffeomorphic to the original attractor. This idea naturally leads to a non-trivial problem of identifying suitable mappings. Many reductive methods exist in different applied fields, a small selection is for example, in *chemical engineering*, intrinsic low-dimensional manifold (ILDM) [9], computational singular perturbation [10], an iterative method [11]; in *mechanical engineering*, proper orthogonal decomposition (POD), method of snapshots, balanced truncation [12], and nonlinear normal modes (NNM) [13], [14], [15], [16], [17].

A mechanical system is considered in the current paper as an example application. Therefore, we comment on the approaches to model reduction in mechanical systems. The *method of snapshots* is based on finding basis func-

tions to project the reference dynamical system onto, thereby constructing a reduced order model, i.e., the method is based only on linear projections. The basis functions are found by sampling many orbit trajectories and then following up with data analysis, e.g., via proper orthogonal decomposition (POD) to derive an optimal (in least squares sense) fit of the point cloud by a $k$-dimensional hyperplane where $k \ll n$; equivalently this may be considered as a statistical regression problem of maximizing variance using $k$ basis vectors to span the k-dimensional hyperplane. The main advantage of such a reduction technique is that it can potentially be applied rather efficiently to high-dimensional problems; the drawback is that there is no guarantee that the nonlinear behavior is captured by a hierarchy that prioritize projections according to, e.g., energy or variance, see for example [18].

The method of NNMs in dissipative systems with an invariant manifold approach was presented in [14] and may be viewed as a type of center manifold reduction. Using the method of NNMs an attracting submanifold is constructed and asymptotic as well as transient behavior is predicted very well in several applications, see e.g., [19]. The main drawback of this method, when used for dissipative systems, is that for a $k$-dimensional submanifold in an $n$-dimensional dynamical system $n - k$ first order nonlinear coupled partial differential equations must be solved and in large scale systems, $k \ll n$, and in general, such methods are sensitive to the tangent and normal dynamics of the submanifold as well as the boundary condition, i.e., the $(k-1)$-dimensional hypersurface.

In the present paper we will approach the problem of dimension reduction with methods from dynamical systems theory, specifically we will apply the *graph transform* (GT) and the theory of *normally hyperbolic invariant manifolds* (NHIM) in order to derive low-dimensional models. As example we reduce a mechanical vibration problem from 25 to 3 dimensions and show that even transient behavior is accurately predicted. This model was chosen as an example because it was previously analyzed using the method of NNMs in [16]. The structure of the paper is as follows: in Section 2 we motivate the geometrical approach to dimension reduction through bifurcation analysis and invariant manifolds, we state Theorem 1 of [6] which is the theoretical basis for the reduction method and explain the hypotheses and the consequences of the theorem; in Section 3 we give the details of the graph transform; in Section 4 we give the details of it and two methods that may be used to perform the transform and we discuss the modifications needed for the graph transform to work in the present setting; in Section 5 the method is applied to a nonlinear mechanics problem and results are presented; in Section 6 convergence properties and results are presented; in Section 7 we conclude with a discussion of advantages, disadvantages and perspectives of the method.

## 2 Attracting submanifolds in dissipative dynamical systems

In the current section we will provide an overview and some background of the theory that we will use to reduce the dimension of dissipative dynamical systems. While the theoretical constructions are mathematically technical, the concepts are relatively simple and of geometrical flavor; we will provide the sufficient details with a stress on geometry.

The choice of method for dimension reduction in dynamical systems depends very much on the purpose. For equilibrium/fixed points the center manifold reduction [20], [21] can be applied to derive reduced representations according to the dimension of the nonhyperbolic linear subspaces of the fixed point, i.e., the center eigenspace which is spanned by the eigenvectors with corresponding eigenvalues $\lambda$ with $\mathrm{Re}(\lambda) = 0$. In essence; all auxilliary phase space variables are locally given by the variables of the center eigenspace. The center manifold persists under small perturbations, meaning that if a bifurcation occurs it can be unfolded in the reduced set of equations. Consider the following dynamical system,

$$\begin{aligned} \dot{x} &= Cx + f(x, y, \alpha), \\ \dot{y} &= Sy + g(x, y, \alpha), \\ \dot{\alpha} &= 0, \end{aligned} \tag{1}$$

where $(x, y, \alpha) \in \mathbb{R}^{n_c} \times \mathbb{R}^{n_s} \times \mathbb{R}^{n_p}$,$f(0, 0, 0) = g(0, 0, 0) = 0$, all eigenvalues of the matrix $C$ have zero real part and all eigenvalues of the matrix $S$ have negative real part. In a neighborhood of the fixed point $(x, y) = (0, 0)$ there exist invariant center manifolds all of which share the same qualitative dynamics, and on these $y = h(x, \alpha)$ resulting in a reduced dynamical system

$$\dot{x} = Cx + f(x, h(x, \alpha), \alpha). \tag{2}$$

The relation $y = h(x, \alpha)$ is generally non-unique, but sufficiently close to the fixed point the whole family of center manifolds will exhibit the same qualitative behavior. We can therefore consider variations in the model parameter $\alpha$. A related and more general concept is the invariant manifold theorem for fixed points, see e.g., [21]. For dimension reduction purposes this implies that if a local bifurcation occurs it is represented in the reduced dynamical system (2), i.e., it is the ideal nonlinear projection for the reduction; note that a linear projection may fail badly (cf. linear projection methods in general).

In the current paper we want to construct dimension reductions in the connection of more complicated sets than fixed points. In particular the manifolds that will be approximated are 'global' and therefore a generalization of the center manifold theorem that applies to sets is needed; this theoretical result is due to Fenichel [6] and for a more accessible entry to the subject see Wiggins [7]. Another useful approach that could, under some additional assumptions, have been taken as basis for this work is the approach of geometric singular perturbations [22], [23].

We restate the result of Fenichel 1971 verbatim

**Theorem 1** *(Fenichel, 1971 [6])*
*Suppose $\dot{x} = f(x)$ is a $C^r$ vector field on $\mathbb{R}^n$, $r \geq 1$. Let $\bar{M} \equiv M \cup \partial M$ be a $C^r$ compact connected manifold with boundary overflowing invariant under the vector field $f(x)$. Suppose $\nu(p) < 1$ and $\sigma(p) < \frac{1}{r}$ for all $p \in M$. Then for any $C^r$ vector field $f^{pert}(x)$ $C^1$ $\theta$-close to $f(x)$, with $\theta$ sufficiently small, there is a manifold $\bar{M}^{pert}$ overflowing invariant under $f^{pert}(x)$ and $C^r$ diffeomorphic to $\bar{M}$.*

A compact manifold with boundary is called *overflowing invariant* if the flow $\phi^t$ of $\dot{x} = f(x)$, is pointing strictly outward at the boundary and if $p \in M$ implies that $\phi^t(p) \in M$ for $t \leq 0$. The functions $\nu(p), \sigma(p)$ are the *generalized Lyapunov-type numbers*. $\nu(p) < 1$ for all $p \in M$ means that vectors normal to the manifold $M$ *expand* in negative time under the linearized dynamics; the closer $\nu(p)$ is to 0 the stronger is the attraction towards the manifold. When $\sigma(p)$ approaches 0 it means that a volume in the neighborhood of the manifold will flatten quickly along the manifold in forward time. Furthermore; $f(x)$ and $f^{pert}(x)$ are $C^1$ $\theta$-close on a compact set $\mathcal{K}$ containing $M$ if

$$\sup_{x \in \mathcal{K}} ||f(x) - f^{pert}(x)|| \leq \theta, \tag{3}$$

$$\sup_{x \in \mathcal{K}} ||Df(x) - Df^{pert}(x)|| \leq \theta. \tag{4}$$

Theorem 1 is a particularly strong and useful result for many purposes in qualitative and quantitative analysis of dynamical systems. It is a persistence result, i.e., it provides a priori knowledge about possible changes of the overflowing invariant manifold when we perturb or deform their corresponding dynamical system. While we apply the implicit function theorem for, e.g., bifurcation analysis of equilibrium points or periodic orbits etc., we may interpret $\nu(p)$ and $\sigma(p)$ as global bifurcation parameters of the overflowing invariant manifolds, see [7]. In Figure 1 we illustrate some of the concepts through a geometrically intuitive example of why we need the conditions of Theorem 1 on the *generalized Lyapunov-type numbers*. In Panel 1(a) the contraction normal to the manifold $M$ is stronger than the contraction tangent to $M$, i.e., $\sigma(p) < 1/r$; $M$ is overflowing invariant; $M$ is attractive, i.e., $\nu(p) < 1$. In this case the perturbed manifold is $C^r$ and sketched as the red curve. In Panel 1(b) the contraction normal to the manifold $M$ is weaker than the contraction tangent to $M$, i.e., $\sigma(p) > 1$; $M$ is overflowing invariant. In this case $M$ is not normally hyperbolic and as a consequence the manifold may bifurcate under the perturbation of the vector field.

In the current setting we apply the theory to ODEs, i.e., finite-dimensional systems and this implies that the compactness is equivalent to being closed and bounded (Heine-Borel theorem). Connectedness is trivially verified for our application.

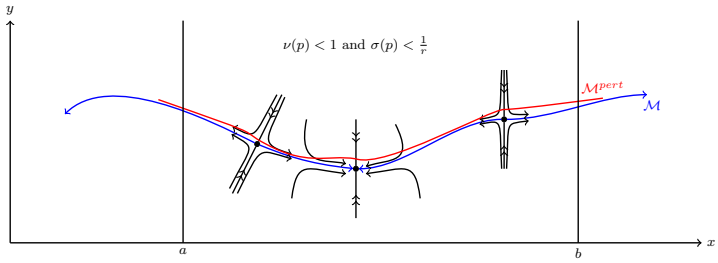


(a)

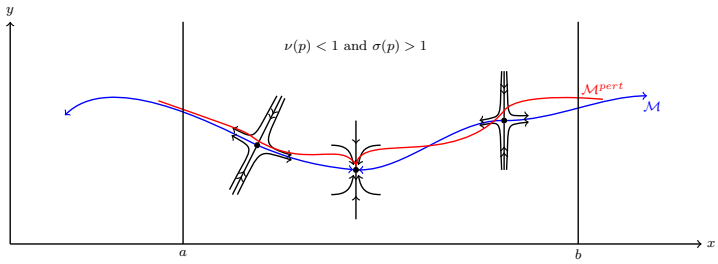


(b)

Fig. 1: Geometrical illustration of Theorem 1 for a compact domain $U = [a, b]$: Panel (a) shows an overflowing NHIM with $\nu(p) < 1$ and $\sigma(p) < 1/r$ for all $p \in M$ in the dynamical system $\dot{x} = f(x)$. The red curve illustrates the persistence of the NHIM in a $\theta$-close dynamical system $\dot{x} = f^{pert}(x)$. Panel (b) shows the same case but with the violation $\sigma(p) > 1$ of Theorem 1, in this example the perturbed manifold develops a cusp at the center fixed point.

## 3 Approximating attracting submanifolds via the graph transform

The proof of Theorem 1 can be done via the graph transform method [6], [7]. We will apply the results for the discrete approximation of compact normally hyperbolic invariant manifolds demonstrated in [27], [28], [29], [30], [31] for manifolds without boundary. In [31] an example is given for which pieces of an attracting two-dimensional manifold that violates the overflowing condition are constructed using the graph transform with a small modification. We will rely on the same type of modification in the numerical approximation of k-dimensional manifolds. We remark here that our list of references for the work on normally hyperbolic invariant manifolds is by no means exhaustive and we are aware that there exist related results for generalized center manifold theorems and integral manifolds in nonautonomous systems.

Next we give an introduction to the graph transform with the necessary details for the numerical constructions given in the following sections. Consider

the following dynamical system

$$\begin{aligned} \dot{x} &= f(x, y, \lambda), \\ \dot{y} &= g(x, y, \lambda), \end{aligned} \tag{5}$$

where $x \in \mathbb{R}^k$, $y \in \mathbb{R}^{n-k}$, $\lambda \in \mathbb{R}$ and $f, g$ are $C^r$ functions of all variables. Let $M_0$ be a compact overflowing NHIM of the dynamical system (5), with $\lambda = 0$, defined by,

$$M_0 = \left\{(x, y) \in \mathbb{R}^k \times \mathbb{R}^{n-k} \middle| y = h_0(x), \lambda = 0, \forall x \in \mathrm{U} \subset \mathbb{R}^{\mathrm{k}}\right\}. \tag{6}$$

where $h_0 : \mathbb{R}^k \mapsto \mathbb{R}^{n-k}$ is $C^r$ and $U$ is a compact connected subset. It follows directly from Theorem 1 that since $M_0$ is a compact overflowing NHIM there is a one-parameter family of NHIMs defined by the parameter $\lambda$. Let $f_\lambda, g_\lambda$ be vector fields that are $\theta$-close to $f, g$ for sufficiently small $|\lambda|$. The graph transform may be performed using $M_0$ as initial condition to converge to $M_\lambda$ because it is a priori known that $M_\lambda$ is to be found in a tubular neighborhood of $M_0$. In the current application the tubular neighborhood may be considered as the one shown in Figure 2. Let $x(t, x_0, y_0) \equiv F^t(x_0, y_0)$ and $y(t, x_0, y_0) \equiv$

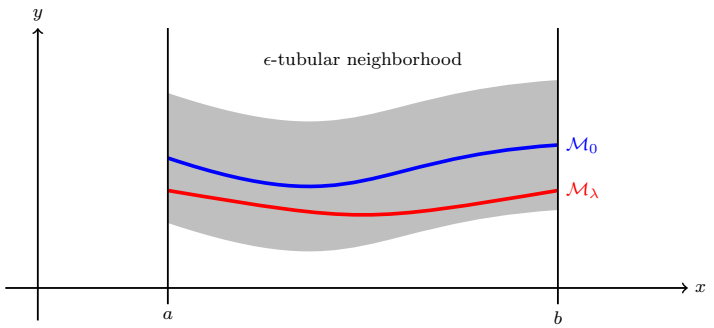


Fig. 2: Illustration of a tubular neighborhood (gray) of $M_0$ (blue) which is the overflowing NHIM in the unperturbed dynamical system. $M_\lambda$ (red) is the overflowing NHIM of a $\theta$-close dynamical system which via Theorem 1 is inside the tubular neighborhood. The compact domain is $U = [a, b]$.

$G^t(x_0, y_0)$ be the flow of Equations (5). We also use $\phi^t$ as a more compact notation for the flow, i.e., $\phi^t(x, y) \equiv \begin{pmatrix} F^t \\ G^t \end{pmatrix}(x, y)$. We illustrate the graph transform in Figure 3 and define it as follows,

$$\mathrm{graph}(h^{i+1}) = \begin{pmatrix} F^t \\ G^t \end{pmatrix}(\mathrm{graph}(h^i)), \tag{7}$$

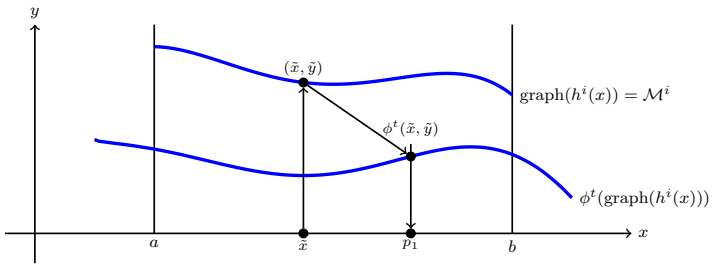


Fig. 3: Illustration of graph transform. $\phi^t$ is the flow of the considered dynamical system and $\tilde{y} = h^i(\tilde{x})$. For the consecutive iteration of the graph transform $\phi^t(\text{graph}(h^i(x)))$ is cut at the boundaries of the compact domain $U = [a, b]$.

where the equality only holds after cutting of the manifold at the boundary of the compact domain (in Figure 3 the interval $[a, b]$). The superscripts, $i$ and $i + 1$, denote the iterative sequence and graph$(h^i)$ is the $i$th graph transform defined by

$$\text{graph}(h^i) = M^i = \left\{(x, y) \in \mathbb{R}^k \times \mathbb{R}^{n-k} \middle| y = h^i(x), \forall x \in \mathrm{U} \subset \mathbb{R}^{\mathrm{k}}\right\}. \tag{8}$$

Remember that the domain of the graph transform is compact and the manifold is overflowing by assumption; this together with several other properties, e.g., a Lipshitz condition on the vector field, makes the graph transform a contraction mapping on a suitable function space that ensures existence and uniqueness of solutions. Note that the overflowing condition at the boundary is necessary for the pre-image, under $\phi^t$, of $M^{i+1}$ to be inside a tubular neighborhood of $M^i$, cf. Figure 3. If all the hypotheses of Theorem 1 are satisfied it implies that $h^i \to h^\infty$ as $i \to \infty$ where graph$(h^\infty)$ is the unique compact overflowing NHIM, i.e., it satisfies the invariance (fixed point) equation

$$\begin{pmatrix} F^t \\ G^t \end{pmatrix} (\text{graph}(h^\infty)) = \text{graph}(h^\infty), \tag{9}$$

where it is again necessary to cut-off at the boundary. We point out that the goal is to construct an approximation to graph$(h^\infty)$. Another important property of the graph transform is that the iterative sequence only converges at a linear rate; this implies that the size of the difference in contraction rates $\sigma(p)$ will be important for practical purposes. We will refrain from commenting on wether the graph transform is fast or slow. The objective measures are the linear convergence rate; computational complexity, i.e., $\mathcal{O}(n^3)$ vs. $\mathcal{O}(k^3)$; and the size of the spectral gap. Firstly, linear convergence is an obvious drawback; secondly, if $k \ll n$ methods that scale with $k$ are advantageous; thirdly a large spectral gap may give convergence after a few graph transform steps and small spectral gaps will take many iterations. We therefore stress that the practical usefulness is as all other methods dependent on the application at hand. Now

let us illustrate how for example the spectral gap is crucial to the usefulness of the graph transform by considering the simplest possible case [7];

$$\begin{aligned} \dot{x} &= \alpha x, \\ \dot{y} &= -\beta y, \end{aligned} \tag{10}$$

where $\alpha, \beta \in \mathbb{R}_{>0}$ and $x, y \in \mathbb{R}$. Here we easily verify that

$$M = \left\{(x, y) \in \mathbb{R} \times \mathbb{R} \middle| y = 0, \text{ for } x \in [-1, 1]\right\}, \tag{11}$$

is an example of a compact overflowing NHIM (and also the unstable manifold of the fixed point $(0, 0)$). The *generalized Lyapunov-type numbers* in this system are given by $\nu = \exp(-\beta)$ and $\sigma = \alpha/\beta$, note that in this case the numbers do not depend on the position $p$. Weak normal hyperbolicity or small spectral gap corresponds to $\sigma(p)$ being close to 1 and strong normal hyperbolicity or large spectral gap corresponds to $\sigma(p)$ being close to 0. In the same sense one can imagine that strong normal hyperbolicity has a dampening effect on the effects of nonlinear perturbations normal to the reduced manifold.

## 4 Numerical approximation of k-dimensional attractive submanifolds via the graph transform

In this section we consider the numerical implementation of the graph transform for the approximation of k-dimensional compact attracting NHIMs of dynamical systems for use in dimension reduction. We present algorithms and discuss their strengths and weaknesses. Our implementation is along the lines of previously detailed accounts presented in [28], [29], [30], [31].

While the graph transform is conceptually easy to understand in the current setting of dimension reduction and the numerical implementation is rather straightforward; the difficulties are mostly of technical character. We have to decide on a finite-dimensional representation of the manifold and there are many possibilities. From a numerical point of view, the priority is to represent the manifold to an acceptable accuracy with a low number of basis functions and the manifold should be computationally inexpensive to evaluate. This is of increasing importance as the dimension of the manifold increases.

For our implementation we have chosen the basis space to be tensor-product splines (cubic $\sim \mathcal{C}^2$) with uniform grid. The main advantage is that the mesh is structured and they are cheap to evaluate. For a $k$-dimensional manifold the tensor-product representation is

$$h(x) \approx \sum_{j_1=0}^{N_1} \sum_{j_2=0}^{N_2} \dots \sum_{j_k=0}^{N_k} c_{j_1 j_2 \dots j_k} \phi_{j_1}(x_1) \phi_{j_2}(x_2) \dots \phi_{j_k}(x_k), \tag{12}$$

where $\phi_{j_i}(x_i)$ is a cardinal spline for the $i$th variable and the coefficients $c_{j_1,\dots,j_k} \in \mathbb{R}^{n-k}$. The evaluation of such a tensor-product with uniform grids is not expensive because the splines have compact support and furthermore

there is only one type of spline in each variable called cardinal spline. Approximations with global basis functions (spectral elements), would be much more expensive to evaluate. A good property which is sacrificed is the possibility of local refinement, e.g., this could be applied via finite elements (interpolation on simplicial complexes) or hierarchical splines. For any scheme that we chose we should also remember that we need the approximating function to have high enough regularity for the bifurcation analysis, e.g., unless it is smoothed afterwards then a piecewise-smooth approximation would not be suitable.

For the graph transform method we will discuss the two strategies for approximating attractive manifolds; both of which may benefit by small changes in the iterative scheme depending on the application. The graph transform was described in the previous section for the continuous setting and given by Equation (7). The method is indeed simple to understand due to its geometric nature; flow the whole manifold, $M^i = \text{graph}(h^i)$, and reparameterize it. In the discrete setting the method is more complicated because we can only flow a set of discrete points and not the manifold as a set; in this context the topology of the dynamics on the NHIM becomes relevant. We know that the *generalized Lyapunov-type numbers* are uniform estimates for the relation between the manifold and the ambient space; the NHIM contraction and expansion rates will in general be highly non-uniform; remember that a $k$-dimensional compact overflowing NHIM $M$ may have all sorts of attractors and repellers that are possible in a k-dimensional dynamical system. We will discuss two methods of iterating the graph transform for compact overflowing NHIMs and refer to them as *GT-bvp* and *GT-ivp*, respectively. We illustrate the discrete graph transform in Figure 4 for both *GT-bvp* and *GT-ivp*.

### 4.1 Graph transform via boundary value problems — *GT-bvp*

*GT-bvp* is the standard method by which the graph transform has been implemented and this is by solving a boundary value problem (BVP) at each discrete grid point. Assume that we start with $M^i = \text{graph}(h^i)$, which is parameterized by and defined for all $x \in U \subset \mathbb{R}^k$, where $U$ is compact connected, in fact for our applications $U$ is simply a k-dimensional rectangle, i.e., $M^i$ is diffeomorphic to $U$. Under the hypotheses of Theorem 1 $M^{i+1}$ is diffeomorphic to $M^i$ and the pre-image of $M^{i+1}$ is inside a tubular neighborhood of $M^i$; this means that the BVP and the graph transform is well-posed for some fixed $t > 0$. The discrete graph transform follows directly from the definition Equation (7) which leads naturally to

$$\begin{pmatrix} \text{Id} \\ h^{i+1} \end{pmatrix} (\tilde{x}) = \begin{pmatrix} F^t \\ G^t \end{pmatrix} \circ \begin{pmatrix} \text{Id} \\ h^i \end{pmatrix} (x) \tag{13}$$

where $x \in \mathbb{R}^k$ is the unknown and $\tilde{x}$ is a grid point of which we want to know the corresponding function value $h^{i+1}(\tilde{x})$. Note that by the hypotheses

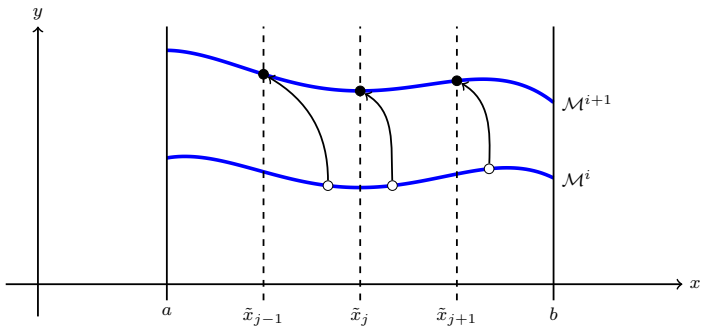


(a)

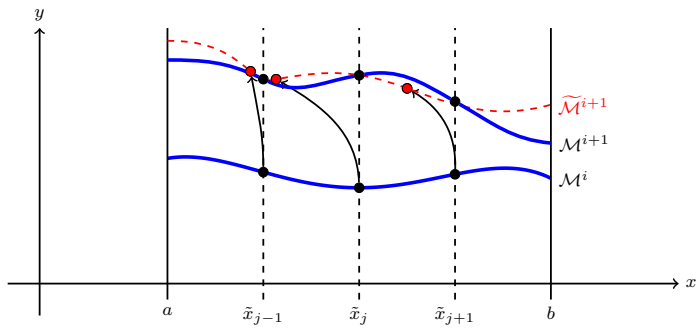


(b)

Fig. 4: Illustration of the two algorithm choices for the graph transform step. Panel (a) shows the graph transform step by solving boundary value problems via single shooting from $M^i$ to a grid point $\tilde{x}_j$. Panel (b) shows the flow of all grid points for flow time $t$, and how the two reparametrization steps are completed. First, all grid points (black bullets) from $M^i$ are acted on by the flow time $t$; they will in general end up off the grid (red bullets) and a temporary manifold $\widetilde{M}^{i+1}$ is interpolated from the scattered data set; the values at grid points of $M^{i+1}$ are assumed to be identical to $\widetilde{M}^{i+1}$ and $M^{i+1}$ is reinterpolate from these grid point values (black bullets).

of Theorem 1 and the definition of the setup $x$ is uniquely determined by

$$x = \left[ F^t \circ \begin{pmatrix} \mathrm{Id} \\ h^i \end{pmatrix} \right]^{-1} (\tilde{x}), \tag{14}$$

and consequently the problem is k-dimensional. Written in a more standard form for numerical BVPs we have

$$\begin{aligned} F^t(x,y) - \tilde{x}_j &= 0, \\ G^t(x,y) - h^{i+1}(\tilde{x}_j) &= 0, \\ y - h^i(x) &= 0, \end{aligned} \tag{15}$$

where $x$ is the unknown, $\tilde{x}_j$ is the $j$th grid point, $j = 1, 2, \ldots, N$ index for grid points, $y \in \mathbb{R}^{n-k}$ and $i = 1, 2, \ldots, n-k$. The BVP is defined by $k + (n-k) + (n-k)$ equations and the unknowns $(x_j, y, h^{i+1}(\tilde{x}_j))$, i.e., $k + (n-k) + (n-k)$ unknowns and it is well-posed. However, since $h^i(x)$ is known a priori it may be used that $(y, h^{i+1}(\tilde{x}_j))$ are explicitly given in the equations and only the starting point $x$ remains to be determined; this defines a k-dimensional BVP,

$$F^t(x, h^i(x)) - \tilde{x}_j = 0. \tag{16}$$

Depending on the choice of solution method, the complexity of the Newton iterations can be chosen to scale with the dimension of the manifold or the ambient space $\mathbb{R}^n$, i.e., $\mathcal{O}(k^3)$ or $\mathcal{O}(n^3)$. For a method that relies on Newton iterations to solve a BVP for k unknowns this is the *minimal* complexity, and this is a superior property and necessary advantage in the case where the codimension of the manifold is large.

Conclusively we comment on some of the important details related to the *GT-bvp* approach. With a specified flow time $t$, it is natural to consider the problem of how to ensure convergence of the Newton iteration, and this can be done via a simple homotopy (continuation) step from the trivial solution for flow time $t = 0$. Hence under the hypothesis of Theorem 1 the continuation problem in $\epsilon$ defined in the following way is well-posed

$$\begin{aligned} F^{\epsilon t}(x,y) - \tilde{x}_j &= 0, \\ G^{\epsilon t}(x,y) - h^{i+1}(\tilde{x}_j) &= 0, \\ y^{(i)} - h^i(x) &= 0, \end{aligned} \tag{17}$$

or

$$F^{\epsilon t}(x, h^i(x)) - \tilde{x}_j = 0, \tag{18}$$

where $\epsilon$ is increased from 0 to 1 in steps. Collocation and shooting methods are the standard methods for solving BVPs and depending on the choice of method the continuation problem will be $k$- or $n$-dimensional. Since the BVPs are naturally formulated as continuation problems numerical continuation packages such as, e.g., CoCo and AUTO can be applied to solve the BVPs. Further technical considerations in the implementation is the order of the polynomial approximation in collocation schemes or the order of the integrators for shooting and error control. For many more details on BVPs and continuation, see e.g., [1] [32].

### 4.2 Graph transform via initial value problems — *GT-ivp*

The *GT-ivp* method is relying solely on integration followed by a reinterpolation. Let $X$ denote a suitably chosen discrete set of base points $x \in U \subset \mathbb{R}^k$; then the graph transform is simply the time-$t$ flow of the set $(X, h^i(X))$,

$$\begin{pmatrix} \mathrm{Id} \\ h^{i+1} \end{pmatrix} (\tilde{X}) = \begin{pmatrix} F^t \\ G^t \end{pmatrix} \circ \begin{pmatrix} \mathrm{Id} \\ h^i \end{pmatrix} (X), \tag{19}$$

followed by a reinterpolation step of the new set $(\tilde{X}, h^{i+1}(\tilde{X}))$ such as to approximate the function $h^{i+1}$. While each graph transform step is orders of magnitude faster than solving BVP; it suffers from bad reinterpolations mainly because of non-uniformity; in particular it is non-trivial to control the quality of the reinterpolation of higher dimensional manifolds from scattered data; however, for our application the manifold is represented by a single chart and as a consequence we do not have to worry about the connectivity of the data set. There are two natural choices for interpolating on this scattered data set; one is via a higher-dimensional triangulation (Delauny, Voronoi) followed by linear interpolation and for small flow time $t$ the triangulation may still be good. The second method is meshfree (or meshless) interpolation [33], [34] via radial basis functions (Gaussians, Wendland, etc.) and it is precise for dense covers. But we do not have the luxury of dense covers (dense cover of a $k$-dimensional cube $N^k$ points quickly gets expensive); furthermore, it may be a difficult task to choose good shape parameters for the basis functions if the data is sparse, e.g., for Gaussian basis functions $\phi(r) = \exp(-c^2 r^2)$ where the parameter $c$ must be chosen well and $r = ||x - x_j||$.

Compared with *GT-bvp*, *GT-ivp* has potential to be much faster but it may suffer severely from the topology of the dynamics on the reduced manifold $M$ and care must be taken in the choice of flow-time in the graph transform; furthermore, since $M$ will in general have attracting and repelling neighborhoods the points must be reinterpolated between each step to prevent accumulation of the interpolation points in the attractors. In [30] three methods to iterate the graph transform for attractive one- and two-dimensional NHIMs without boundary (periodic orbits, tori) are presented, demonstrated and compared thoroughly; however, for the application in dimension reduction with manifolds with boundary many significant details change. The manifolds in this paper is constructed only using *GT-bvp*.

### 4.3 Modifying the graph transform to attracting submanifolds

One of the necessary conditions for the graph transform to converge in the present formulation is that the manifold is overflowing. This condition is not satisfied for attracting manifolds such as those usually approximated in dimension reduction. As it was mentioned earlier this implies that the pre-image of $M^{i+1}$ is not inside a tubular neighborhood of $M^i$ and consequently uniqueness is lost. We illustrate this in Figure 5. However, in the case of model reduc-

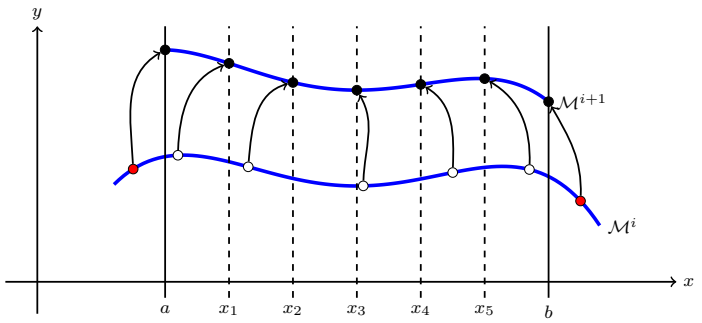


Fig. 5: Illustration of the consequences of violating the overflowing condition. The red bullets show that the pre-image of the end-points are outside the tubular neighborhood of $M^i$.

tion there is a multitude of manifolds that are all good candidates for $M^\infty$. As mentioned earlier this non-uniqueness is often encountered in applications and we must modify the vector field at the boundary

$$\partial M = \left\{(x,y) \in \mathbb{R}^k \times \mathbb{R}^{n-k} \middle| y = h(x), \forall x \in \partial U\right\}, \tag{20}$$

of the manifold. This may sound quite invasive, but in the case of dimension reduction we can check if the approximated attracting submanifold is good or not by comparison with the original models. In a discrete implementation such modifications of the vector field in small neighborhoods of the boundary are inconvenient, instead we will modify the graph transform steps by using extrapolation at the boundary. We note that the choice of extrapolation method is of course non-unique; in our implementations later we use a simple constant extrapolation from the k-dimensional rectangle domain.

It should be remarked that, while the modification may seem harmless, an extra effect comes into play; in the case of an overflowing compact NHIM the error from each iteration and reparameterization is suppressed by the attractiveness and the fact that any pre-image of any point on $M^{i+1}$ is inside the tubular neighborhood of $M^i$. When the overflowing condition is not satisfied errors may be transported in through the boundary via the extrapolation step.

For the convergence of the graph transform in the construction of a good approximate manifold $M$, the convergence criteria is usually

$$||h^{i+1} - h^i|| < \text{tol}, \tag{21}$$

and a measure for contraction rate is,

$$\frac{||h^{i+1} - h^i||}{||h^i - h^{i-1}||}. \tag{22}$$

The norm in our implementation was the 2-norm, however, it was practical to define another measure which we will describe in Section 6.

## 5 Example application: Reduction of a nonlinear mechanical problem

In this section we will approximate the attracting invariant manifolds via the graph transform in an example of the mechanical vibrations of the transverse vibrations of an Euler-Bernoulli beam with a torsional nonlinearity. The mechanical system is taken from [16] where dimension reduction is successfully applied via the method of NNMs. We motivate the use of the graph transform for dimension reduction in nonlinear mechanical systems by considering the case where we have obtained a finite-dimensional ODE model from a PDE formulation; assume that the ODE has the following structure,

$$M\ddot{x} + C\dot{x} + Kx = \epsilon f(x, \dot{x}, t, \lambda), \tag{23}$$

where $M, C, K \in \mathbb{R}^{n\times n}$ are the mass, damping and stiffness matrices, respectively, $x \in \mathbb{R}^n$ and $\epsilon \in \mathbb{R}$. In order to keep the example simple, we assume that $M, C, K$ are symmetric positive definite and that $C$ is chosen as linear modal damping; $f \in \mathbb{R}^n$ is smooth in all parameters and periodic, i.e., $f(x, \dot{x}, t, \lambda) = f(x, \dot{x}, t + 2\pi, \lambda)$. This allows the following modal form

$$\ddot{p} + 2\xi\Omega\dot{p} + \Omega^2 p = \epsilon g(p, \dot{p}, t, \lambda), \tag{24}$$

where $\xi$ is the modal damping factor and $\Omega$ is a diagonal matrix with entries corresponding to the eigenfrequencies $\omega_i$ of the undamped vibrations ordered such that $\omega_n > \ldots > \omega_1 > 0$. We put this system on standard first-order form,

$$\begin{aligned} \dot{p} &= q, \\ \dot{q} &= -2\xi\Omega q - \Omega^2 p + \epsilon g(p, q, \theta, \lambda), \\ \dot{\theta} &= 1, \end{aligned} \tag{25}$$

or as blocks

$$\begin{aligned} \dot{p}_i &= q_i, \\ \dot{q}_i &= -2\xi\omega_i q_i - \Omega^2 p_i + \epsilon g_i(p, q, \theta, \lambda), \\ \dot{\theta} &= 1, \end{aligned} \tag{26}$$

for $i = 1, \ldots, n$, where the periodic coordinate is $\theta \in \mathbb{S}^1$. Let $\epsilon = 0$ and disregard $\theta$ for a moment; in this case the origin is a global attractor and each $p_i$ and $q_i$ approaches 0 at an exponential rate, i.e., $\exp(-\xi\omega_i t)$. In this case there is a hierarchy of unique normally hyperbolic attracting submanifolds; the lowest dimensional is given by,

$$M = \left\{(p, q) \in \mathbb{R}^{2n} \middle| p_i = q_i = 0 \text{ for } i = 2, \ldots, n \wedge (p_1, q_1) \in V \subset \mathbb{R}^2\right\},$$

where $V$ contains the origin. Note that the hierarchy is determined directly by the ordering implicitly defined by the damping model. When $\epsilon = 0$ the $\theta$-dependence is decoupled and this independent variable is varying periodically,

i.e., the attracting submanifold is periodically varying and given by

$$M_0 = \Big\{(p,q,\theta) \in \mathbb{R}^n \times \mathbb{R}^n \times \mathbb{S}^1 \big| p_i = q_i = 0 \\ \text{for } i = 2,\dots,n \wedge (p_1,q_1,\theta) \in V \times \mathbb{S}^1\Big\}.$$

If we assume that the vector field has been modified such that $M_0$ is overflowing then Theorem 1 provides the existence and uniqueness of a NHIM $M_\epsilon$ for some $\epsilon > 0$, i.e.,

$$M_\epsilon = \Big\{(p,q,\theta) \in \mathbb{R}^n \times \mathbb{R}^n \times \mathbb{S}^1 \big| p_i = h_i(p_1,q_1,\theta), q_i = h_{i+n}(p_1,q_1,\theta) \\ \text{for } i = 2,\dots,n \wedge (p_1,q_1,\theta) \in V \times \mathbb{S}^1\Big\}.$$

From here on, the graph transform may be used in a homotopic continuation for $\epsilon \to 1$, assuming that the conditions of Theorem 1 are satisfied. We note that it may be quite instructive to consider the case where the system is linear and harmonically forced, i.e., $g_i(\theta) = A_i \cos(\theta)$; in this case the reduction implies that the reduced variables relax to their periodic steady states, i.e., their states only depend on $\theta$; it is useful to remember this when thinking about the same system with the addition of a weak nonlinearity. Note that parameters can be added to the construction by adding parameters as independent variables in the dynamical system, i.e.,

$$\begin{aligned} \dot{p} &= q, \\ \dot{q} &= -2\xi\Omega q - \Omega^2 p + \epsilon g(p,q,\theta,\lambda), \\ \dot{\lambda} &= 0, \\ \dot{\theta} &= 1, \end{aligned} \tag{27}$$

where $\lambda \in \mathbb{R}^r$ and in this case the manifolds are then also parameterized by $\lambda$, i.e., $h_i = h_i(p_1,q_1,\theta,\lambda)$. Hence such a manifold would be $(3+r)$-dimensional. The manifolds may naturally be constructed independently for each parameter-value in a continuation scheme. Note that it would be a trivial extension to add other types of time dependent forcing with other periods; of particular importance are then the smoothness requirements on $g$ and the overflowing condition. We remark that there exist other useful results, that allow for equivalent analysis, e.g., persistence results in the noncompact case [35], [36]. This can for example be useful for the analysis of systems with general time dependence.

### 5.1 Harmonically forced Euler-Bernoulli beam with a torsional nonlinearity

As an example we apply the described graph transform to obtain a dimension reduction of a nonlinear mechanical problem shown in Figure 6. The model is taken from [16], where a dimension reduction is performed by the previously

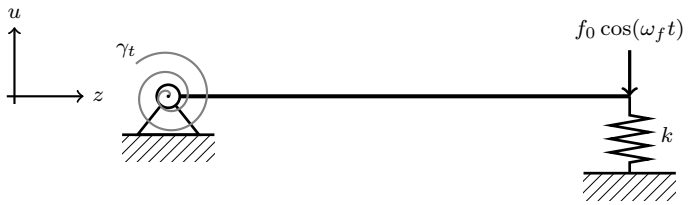


Fig. 6: System sketch of the mechanical system: a harmonically forced Euler-Bernoulli beam with a linear spring $k$ at the end point and a torsional nonlinearity $\gamma_t$ at the simply supported end.

mentioned method of NNMs. We restate the weak form and refer to [16] for further details,

$$\int_{t_1}^{t_2}\Big\{\int_0^l(\rho A\ddot{u}\delta u - EIu''\delta u'')\mathrm{d}x - ku(l,t)\delta u(l,t) - \gamma_t(\dot{u}(0,t))\delta u'(0,t) + F(t)\delta u(l,t)\Big\}\mathrm{d}t = 0,\ \ \forall t_1 < t < t_2. \tag{28}$$

Here, $u = u(z,t)$ is the transverse displacement, $z$ is the axial coordinate; the overdot denotes derivation wrt. time $t$, and the prime denotes derivation wrt. space $z$. Furthermore, $l = 1\,\mathrm{m}$ is the beam length; $\rho = 7860\,\mathrm{kg/m^3}$ is the mass density; $A = 0.0025\,\mathrm{m^2}$ is the cross-sectional area of the beam; $E = 2\cdot 10^1 1\,\mathrm{N/m^2}$ is the modulus of elasticity; $I = 5.0\cdot 10^{-8}\,\mathrm{m^4}$ is the cross section area moment of inertia; $k = 10^8\,\mathrm{N/m}$ is the stiffness of the spring at $z = l$; $F(t) = f_0\cos\omega_f t$ describes the harmonic excitation at $x = l$ with $f_0 = 3\cdot 10^6\,\mathrm{N}$; $\gamma_t$ is the torsional nonlinear force at $z = 0$ defined as

$$\gamma_t(\dot{u}(0,t)) = \left[5\cdot 10^3\cdot[\dot{u}(0,t)]^2 + 2\cdot 10^4\cdot[\dot{u}(0,t)]^3\right]\mathrm{N}, \tag{29}$$

where N denotes the unit Newton. Subsequently, linear modal damping is added to the model. After a suitable discretization, the system is represented in a 12-dof system ($n = 12$) description in the usual second order form,

$$M\ddot{p} + C\dot{p} + Kp = G(t) + N(\dot{p}), \tag{30}$$

where $M, C, K \in \mathbb{R}^{12\times 12}$ are the mass, damping and stiffness matrices, respectively, and $G(t)$ represents the harmonic forcing and $N(\dot{p})$ is the torsional nonlinearity. Rescaling time, transforming the system to modal form and subsequently to first order form as shown previously in order to obtain,

$$\begin{aligned}\dot{p} &= q,\\ \dot{q} &= -2\xi\Omega q - \Omega^2 p + \tilde{G}(\theta,\lambda) + \tilde{N}(q,\lambda),\\ \dot{\theta} &= 1,\end{aligned} \tag{31}$$

where the compact domain is $U = [a_1, b_1] \times [a_2, b_2] \times \mathbb{R}_{2\pi\mathbb{Z}}$. In other words, $U$ is the direct product of a two-dimensional rectangular region and a 'circle'; and the attracting submanifold that we want to approximate is given by

$$M = \Big\{(p, q, \theta) \in \mathbb{R}^{12} \times \mathbb{R}^{12} \times \mathbb{R}_{2\pi\mathbb{Z}} | p_i = h_i(p_1, q_1, \theta), q_i = h_{i+n}(p_1, q_1, \theta) \\ \text{for } i = 2, \ldots, 12 \wedge (p_1, q_1, \theta) \in U \Big\}.$$

In [16] the invariant manifold is then constructed by transforming the first mode to polar coordinates and then solving the invariance equation from an initial hypersurface ($k-1$ dimensional) defined by the solution of the linearized problem. In general, marching methods may be faster because they are not based on an iterative contraction mapping principle, but if a marching method is used to march in backwards time then a normally attracting manifold is an unstable object, e.g., consider approximating the center stable manifold marching from $(0, 0)$ in the simple case given in Equation (10) with $\alpha < 0$ and $|\alpha/\beta| \ll 1$, this yields an unstable algorithm, because the manifold is unstable in backward time. The graph transform method does not share these problems; in fact, when approximating the attracting submanifolds for this mechanical system we could initialize the graph transform from the zero-solution, and it converged to the manifold from this guess.

### 5.2 Results

Next we will review the results from the approximation via the graph transform. In order for a dimension reduction to be a success in an application, it is reasonable to demand that a prioritized set of conditions should be satisfied. *Firstly*, all qualitative measures of the limit sets are preserved, i.e., the bifurcation structure of the reference model and the reduced model must be identical. *Secondly*, quantitative measures are preserved, e.g., response amplitudes of periodic solutions. *Thirdly*, the attracting manifold is invariant, i.e., if a trajectory is initialized on the manifold then it stays on the manifold.

In order to thoroughly test the two first conditions we construct a two-parameter bifurcation diagram in frequency $\omega_f$ and forcing amplitude $f_0$. The third condition is tested by initializing a trajectory on the manifold and comparing it with the trajectory of the full model; this is done in Section 6. Furthermore, we compare a simple reduction based on linear projections with two reductions based on the graph transform, where one manifold is constructed for a fixed set of parameters and another which includes dependency on the forcing amplitude $f_0$.

We begin by explaining the two-parameter bifurcation diagram which we computed from the full model. The numerical bifurcation analysis was performed in MATLAB® using the numerical continuation package CoCo [1]. In the present case this was particularly convenient because the spline representation of the manifolds for the reduced equations could then be done via the

'griddedinterpolant()' function provided in MATLAB R2013a. In Figure 7 we show the results of the bifurcation analysis, and since the system is periodically forced we are considering families of periodic solutions, i.e., each point in the bifurcation diagram on the manifold represents a periodic orbit. For the previously defined model parameters and with $(\omega_f, f_0)$ as bifurcation parameters. In the diagram the $||p_1||$-axis, is the displacement of the first mode defined by a Poincaré map as $q_1$ changes sign from positive to negative velocity. The manifold in the bifurcation diagram is often referred to as a nonlinear resonance tongue; the red section of the manifold marks unstable periodic orbits while the blue part is stable periodic orbits; the common boundary of the red and blue manifolds is a smooth curve of fold points. The linear resonance of the system corresponds to the first modal eigenfrequency $\omega_1 = 222.43$ rad/s. Dynamical systems with such a type of nonlinear resonance tongue has the possibility of hysteresis, i.e., increasing the frequency from $\omega_f = 160$ rad/s at (sufficiently large forcing amplitudes) to $\omega_f = 280$ rad/s will give a discontinuous jump in response amplitude (large to small) and vice versa.

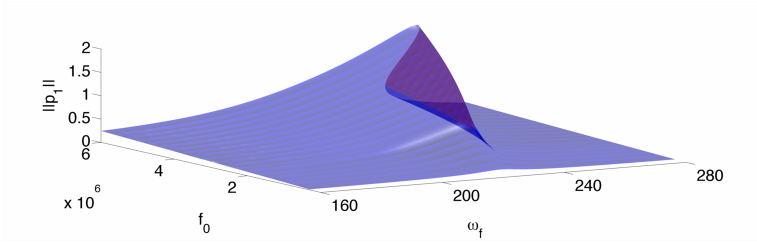


(a)

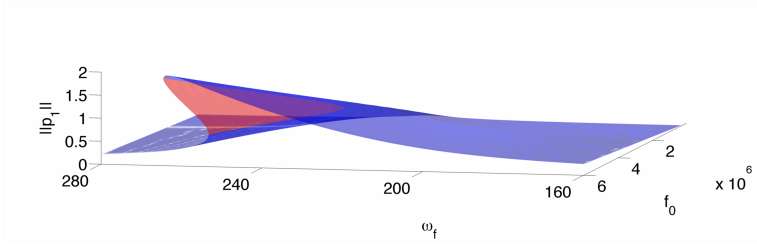


(b)

Fig. 7: Bifurcation diagram of the 1:1 nonlinear resonance tongue of the reference model Equation (31). Blue parts denote stable periodic orbits and red parts denote unstable.

We compare the bifurcation diagram of the reference model with bifurcation diagrams produced by linear reduction, GT-based reduction all parameters fixed and a GT-based reduction with the forcing amplitude $f_0$ as an independent variable.

The linear reduction is a linear projection onto the first mode, i.e., we consider $p_i = q_i = 0 \; \forall \; i = 2, \ldots, n$. It is a good idea to check this in order to see if a nonlinear reduction is necessary at all. In Figure 8 the full system is compared with the linear reduction; the bifurcation structures of the two systems are topologically equivalent, but the quantitative prediction of response amplitudes and fold points is very bad in the linear model, in particular the hardening nonlinearity has a stronger effect in the linear case, this implies that energy is transferred via nonlinear couplings.

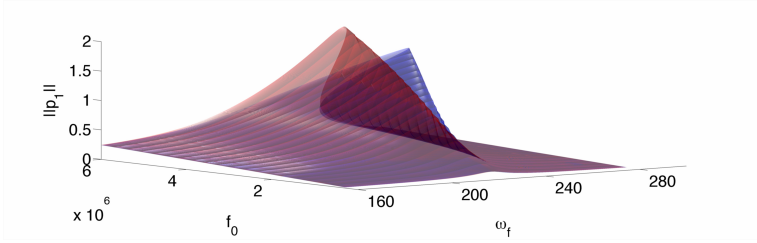


(a)

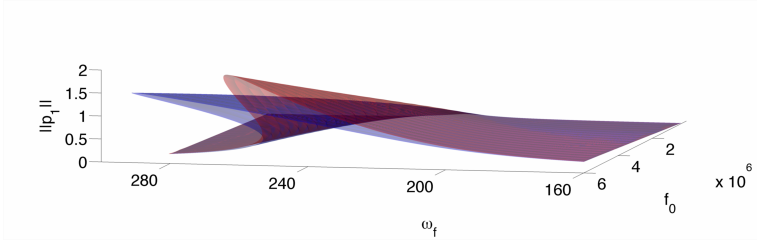


(b)

Fig. 8: Comparison of nonlinear resonance tongues between the linear reduction (blue) and the reference (red). Note that both $||p_1||$ and fold points are badly predicted.

Now we turn to the GT-based reductions. In the first case the attracting submanifold is approximated for a fixed parameter set, i.e., the manifold is 3-dimensional. The results are shown in Figure 9; in general, the quantitative and qualitative measures are fairly well approximated, and it is expected that the errors increase as the parameter set changes for example when the forcing amplitude changes away from the value of which the manifold was ap-

proximated. In the last GT-based reduction we added the dependency on the

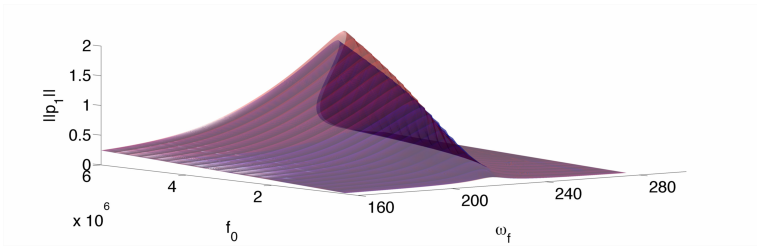


(a)

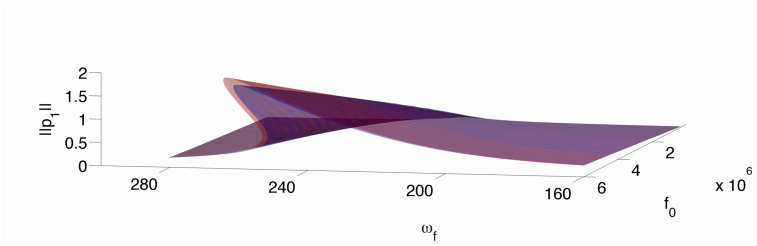


(b)

Fig. 9: Comparison of nonlinear resonance tongues between the GT-based reduction with fixed parameters (blue) and the reference model (red). Note that $||p_1||$ is very well predicted in a neighborhood of the construction values $(\omega_f, f_0) = (242, 1)$ and fold points quite well predicted for the whole range.

manifold of the forcing amplitude $f_0$ in order to show that the reduced model can indeed approximate the reference model to high precision. The results are shown in Figure 10.

Figures 8-10 are the maximum value of the displacement of $p_1$, and so they do not show how the reduced models approximates all degrees of freedom, this was chosen such that a comparison with the linear reduction would be more meaningful; Figure 11 shows this comparison for the manifold with interpolated values of the force amplitude parameter, i.e., Figure 10 but with the norm of all dimensions as the measure. Here we observe that the precision is not as accurate, but this is not a problem as such; in Figure 12 we show that it is easy to approximate the result of the reference model; this is done by comparing a slice where a manifold is also constructed for a range of values $\omega_f = \{160, 200, 240, 280\}$ rad/s. Furthermore, in Figure 9 it is observed that the reduced model with a manifold constructed at a fixed parameter set has a systematic underestimation of response amplitude when $f_0$ is larger than the value for which the manifold was approximated and vice versa. Similarly, it

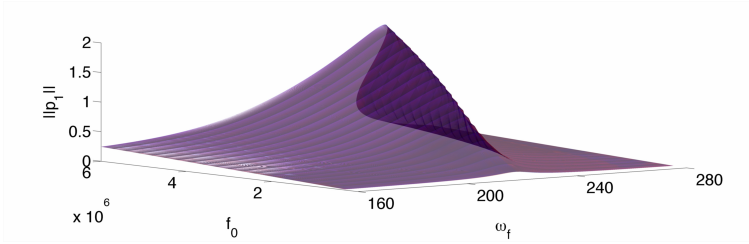


(a)

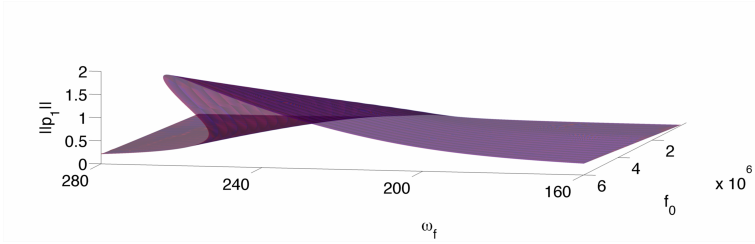


(b)

Fig. 10: Comparison of nonlinear resonance tongues between the GT-based reduction with parameter dependence in $f_0$ (blue) and the reference model (red). Note $||p_1||$ is very well predicted over all and that fold points are perfectly predicted.

may be observed in Figure 12(a) that the norm of the solutions is overestimated for $\omega_f$ smaller than the value for which the manifold was approximated and vice versa. This may be understood by considering the effect that forcing amplitude and frequency have on the response to first order, i.e., basically from linear analysis or something reminiscent of a lowest order perturbation correction. For the frequency dependence we let all velocities be corrected by,

$$q_i \approx h_{i+n}(p_1, q_1, \omega_f^*) + \frac{\omega_f - \omega_f^*}{\omega_f^*} h_{i+n}(p_1, q_1, \omega_f^*). \tag{32}$$

With this correction the perturbation correction is shown in Figure 12(b). It is may be possible to do better corrections, we merely wanted to show that corrections outside the reduced manifold have a good chance of behaving 'linearly' in a system such as the one considered here.

## 6 Convergence — how invariant is the approximated manifold?

As mentioned earlier there is a satisfying theory of convergence for the graph transform. In the current format since the boundary of the manifold is not

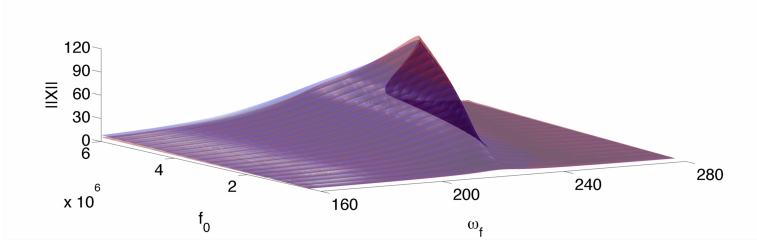


(a)

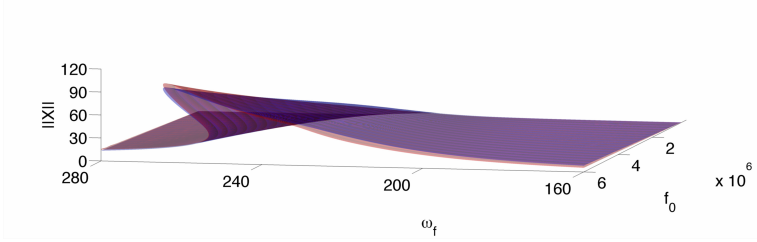


(b)

Fig. 11: Comparison of nonlinear resonance tongues between the GT-based reduction with parameter dependence in $f_0$ (blue) and the reference model (red). Note $||X||$ is the norm of the solution over all dimensions. Notice the systematic overprediction for $\omega_f < 250$ rad/s and underprediction for $\omega_f > 250$ rad/s, where $\omega_f = 250$ rad/s is the value for which the manifold was constructed. Furthermore, this reduced manifold is with added parameter dependence on the forcing amplitude $f_0$, this explains why the reduced manifold approximation is intersecting the reference manifold in a curve with $\omega_f \approx 250$ rad/s.

overflowing invariant a hypothesis of Theorem 1 is not satisfied and the convergence should not necessarily be expected to be uniform. Furthermore, the relevant measure for dimension reduction is more practical, i.e., while it may be possible to converge to some strict tolerance between consecutive iterates of the graph transform as in previous papers on the graph transform e.g. [31]; however, this convergence property seems to be too strict for practical purposes. What we really want to know is how invariant the manifold is.

Let $x(t)$ be an orbit from the full/reference model, equivalently let $x_{red}(t)$ be an orbit of the low-dimensional reduced model and let $\tilde{x}_{red}$ be the mapping that brings the reduced orbit into the full phase space, this is naturally done via the constructed invariant manifold. Consider the following measure,

$$||x - \tilde{x}_{red}||^2 = \int_0^T (x - \tilde{x}_{red})^2 \ \mathrm{d}t, \tag{33}$$

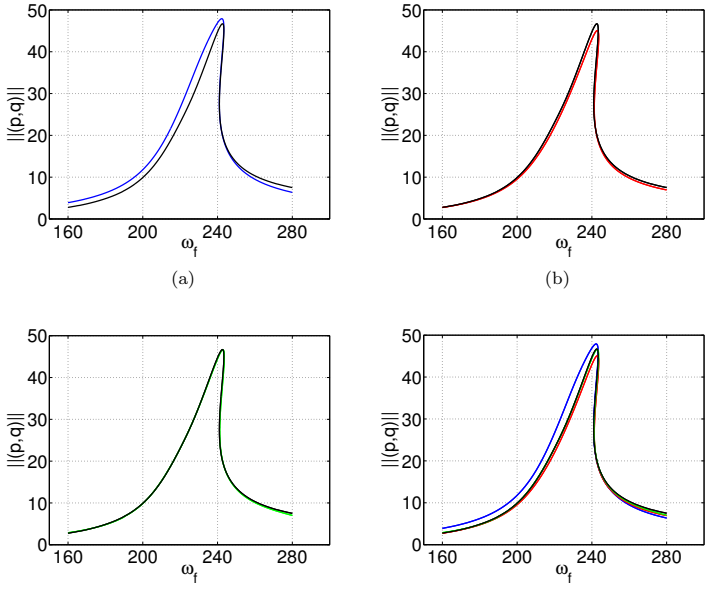


Fig. 12: Full norm of solutions: Comparison of reference model (black curve) with reduced models (blue, red, green). Panel (a) is based on a reduced manifold with fixed parameters ($\omega_f = 242\,\mathrm{rad/s}$), notice the systematic over and underestimation; Panel (b) is based on a reduced manifold with fixed parameters ($\omega_f = 242\,\mathrm{rad/s}$) with a semi-analytical first order correction; Panel (c) is based on a reduced manifold with parameter dependence in $\omega_f$ for $\{160, 200, 240, 280\}\,\mathrm{rad/s}$; Panel (d) is all approximations plotted together against the reference model.

where $T$ should then depend on the forcing period, i.e., some suitable number of periods. This is the squared error and it may be rewritten in discrete form. In the current implementation we applied a slightly different norm in the discrete data by introducing a weighted scaling such that the individual dimensions are expected to be scaled to $\mathcal{O}(1)$; this is done by a positive definite diagonal matrix $A$ that scales the dimensions according to the maximal amplitude of the periodic orbit. The norm is defined by,

$$||X||_A^2 = (AX)^T \cdot (AX) = X^T (A^T A) X, \tag{34}$$

where $A \in \mathbb{R}^n \times \mathbb{R}^n$ and $X \in \mathbb{R}^n \times \mathbb{R}^N$ with $N$ being the number of time steps. The convergence criteria is defined as a relative measure,

$$e = \frac{||X - X_{red}||_A}{||X||_A} < \mathrm{Rel}_{\mathrm{tol}}. \tag{35}$$

Since the idea of the convergence check is to measure how invariant the manifold is, the initial condition to the orbits is chosen on the manifold away from the stable limit cycles such that we also measure the transients on the manifold. If the system was initialized off the manifold the initial transient would count as an error and this would be misleading. This convergence measure provides the means to determine optimal settings for basis function type, grid type and stopping criteria when iterating the graph transform.

In the following we shall present some examples of this convergence test. The approximated attracting submanifolds that where used for the comparisons where constructed using a uniform grid with $(N_{p_1}, N_{q_1}, N_\theta) = (31, 31, 21)$ and we find $e < 0.01$, i.e., the relative square error is less than 1%. A reference orbit $x(t)$ [red] and a reduced orbit $x_{red}(t)$ [blue $\times$'s] are shown in Figure 13 for a visual comparison of the 2nd and 12th slaved mode. It should already be clear from the figures that the orbits agree, note that this is also the case for the transients on the attracting submanifold, however, this type of visual measure is not practical for manifolds of high codimension for example; the figures serve as visual verification that the orbits may be approximated very accurately.

The measure $e$ is naturally not unique, it is a creative measure since the orbits are not in any way dense on the manifold; furthermore, the choice of norm and convergence criteria may be chosen suitably for given applications. In Table I some values of $e$ are shown for several variations of the grids and iteration number. The iterations are initialized from the same initial guess, and the results indicate that the graph transform quickly relaxes at a level of relative error $e$; as it is expected for consistent numerical methods $e$ does indeed decrease with finer grids. A strict analysis of the convergence of the

| Grid\ Ite. | 10 | 100 | 1000 |
|---|---|---|---|
| $(8, 8, 4)$ | 27.65 % | 7.75 % | 8.13 % |
| $(8, 8, 8)$ | 27.90 % | 5.07 % | 4.39 % |
| $(8, 8, 16)$ | 28.74 % | 4.78 % | 4.35 % |
| $(16, 16, 4)$ | 27.07 % | 8.88 % | 7.04 % |
| $(16, 16, 8)$ | 26.31 % | 5.95 % | 1.85 % |
| $(16, 16, 16)$ | 27.11 % | 5.71 % | 1.52 % |
| $(32, 32, 4)$ | 27.44 % | 8.90 % | 7.37 % |
| $(32, 32, 8)$ | 26.67 % | 5.99 % | 1.78 % |
| $(32, 32, 16)$ | 27.46 % | 5.76 % | 0.91 % |

Table I: Convergence of invariance measure as a function of grid density and graph transform iteration. Grid means $(N_{p_1} - 1, N_{q_1} - 1, N_\theta - 1)$.

graph transform is not made in the traditional format, because the boundary

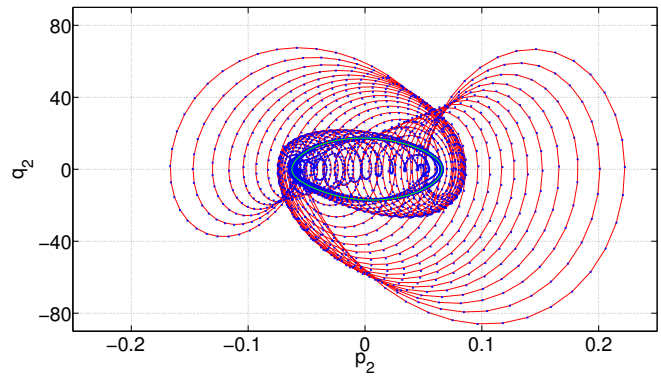


(a)

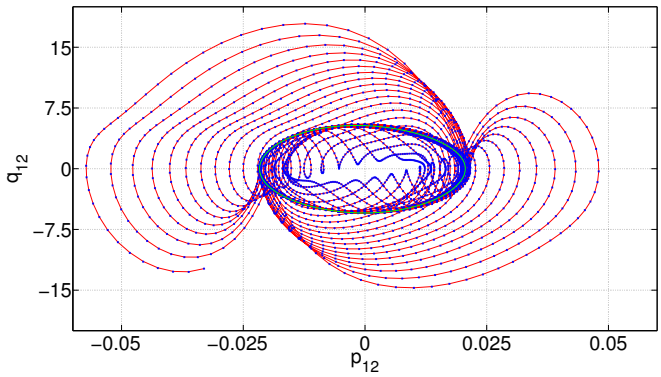


(b)

Fig. 13: Phase plane visual comparison; red is the reference orbit; blue crosses are the reduced model; green is the periodic orbit: Panel (a) shows the lowest slaved mode (2) and Panel (b) shows the highest slaved mode (12). Note how precise the transient details are captured.

is not overflowing invariant the convergence is not uniform, it oscillates but converges at a linear rate as it should, see this in Figure 14. It seems reasonable to hypothesize that more invasive boundary modifications such as fixing the boundary would render the convergence uniform and the submanifold unique. A regular convergence study still remains to be performed after a suitable

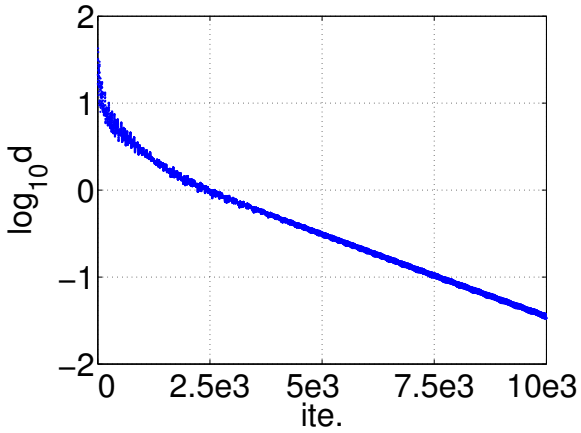


Fig. 14: Verification of the linear convergence rate of the graph transform; d is the 2-norm difference between the $i$th and $(i+1)$th iterate of the graph transform. Note that, the convergence is nonuniform, this is due to the violation of the overflowing condition; modifications that fix the boundary from a certain iteration might possibly solve this. Furthermore, the number of graph transforms is very large in the figure; in the practical applications it is unnecessary to perform many graph transform iterations (cf. Table I). This convergence study is made for $(N_{p_1} - 1, N_{q_1} - 1, N_\theta - 1) = (8, 8, 8)$. While the graph transform has converged to a tolerance that is $10^2$ times smaller than that at ite. $= 1000$ the relative convergence measure is basically (cf. Table I) unchanging $e = 4.37\%$ and this exemplifies that the strict convergence measure is not that relevant for the practical application in dimension reduction.

boundary modification; note however that the convergence measure of the graph transform has little impact on the quality of the manifold (cf. Table I).

## 7 Discussion, conclusion and perspective

In the previous sections we demonstrated how the graph transform can be applied in dimension reduction, we also provided the details for the numerical implementation, and discussed the advantages and disadvantages compared to other methods of construction. Summing up; the graph transform method is algorithmically of minimal complexity in the Newton steps because it scales with the spatial dimension of the manifold $k - 1$ for nonautonomous systems) in solving the BVPs; furthermore, it is robust and independent wrt. the dynamics on the manifold, this makes it trivial to obtain good uniform meshes and unlike many other methods the graph transform offers a theory of con-

vergence; the only drawback being that the scheme is only linearly convergent (cf. Figure 14) and this underlines the importance of the size of the spectral gap; however, as Table I indicates the reduced manifolds are rather useful for practical purposes for relatively early iterates. The violation of the overflowing condition, in general, implies non-uniqueness and in order to overcome this the graph transform was modified using extrapolation at the boundary similar to [31]; we did not prove that the method always converges using this modification, but as it was shown in Section 6 the modified algorithm does share the linear convergence rate; although it is not uniformly convergent. We remark that the algorithm was not optimized in the current study; a few obvious changes that may increase the speed is, an adaptive scheme for varying the flow time, e.g., as there is a sort of hierarchy of time scales that settle to the reduced manifold at different time scales the flow time may be increased, in the particular example such a time scale hierarchy could be found by the linear modes, i.e., the 12th mode basically settles fast and the 2nd settles last.

Other methods march from an appropriate $(k-1)$-dimensional boundary, but these are vulnerable to the structure and topology of the dynamics on and off the manifold; furthermore, marching methods in which the Newton steps scale with the codimension of the attracting low-dimensional submanifold are not suitable for high-dimensional systems (large-scale systems). In the paper [37] a series of efficient methods for computing the stable two-dimensional manifold of the origin in the Lorenz system are reviewed. The setting is different because the stable manifold is unique and attracting as a set and by definition all points on the stable manifold converge to the origin as $t \to \infty$; this provides the possibility of a good global transversal initial condition, in the present setting it is more problematic because the dynamics on the manifold does not have such a simple structure. Nevertheless, with some modifications the methods of advancing the front of these manifolds could be useful in the setting of model reduction. In particular, the method of Krauskopf and Osinga using geodesic circles [38] [39] and Hendersons computation via fat trajectories [40], [41], [42]; both methods generalize to higher dimensions. We remark that a mixed scheme which takes advantage of the speed of low-complexity marching methods and the superior convergence and stability properties of the graph transform may be a better alternative than one or the other.

We remark that if dimension reduction is to be used in practice then it is of importance that reduced models are validated by comparison with reference models; and this comparison should be performed via the bifurcation structure found in the reduced models. The graph transform has Newton steps of complexity scaling only with the manifold dimension $k$ and this makes it attractive for systems with high codimension as opposed to the traditional methods.

## References

1. H. Dankowicz and F. Schilder. *Recipes for Continuation*. Computational Science and Engineering Series. Society for Industrial and Applied Mathematics, 2013.

2. E. J. Doedel with major contributions from A.R. Champneys, T. Fairgrieve, Yu.A. Kuznetsov, B. Oldeman, R. Paffenroth, B. Sandstede, X. Wang, and C. Zhang. *AUTO-07P : Continuation and bifurcation software for ordinary differential equations*. Concordia University Montreal, Canada.
3. J. Sanchez, M. Net, B. Garcia-Archilla, and C. Simo. Newton-krylov continuation of periodic orbits for navier-stokes flows. *JOURNAL OF COMPUTATIONAL PHYSICS*, 201(1):13–33, 2004.
4. H. A. Dijkstra, F. W. Wubs, A. K. Cliffe, E. Doedel, I. F. Dragomirescu, B. Eckhardt, A. Y. Gelfgat, A. L. Hazel, V. Lucarini, A. G. Salinger, E. T. Phipps, J. Sanchez-Umbria, H. Schuttelaars, L. S. Tuckerman, and U. Thiele. Numerical bifurcation methods and their application to fluid dynamics: Analysis beyond simulation. *COMMUNICATIONS IN COMPUTATIONAL PHYSICS*, 2014.
5. J. C. Robinson. *Infinite-Dimensional Dynamical Systems: An Introduction to Dissipative Parabolic PDEs and the Theory of Global Attractors*. Cambridge Texts in Applied Mathematics. Cambridge University Press, 2001.
6. N. Fenichel. Persistence and smoothness of invariant manifolds for flows. *Indiana Univ. Math. J.*, 21:193–226, 1971.
7. S. Wiggins. *Normally hyperbolic invariant manifolds in dynamical systems*. Springer, 1994.
8. W.A. Coppel. *Dichotomies in Stability Theory*. Lecture Notes in Mathematics. Springer, 1978.
9. U. Maas and SB Pope. Simplifying chemical-kinetics - intrinsic low-dimensional manifolds in composition space. *COMBUSTION AND FLAME*, 88(3-4):239–264, 1992.
10. S.H. Lam and D.A. Goussis. Csp method for simplifying kinetics. *International Journal of Chemical Kinetics*, 26(4):461–486, 1994.
11. M. R. Roussel and S. J. Fraser. Geometry of the steady-state approximation - perturbation and accelerated convergence methods. *JOURNAL OF CHEMICAL PHYSICS*, 93(2):1072–1081, JUL 15 1990.
12. CW Rowley. Model reduction for fluids, using balanced proper orthogonal decomposition. *INTERNATIONAL JOURNAL OF BIFURCATION AND CHAOS*, 15(3):997–1013, 2005.
13. S. W. Shaw and C. Pierre. Non-linear normal modes and invariant manifolds. *Journal of Sound and Vibration*, 150(1):170–173, 1991.
14. Shaw and Pierre. Normal modes for non-linear vibratory systems. *Journal of Sound and Vibration*, 164(1):85–124, 1993.
15. S. W. Shaw and C. Pierre. Normal modes of vibration for non-linear continuous systems. *Journal of Sound and Vibration*, 169(3):319–347, 1994.
16. D. Jiang, C. Pierre, and S. W. Shaw. Nonlinear normal modes for vibratory systems under harmonic excitation. *JOURNAL OF SOUND AND VIBRATION*, 288(4-5):791–812, 2005.
17. AF Vakakis. Non-linear normal modes (nnms) and their applications in vibration theory: An overview. *MECHANICAL SYSTEMS AND SIGNAL PROCESSING*, 11(1):3–22, 1997.
18. CW Rowley, T. Colonius, and RM Murray. Model reduction for compressible flows using pod and galerkin projection. *PHYSICA D-NONLINEAR PHENOMENA*, 189(1-2):115–129, 2004.
19. Konstantin V. Avramov and Yuri V. Mikhlin. Review of applications of nonlinear normal modes for vibrating mechanical systems. *Applied Mechanics Reviews*, 65(2):020801, 2013.
20. J. Carr. *Applications of Centre Manifold Theory*. Number vb. 35 in Applied Mathematical Sciences Series. Springer-Verlag, 1981.
21. C. Chicone. *Ordinary Differential Equations with Applications*. Texts in Applied Mathematics. Springer, 2006.
22. N. Fenichel. Geometric singular perturbation theory for ordinary differential equations. *Journal of Differential Equations*, 31(1):53–98, January 1979.
23. C. K. R. T. Jones. Geometric singular perturbation theory. In Russell Johnson, editor, *Dynamical Systems*, volume 1609 of *Lecture Notes in Mathematics*, pages 44–118. Springer Berlin Heidelberg, 1995.

24. N. Fenichel. Asymptotic stability with rate conditions. *Indiana Univ. Math. J.*, 23:11091137, 1974.
25. N. Fenichel. Asymptotic stability with rate conditions, ii. *Indiana Univ. Math. J.*, 26:81–93, 1977.
26. M. W. Hirsch, C. C. Pugh, and M. Shub. *Invariant Manifolds*. Number nr. 583 in Lecture Notes in Mathematics. Springer-Verlag, 1977.
27. Luca Dieci and Jens Lorenz. Computation of invariant tori by the method of characteristics. *SIAM Journal on Numerical Analysis*, 32(5):1436–1474, October 1995.
28. Hinke M Osinga. *Computing invariant manifolds: Variations on the Graph Transform*. PhD thesis, Rijksuniversiteit Groningen, 1996.
29. HW Broer, HM Osinga, and G. Vegter. Algorithms for computing normally hyperbolic invariant manifolds. *ZEITSCHRIFT FUR ANGEWANDTE MATHEMATIK UND PHYSIK*, 48(3):480–524, 1997.
30. Volker Reichelt. Computing invariant tori and circles in dynamical systems. In *in Doedel and Tuckerman*, pages 407–437. Springer, 2000.
31. H. W. Broer, A. Hagen, and G. Vegter. Numerical continuation of normally hyperbolic invariant manifolds. *NONLINEARITY*, 20(6):1499–1534, 2007.
32. B. Krauskopf, H. M. Osinga, and J. Galan-Vioque. *Numerical continuation methods for dynamical systems : path following and boundary value problems*. Springer, 2007.
33. G.E. Fasshauer. *Meshfree Approximation Methods with MATLAB*. Interdisciplinary mathematical sciences. World Scientific, 2007.
34. G.R. Liu. *Mesh Free Methods: Moving Beyond the Finite Element Method*. Taylor & Francis, 2010.
35. P. W. Bates, K. N. Lu, and C. C. Zeng. Persistence of overflowing manifolds for semiflow. *Communications On Pure and Applied Mathematics*, 52(8):983–1046, August 1999.
36. J. Eldering. Persistence of noncompact normally hyperbolic invariant manifolds in bounded geometry. *Comptes Rendus Mathematique*, 350(11-12):617–620, June 2012.
37. B. Krauskopf, HM Osinga, EJ Doedel, ME Henderson, J. Guckenheimer, A. Vladimirsky, M. Dellnitz, and O. Junge. A survey of method's for computing (un)stable manifold of vector fields. *INTERNATIONAL JOURNAL OF BIFURCATION AND CHAOS*, 15(3):763–791, 2005.
38. B. Krauskopf and H. Osinga. Globalizing two-dimensional unstable manifolds of maps. *INTERNATIONAL JOURNAL OF BIFURCATION AND CHAOS*, 8(3):483–503, 1998.
39. B. Krauskopf and HM Osinga. Computing geodesic level sets on global (un)stable manifolds of vector fields. *SIAM JOURNAL ON APPLIED DYNAMICAL SYSTEMS*, 2(4):546–569, 2003.
40. M. E. Henderson. Higher-dimensional continuation. In B. Krauskopf, H. M. Osinga, and J. Galan-Vioque, editors, *Numerical Continuation Methods for Dynamical Systems*, pages 77–115. Springer Netherlands, 2007.
41. M. E. Henderson. Computing invariant manifolds by integrating fat trajectories. *SIAM JOURNAL ON APPLIED DYNAMICAL SYSTEMS*, 4(4):832–882, 2005.
42. M. E. Henderson. Flow box tiling methods for compact invariant manifolds. *SIAM Journal on Applied Dynamical Systems*, 10(3):1154–1176, 2011.

Appendix D

# Beam theory

In this Appendix we derive the beam equation. The derivation is based on three sources Landau [LL86], Klarbring [Kla06] and Antman [Ant06].

We derive the equations of motion from Euler's Laws to describe the dynamics of the beam. Euler's Law of linear momentum,

$$\int_\Omega \mathbf{b}\, \mathrm{d}V + \int_{\partial\Omega} \mathbf{T}\cdot\mathbf{n}\, \mathrm{d}S = \int_\Omega \rho\mathbf{a}\, \mathrm{d}V, \tag{D.1}$$

and Euler's Law of angular momentum,

$$\int_\Omega \mathbf{x}\times\mathbf{b}\, \mathrm{d}V + \int_{\partial\Omega} \mathbf{x}\times(\mathbf{T}\cdot\mathbf{n})\, \mathrm{d}S = \int_\Omega \mathbf{x}\times\rho\mathbf{a}\, \mathrm{d}V, \tag{D.2}$$

where $S$ and $V$ denotes surface and volume, respectively, $\rho$ is the mass density, $\mathbf{a}$ is the acceleration, $\mathbf{b}$ is contributions from volume forces. In both equations $\mathbf{n}$ denotes the normal vector directed out of beam volume $\Omega$ and $\mathbf{T}$ is the stress tensor and $\mathbf{T}\cdot\mathbf{n}$ is the stress component in the normal direction $\mathbf{n}$; the fields may in general depend on space and time. In the following we imagine the beam to be static and let $\mathbf{a} = 0$, later we can add time dependence. The first assumption is that the beam is so thin that we may approximate it with a curve. Essentially

this means that Euler's Laws may be reformulated in a simplified form,

$$\int_c^s \mathbf{q}\, \mathrm{d}\xi + \mathbf{f}(s) - \mathbf{f}(c) = 0, \tag{D.3}$$

$$\int_c^s \mathbf{r} \times \mathbf{q} + \mathbf{l}\, \mathrm{d}\xi + \mathbf{m}(s) - \mathbf{m}(c) + \mathbf{r}(s) \times \mathbf{f}(s) - \mathbf{r}(c) \times \mathbf{f}(c) = 0, \tag{D.4}$$

where the terms outside the integrals are cut forces and cut couples (boundary conditions for the end points) of the piece of rod $[c, s]$, and $\mathbf{l}$ is a body force couple that originates from a part of the surface of the beam. Assuming a proper amount of regularity we differentiate the expressions and obtain the local formulations,

$$\frac{\partial \mathbf{f}}{\partial s} + \mathbf{q} = 0, \tag{D.5}$$

$$\mathbf{r} \times \mathbf{q} + \mathbf{l} + \frac{\partial \mathbf{m}}{\partial s} + \frac{\partial}{\partial s}(\mathbf{r} \times \mathbf{f}) = 0, \tag{D.6}$$

substitution of Equation (D.5) in (D.6) simplifies the angular momentum equation,

$$\frac{\partial \mathbf{m}}{\partial s} + \frac{\partial \mathbf{r}}{\partial s} \times \mathbf{f} + \mathbf{l} = 0. \tag{D.7}$$

Equation (D.5) and (D.7) are the equilibrium equations of the Cosserat[1] theory of beams/rods [Ant06]. Given a beam described by $\mathbf{r}(s)$ and the body force $\mathbf{q}(s)$ and couple $\mathbf{l}(s)$, Equation (D.5) and (D.7) is in general a set of six linear non-autonomous ordinary differential equations; it may be comfortable to understand the system from this perspective, e.g., for the purposes of considerations regarding uniqueness, existence and regularity.

Before we go on with the reduction of the equations we state the relations of the one-dimensional theory of rods to the three-dimensional beams, see [Kla06],

[1] This theory is due to two brothers Eugene and Francois Cosserat in the early 20th century. Although, it is unrelated, it is perhaps an interesting historical note that Eugene began his studies at École normale supérieure in 1883 and one year later Jacques Hadamard became a fellow student and the *graph transform* that is a cornerstone of Paper C is due to Hadamard (1901).

such that we understand the significance of the variables; we have

$$\mathbf{q}(s) = \int_{A(s)} \mathbf{b}\ \mathrm{d}x_n \mathrm{d}x_b\ + \int_{\partial A(s)} \mathbf{T}(\mathbf{n})\ \mathrm{d}r,$$
$$\mathbf{f}(s) = \int_{A(s)} \mathbf{T}(\mathbf{e}_s)\ \mathrm{d}x_n \mathrm{d}x_b,$$
$$\mathbf{l}(s) = \int_{A(s)} (x_n\mathbf{e}_n + x_b\mathbf{e}_b) \times \mathbf{b}\ \mathrm{d}x_n \mathrm{d}x_b + \int_{\partial A(s)} (x_n\mathbf{e}_n + x_b\mathbf{e}_b) \times \mathbf{T}(\mathbf{n})\ \mathrm{d}r,$$
$$\mathbf{m}(s) = \int_{A(s)} (x_n\mathbf{e}_n + x_b\mathbf{e}_b) \times \mathbf{T}(\mathbf{e}_s)\ \mathrm{d}x_n \mathrm{d}x_b,$$

where $x_n$, $x_b$ are coordinates in the cross-sections. Seeing these equations, may provides extra insight to the mathematical details of the problem. These relations are useful to understand how geometrical variations and parameter variations would come into play, but it is important to understand that they are not particularly useful if the geometry is much more than trivial perturbations from an easily parameterized object.

In the current study, we restrict the bending to a plane, and our beam is symmetric across the plane that contains the centroid of the beam. If we choose a right-handed orthonormal coordinate system defined by the standard basis $\{\mathbf{e}_x, \mathbf{e}_y, \mathbf{e}_z\}$, and we assume that the bending plane is span$\{\mathbf{e}_x, \mathbf{e}_z\}$, then we may reduce the variables to,

$$\begin{aligned} &\mathbf{q} = q_x\mathbf{e}_x + q_z\mathbf{e}_z,\ \mathbf{f} = f_x\mathbf{e}_x + f_z\mathbf{e}_z, \\ &\mathbf{l} = l_y\mathbf{e}_y,\ \mathbf{m} = m_y\mathbf{e}_y, \\ &\mathbf{r} = r_x\mathbf{e}_x + r_z\mathbf{e}_z. \end{aligned} \tag{D.8}$$

Substituting the relations of Equations (D.8) in Equation (D.5) and (D.7) we obtain the component form of bending in the plane,

$$\frac{\partial f_x}{\partial s} + q_x = 0, \tag{D.9}$$
$$\frac{\partial f_z}{\partial s} + q_z = 0, \tag{D.10}$$
$$\frac{\partial m_y}{\partial s} + \nu f_x - \eta f_z + l_y = 0, \tag{D.11}$$

where $\nu, \eta$ are defined by $\frac{\partial \mathbf{r}}{\partial s} = \eta\mathbf{e}_x + \nu\mathbf{e}_z$. If we furthermore assume that the centroid of the undeformed beam is a subset $B$ of the $z$-axis,

$$B = \{(x, y, z) \in \mathbb{R}^3 |\ x = y = 0,\ z = s \in [0, L]\}, \tag{D.12}$$

then the hypothesis of small displacements and small curvatureamounts to $||r_x||/L \ll 1$ and $||\partial_{ss}\mathbf{r}||L \ll 1$; since by definition $\eta = \partial_s\mathbf{r} \cdot \mathbf{e}_x = \partial_s r_x$ we

may conclude that the moment from $\eta f_z$ may be neglected via the smallness constraints for the cantilever beam ($r_x(0) = r'_x(0) = 0$). This is realized by using,

$$||r'_x(s)|| = \left|\left| r'_x(0) + \int_0^s r''_x(\xi)\,\mathrm{d}\xi \right|\right| \leq ||r'_x(0)|| + ||r''_x||L \ll 1. \tag{D.13}$$

Alternatively one may artificially extend the beam to $\mathbb{R}$ in a way such that the smallness constraints still hold uniformly; in such a case Taylor's theorem [Rud64] may be applied to obtain a useful uniform estimate of the first derivative of a function $f$ assuming

$$c_0 = \sup_{x\in\mathbb{R}} |f(x)|, \qquad c_2 = \sup_{x\in\mathbb{R}} |f''(x)|, \tag{D.14}$$

and letting $h > 0$ we write

$$f(x+h) = f(x) + f'(x)h + \frac{1}{2}f''(a)h^2, \tag{D.15}$$

where $a \in \mathbb{R}$.

$$f'(x) = \frac{f(x+h) - f(x)}{h} - \frac{h}{2}f''(a), \tag{D.16}$$

choose $h = \sqrt{c_0/c_2}$ to obtain,

$$\sup_{x\in\mathbb{R}} |f'(x)| \leq M\sqrt{c_0 c_2}, \tag{D.17}$$

where is $M$ is a constant with $M \geq 0$, thus we obtain $||r'_x(s)|| \ll 1$. These two arguments may seem a bit pedantic, but we show them since, strictly speaking, the smallness of the first derivative does not follow merely from the smallness constraints.

It follows that $\nu = 1$ to first order because $\mathbf{r}(s)$ is parameterized unit-speed. It is worth noting that these conditions equivalently imply that the length $L^*$ of the deformed beam is the same as the undeformed $L$ to first order. In [Ant06] it is remarked that $\eta = 0$ and $\nu = 1$ means that the material is *unshearable* and *inextensible*, respectively. Combining this with the Euler-Bernoulli constitutive equation which says that the moment is linear in curvature, we may obtain the Euler-Bernoulli beam equation.

We will not derive the Euler-Bernoulli constitutive equation here; it is as follows,

$$m_y = EI\frac{\partial^2 u}{\partial s^2}, \tag{D.18}$$

where we let $u$ denote the transverse displacement of the beam. Differentiating Equation (D.11), applying $\eta = 0$ and $\nu = 1$, and using Equation (D.9) and (D.18) to obtain,

$$\frac{\partial^2}{\partial s^2}\left(EI\frac{\partial^2 u}{\partial s^2}\right) + \frac{\partial l_y}{\partial s} - q_x = 0. \tag{D.19}$$

Again as a consequence of the smallness conditions we may interchange $s$ with $z$ and $\mathbf{u} = u\mathbf{e}_x$ likewise to obtain,

$$\frac{\partial^2}{\partial z^2}\left(EI\frac{\partial^2 u}{\partial z^2}\right) + \frac{\partial l_y}{\partial z} - q_x = 0. \tag{D.20}$$

In our applications we are concerned with the forced transverse vibrations of thin beams with constant cross sections and homogeneous material; so in order to get some dynamics in the equation we can add this to the body couple $l_y$ and body force $q_x$.

For the body couple one may add the effect of rotational inertia of the cross sections, $l_y = -\rho I_{xx}\frac{\partial^3 u}{\partial z \partial t^2}$; this effect is negligible in the present study because the considered beams are thin and $I_{xx} \propto L^2_{\text{thickness}}$, hence to first order it is reasonable to take $l_y = 0$. The excitation and the linear momentum of the moving body is added through the body force term $q_x = F(z,t) - \rho A\frac{\partial^2 u}{\partial t^2}$, and by substitution we obtain Euler-Bernoullis beam equation for the small transverse vibrations of a harmonically forced thin beam,

$$\rho A\frac{\partial^2 u}{\partial t^2} + EI\frac{\partial^4 u}{\partial z^4} = F(z,t). \tag{D.21}$$

Appendix E

# Galerkin princple

We derive the weak form of the transverse vibrations of a beam in the following way,

$$
\begin{aligned}
0 &= \int_0^L \left( \rho A \frac{\partial^2 u}{\partial t^2} + EI \frac{\partial^4 u}{\partial z^4} - F(z,t) \right) \phi(z) \, \mathrm{d}z \\
&= \int_0^L \left[ \left( \rho A \frac{\partial^2 u}{\partial t^2} - F(z,t) \right) \phi(z) + EI \frac{\partial^2 u}{\partial z^2} \frac{\partial^2 \phi}{\partial z^2} \right] \mathrm{d}z + \left[ EI \frac{\partial^3 u}{\partial z^3} \phi - EI \frac{\partial^2 u}{\partial z^2} \frac{\partial \phi}{\partial z} \right]_0^L .
\end{aligned}
$$

Since the beam is a cantilever, it has one end clamped (at $z = 0$) and one end free (at $z = L$), i.e.,

$$
u(0,t) = \frac{\partial u}{\partial z}(0,t) = 0, \ \text{(essential bcs)} \tag{E.1}
$$

$$
\frac{\partial^2 u}{\partial z^2}(L,t) = \frac{\partial^3 u}{\partial z^3}(L,t) = 0, \ \text{(natural bcs)}. \tag{E.2}
$$

Essential boundary conditions are satisfied through the choice of approximating function space, $\phi(0) = \partial_z \phi(0) = 0$, whereas the natural conditions are satisfied directly in the weak form, such that the weak form is then

$$
0 = \int_0^L \left( \rho A \frac{\partial^2 u}{\partial t^2} \phi + EI \frac{\partial^2 u}{\partial z^2} \frac{\partial^2 \phi}{\partial z^2} - F(z,t) \phi \right) \, \mathrm{d}z.
$$

Now let $S_n = \text{span}(\phi_1(z), \ldots, \phi_n(z))$ be a suitable chosen approximating finite-dimensional subspace[1] and let $u_n = \sum_{i=1}^{n} a_i(t)\phi_i(z)$, Galerkins equations then emerge from the constraint that the residual of the weak form is orthogonal to the approximating subspace, hence inner-product between the residual and $\phi_j$ must vanish for all $j = 1, \ldots, n$

$$0 = \int_0^L \left( \rho A \frac{\partial^2 u_n}{\partial t^2} \phi_j + EI \frac{\partial^2 u_n}{\partial z^2} \frac{\partial^2 \phi_j}{\partial z^2} - F(z,t)\phi_j \right) \mathrm{d}z, \tag{E.3}$$

$$0 = \int_0^L \left( \rho A \frac{\partial^2 a_i}{\partial t^2} \phi_i \phi_j + EI a_i \frac{\partial^2 \phi_i}{\partial z^2} \frac{\partial^2 \phi_j}{\partial z^2} - F(z,t)\phi_j \right) \mathrm{d}z. \tag{E.4}$$

Note that we sum over the repeated index $i$. Equation E.4 is a standard $n$-dimensional $T$-periodically forced second order ODE,

$$M\ddot{a} + Ka = f(t), \tag{E.5}$$

where $M, K \in \mathbb{R}^{n \times n}$ are symmetric matrices and $f : \mathbb{R} \to \mathbb{R}^n$ and $a = (a_1, \ldots, a_n) \in \mathbb{R}^n$.

[1] It is implied that we are talking about a function space with an inner-product.

# Bibliography


[Adh00] Sondipon Adhikari. *Damping models for structural vibration.* PhD thesis, Cambridge University, 2000.

[AE] V. Avrutin and M. Elmegård. Private communication with Viktor Avrutin.

[ALS+03] V Avrutin, R Lammert, M Schanz, G Wackenhut, and GS Osipenko. On the software package ant 4.669 for the investigation of dynamical systems. In *Fourth International Conference on Tools for Mathematical Modelling*, volume 9, pages 24–35, 2003.

[AM13] Konstantin V. Avramov and Yuri V. Mikhlin. Review of applications of nonlinear normal modes for vibrating mechanical systems. *Applied Mechanics Reviews*, 65(2):020801, 2013.

[Ant06] S. Antman. *Nonlinear Problems of Elasticity.* Applied mathematical sciences. Springer, 2006.

[Arn81] V.I. Arnold. *Singularity Theory.* Cambridge Surveys of Economic Literature. Cambridge University Press, 1981.

[Arn06] V.I. Arnold. *Ordinary differential equations.* Universitext (1979). Springer, 2006.

[Bar96] Grigory Isaakovich Barenblatt. *Scaling, self-similarity, and intermediate asymptotics: dimensional analysis and intermediate asymptotics*, volume 14. Cambridge University Press, 1996.

[BBCK07] M. Bernardo, C. Budd, A.R. Champneys, and P. Kowalczyk. *Piecewise-smooth dynamical systems: theory and applications*, volume 163. Springer, 2007.

[BD07] G.E.P. Box and N.R. Draper. *Response Surfaces, Mixtures, and Ridge Analyses*. Wiley Series in Probability and Statistics. Wiley, 2007.

[BHV07] H. W. Broer, A. Hagen, and G. Vegter. Numerical continuation of normally hyperbolic invariant manifolds. *NONLINEARITY*, 20(6):1499–1534, 2007.

[BKK94] I. U. Bronshtein, A. Ya Kopanskii, and Aleksandr IAkovlevich Kopanskii. *Smooth invariant manifolds and normal forms*, volume 7. World Scientific, 1994.

[Bol64] V.V. Bolotin. *The dynamic stability of elastic systems*. Number vb. 3 in Holden-Day series in mathematical physics. Holden-Day, 1964.

[BOV97] HW Broer, HM Osinga, and G. Vegter. Algorithms for computing normally hyperbolic invariant manifolds. *ZEITSCHRIFT FUR ANGEWANDTE MATHEMATIK UND PHYSIK*, 48(3):480–524, 1997.

[BSS+13] Emil Bureau, Frank Schilder, Ilmar Ferreira Santos, Jon Juel Thomsen, and Jens Starke. Experimental bifurcation analysis of an impact oscillator — tuning a non-invasive control scheme. *Journal of Sound and Vibration*, 332(22):5883 – 5897, 2013.

[Bur] E. Bureau. Private communication with Emil Bureau.

[CH53] R. Courant and D. Hilbert. *Methods of Mathematical Physics*, volume 1. Interscience Publishers, Inc., New York, NY, 1953.

[Chi06] C. Chicone. *Ordinary Differential Equations with Applications*. Texts in Applied Mathematics. Springer, 2006.

[DGK03] Annick Dhooge, Willy Govaerts, and Yu A Kuznetsov. Matcont: a matlab package for numerical bifurcation analysis of odes. *ACM Transactions on Mathematical Software (TOMS)*, 29(2):141–164, 2003.

[dH56] Jacob Pieter den Hartog. *Mechanical vibrations*. DoverPublications. com, 1956.

[DPC+07] E. J. Doedel, R. C. Paffenroth, A. R. Champneys, T. F. Fairgrieve, Yu A Kuznetsov, B. E. Oldeman, B. Sandstede, and X. J. Wang. Auto-07p: Continuation and bifurcation software for ordinary differential equations. *Available for download from http://indy. cs. concordia. ca/auto*, 2007.

[DS] H. Dankowicz and F. Schilder. http://sourceforge.net/projects/cocotools/.

[DS13] H. Dankowicz and F. Schilder. *Recipes for Continuation*. Computational Science and Engineering Series. Society for Industrial and Applied Mathematics, 2013.

[Dys04] Freeman Dyson. A meeting with enrico fermi. *Nature*, 427(6972):297–297, January 2004.

[Eva10] L.C. Evans. *Partial Differential Equations*. Graduate studies in mathematics. American Mathematical Society, 2010.

[Fen71] N. Fenichel. Persistence and smoothness of invariant manifolds for flows. *Indiana Univ. Math. J.*, 21:193–226, 1971.

[Fen79] N. Fenichel. Geometric singular perturbation theory for ordinary differential equations. *Journal of Differential Equations*, 31(1):53–98, January 1979.

[GH83] John Guckenheimer and Philip Holmes. *Nonlinear oscillations, dynamical systems, and bifurcations of vector fields*. Springer-Verlag, 1983.

[Gov00] Willy JF Govaerts. *Numerical methods for bifurcations of dynamical equilibria*. Number 66. Siam, 2000.

[GP10] Victor Guillemin and Alan Pollack. *Differential topology*, volume 370. American Mathematical Soc., 2010.

[GS85] Martin Golubitsky and D Schaeffer. Singularities and groups in bifurcation theory. volume i, applied mathematical sciences vol. 51. 1985.

[GV04] John Guckenheimer and Alexander Vladimirsky. A fast method for approximating invariant manifolds. *SIAM Journal on Applied Dynamical Systems*, 3(3):232–260, 2004.

[Hen02] Michael E Henderson. Multiple parameter continuation: Computing implicitly defined k-manifolds. *International Journal of Bifurcation and Chaos*, 12(03):451–476, 2002.

[Hol77] PJ Holmes. Bifurcations to divergence and flutter in flow-induced oscillations: a finite dimensional analysis. *Journal of Sound and Vibration*, 53(4):471–503, 1977.

[Hun67] Herbert Edwin Huntley. *Dimensional analysis*. Dover New York, 1967.

[JPS05] D. Jiang, C. Pierre, and S. W. Shaw. Nonlinear normal modes for vibratory systems under harmonic excitation. *JOURNAL OF SOUND AND VIBRATION*, 288(4-5):791–812, 2005.

[Kel67] Al Kelley. The stable, center-stable, center, center-unstable, unstable manifolds. *Journal of Differential Equations*, 3(4):546–570, 1967.

[KGVB05] Gaetan Kerschen, Jean-claude Golinval, Alexander F Vakakis, and Lawrence A Bergman. The method of proper orthogonal decomposition for dynamical characterization and order reduction of mechanical systems: an overview. *Nonlinear Dynamics*, 41(1-3):147–169, 2005.

[KK02] Hans G Kaper and Tasso J Kaper. Asymptotic analysis of two reduction methods for systems of chemical reactions. *Physica D: Nonlinear Phenomena*, 165(1):66–93, 2002.

[Kla06] A. Klarbring. *Models of Mechanics*. Solid mechanics and its applications. Springer, 2006.

[KOD+05] B. Krauskopf, HM Osinga, EJ Doedel, ME Henderson, J. Guckenheimer, A. Vladimirsky, M. Dellnitz, and O. Junge. A survey of method's for computing (un)stable manifold of vector fields. *INTERNATIONAL JOURNAL OF BIFURCATION AND CHAOS*, 15(3):763–791, 2005.

[Kuz04] I.U.A. Kuznetsov. *Elements of Applied Bifurcation Theory*. Number vb. 112 in Applied Mathematical Sciences. Springer, 2004.

[LG94] S.H. Lam and D.A. Goussis. Csp method for simplifying kinetics. *International Journal of Chemical Kinetics*, 26(4):461–486, 1994.

[LL86] L.D. Landau and E.M. Lifshitz. *Course of Theoretical Physics vol. 7: Theory of elasticity*. Butterworth-Heinemann, Oxford England Burlington, MA, 1986.

[Mei01] L. Meirovitch. *Fundamentals of Vibrations*. McGraw-Hill, Boston, 2001.

[MH79] FC Moon and Philip J Holmes. A magnetoelastic strange attractor. *Journal of Sound and Vibration*, 65(2):275–296, 1979.

[Mil97] John W Milnor. *Topology from the differentiable viewpoint*. Princeton University Press, 1997.

[MP92] U. Maas and SB Pope. Simplifying chemical-kinetics - intrinsic low-dimensional manifolds in composition space. *COMBUSTION AND FLAME*, 88(3-4):239–264, 1992.

[MS83] F. C. Moon and S. W. Shaw. Chaotic vibrations of a beam with non-linear boundary-conditions. *International Journal of Non-linear Mechanics*, 18(6):465–477, 1983.

[NM95] Ali H Nayfeh and Dean T Mook. *Nonlinear oscillations*. Wiley, wiley classics library edition, 1995.

[PPS02] E. Pesheck, C. Pierre, and S.W. Shaw. A new galerkin-based approach for accurate non-linear normal modes through invariant manifolds. *Journal of Sound and Vibration*, 249(5):971 – 993, 2002.

[RCM04] C.W. Rowley, T. Colonius, and R.M. Murray. Model reduction for compressible flows using pod and galerkin projection. *PHYSICA D-NONLINEAR PHENOMENA*, 189(1-2):115–129, 2004.

[Rei00] Volker Reichelt. Computing invariant tori and circles in dynamical systems. In *in Doedel and Tuckerman*, pages 407–437. Springer, 2000.

[RF90] M. R. Roussel and S. J. Fraser. Geometry of the steady-state approximation - perturbation and accelerated convergence methods. *JOURNAL OF CHEMICAL PHYSICS*, 93(2):1072–1081, JUL 15 1990.

[Rob98] C. Robinson. *Dynamical Systems: Stability, Symbolic Dynamics, and Chaos*. Studies in Advanced Mathematics. Taylor & Francis, 1998.

[Rob01] J. C. Robinson. *Infinite-Dimensional Dynamical Systems: An Introduction to Dissipative Parabolic PDEs and the Theory of Global Attractors*. Cambridge Texts in Applied Mathematics. Cambridge University Press, 2001.

[Row05] CW Rowley. Model reduction for fluids, using balanced proper orthogonal decomposition. *INTERNATIONAL JOURNAL OF BIFURCATION AND CHAOS*, 15(3):997–1013, 2005.

[Rud64] Walter Rudin. *Principles of mathematical analysis*, volume 3. McGraw-Hill New York, 1964.

[Sey10] R. Seydel. *Practical Bifurcation and Stability Analysis*. Interdisciplinary Applied Mathematics. Springer, 2010.

[SFLC87] Michael Shub, Albert Fathi, Rémi Langevin, and Joseph Christy. *Global stability of dynamical systems*, volume 11. Springer-Verlag New York, 1987.

[SGBN+08] J. Sieber, A. Gonzalez-Buelga, S.A. Neild, D.J. Wagg, and B. Krauskopf. Experimental continuation of periodic orbits through a fold. *Phys. Rev. Lett. (USA)*, 100(24):244101–1–4, 2008.

[Sha85] S. W. Shaw. Forced vibrations of a beam with one-sided amplitude constraint - theory and experiment. *Journal of Sound and Vibration*, 99(2):199–212, 1985.

[SK08] J. Sieber and B. Krauskopf. Control based bifurcation analysis for experiments. *Nonlinear Dynamics*, 51(3):365–377, 2008.

[SP91] S. W. Shaw and C. Pierre. Non-linear normal modes and invariant manifolds. *Journal of Sound and Vibration*, 150(1):170–173, 1991.

[SP93] S. W. Shaw and C. Pierre. Normal modes for non-linear vibratory systems. *Journal of Sound and Vibration*, 164(1):85–124, 1993.

[Tem97] R. Temam. *Infinite Dimensonal Dynamical Systems in Mechanics and Physics*. Applied Mathematical Sciences. U.S. Government Printing Office, 1997.

[Wig94] S. Wiggins. *Normally hyperbolic invariant manifolds in dynamical systems*. Springer, 1994.

[Wig03] Stephen Wiggins. *Introduction to applied nonlinear dynamical systems and chaos*, volume 2. Springer, 2003.

[ZKK04] Antonios Zagaris, Hans G Kaper, and Tasso J Kaper. Analysis of the computational singular perturbation reduction method for chemical kinetics. *Journal of Nonlinear Science*, 14(1):59–91, 2004.